

# **Frequency Agile Microwave Circuits Based on Ferroelectric Thin-Film Varactors**

Frequenzagile Mikrowellenschaltungen auf der Basis  
ferroelektrischer Dünnsfilm-Varaktoren

Der Technischen Fakultät der  
Universität Erlangen-Nürnberg  
zur Erlangung des Grades

**DOKTOR-INGENIEUR**

vorgelegt von  
Dipl.-Ing. Errikos Lourandakis

Erlangen - 2009

Als Dissertation genehmigt von  
der Technischen Fakultät der  
Universität Erlangen-Nürnberg

Tag der Einreichung:	02.02.2009
Tag der Promotion:	15.04.2009
Dekan:	Prof. Dr.-Ing. habil. J. Huber
Berichterstatter:	Prof. Dr.-Ing. Dr.-Ing. habil. R. Weigel Prof. Dr.-Ing. R. Jakoby

# Acknowledgment

I would like to express my appreciation to some individuals who supported my work throughout the last years. First of all, I want to mention Prof. Dr.-Ing. Robert Weigel who gave me the opportunity to conduct this work. Without his guidance, support, and motivating spirit I would have not reached at this point. My sincere appreciation goes also to Prof. Dr.-Ing. Georg Fischer for his cooperation and helpful guidance at the final stage of my thesis.

Furthermore, my appreciation goes to my colleagues at the Institute for Electronics Engineering at the University of Erlangen-Nuremberg for establishing such an inspiring work environment. It has been a pleasure to participate in a team of highly motivated and qualified researchers. Among all, I have to distinguish my former colleague Dr. Matthias Schmidt, who has been an important partner and has contributed greatly to our research project. Additionally, I would like to mention Benjamin Waldmann, Stefan Zorn, and Alexander Kölpin for their valuable collaboration over the last years.

At this point I want to emphasize the important contribution of our industrial partner the EPCOS AG, and namely Dr. Anton Leidl and Dr. Stefan Seitz. By providing us ferroelectric varactors we could implement and verify our proposed concepts. Last but not least, I want to thank Prof. Dr.-Ing. Rolf Jakoby and his team at TU Darmstadt for their cooperation within the BMBF funded MARIO-Project.

Nuremberg, February 2009

Errikos Lourandakis

# Abstract

The trend for mobile communications is clearly moving toward increasing numbers of communication standards and services which occupy expanding wide frequency ranges. At the same time the physical dimensions of handheld user devices are shrinking, leading to even tighter specifications for the highly integrated front-end architectures of mobile radios. Modern front-end architectures use dedicated receive and transmit paths for each covered communication standard. Thus the overall complexity and occupied area is increasing as well. The wide frequency allocation of the regulated communication bands, which have to be covered by these radios, calls for reconfigurable and frequency agile microwave subsystems. By introducing such subsystems, new architectures with reduced numbers of functional blocks could be implemented. Attractive applications for tunable circuits in the RF front-end are tunable matching networks, filters, and reconfigurable power amplifiers. New concepts are desired which can combine several of these individual circuits, in order to improve the overall front-end efficiency. Since the target application is the operation in handheld devices, certain design goals have to be considered such as size, losses, power consumption, linearity, and overall costs.

One possibility to achieve tunability in microwave circuits is the introduction of tunable passive components, based on ferroelectric materials or microelectromechanical systems (MEMS). Both families of tunable passives are discussed in this work. Among the numerous ferroelectric materials, Barium-Strontium-Titanate (BST) is probably the most suitable candidate. Its RF behavior as well as its manufacturing technology have been investigated intensively over the past years. In this thesis, ferroelectric thin-film BST varactors serve as tuning elements in order to design frequency agile microwave circuits in the frequency region around 2 GHz. Based on BST varactors several frequency agile subsystems, like filters, couplers and power dividers will be discussed. Analytical design procedures are presented and the suitability of the proposed designs is demonstrated with prototype boards. Novel filter topologies are presented along with one innovative concept for designing reduced size frequency agile circuits, such as power dividers and couplers. The operation of the implemented tunable microwave circuits is investigated in terms of simulation and measurement setups.

# Zusammenfassung

Der Trend in der Mobilfunkkommunikation entwickelt sich dahin, dass immer mehr Standards und Anwendungen abgedeckt werden müssen. Diese funkbasierten Dienste erstrecken sich über einen sich stetig ausbreitenden Frequenzbereich. Gleichzeitig ist eine zunehmende Entwicklung in Richtung Miniaturisierung bei den Abmessungen der Mobilfunkgeräte festzustellen. Beide Entwicklungen kombiniert führen zu erhöhten Anforderungen an die Transceiver-Architekturen der Geräte. In modernen Sende- und Empfänger-Implementierungen werden dedizierte Kommunikationspfade für die jeweiligen Betriebsmodi eingesetzt. Somit ergeben sich eine hohe Anzahl von HF-Baugruppen und eine damit verbundene hohe Komplexität. Der weite Frequenzbereich, der für die verschiedenen Kommunikationsstandards abgedeckt werden muss, erklärt die Notwendigkeit für abstimmbare und frequenzagile HF-Schaltungen. Durch die Einführung solcher Subsysteme werden Architekturen mit einer reduzierten Anzahl an HF-Baugruppen ermöglicht. Interessante Anwendungen für abstimmbare Schaltungen im Frontend sind u.a. abstimmbare Anpassnetzwerke, Filter und rekonfigurierbare Sendestufen. Neue Konzepte sind erforderlich, die mehrere solcher Schaltungen kombinieren, um die Effizienz existierender Systeme zu steigern. Da der Einsatz in Mobilfunkgeräten angedacht ist, müssen gewisse Aspekte wie z.B. die Abmessungen der Schaltungen, HF-Verluste, Leistungsverbrauch und Linearität untersucht werden.

Eine Möglichkeit um ein abstimmbares Verhalten von Mikrowellenschaltungen zu erzielen ist die Einführung von passiven abstimmbaren Komponenten. Diese können auf unterschiedlichen Technologien basieren, z.B. auf ferroelektrischen Materialien oder auf mikroelektromechanischen Systemen (MEMS). Beide technologischen Ansätze werden in dieser Arbeit untersucht. Unter einer Vielfalt an ferroelektrischen Materialien erscheint Barium-Strontium-Titanat (BST) als die wohl geeigneteste Wahl. Sowohl das HF-Verhalten als auch die Herstellungsprozesse von solchen ferroelektrischen Schichten wurden bereits intensiv erforscht. In der vorliegenden Arbeit dienen BST-Varaktoren als abstimmbare Komponenten zum Entwurf von frequenzagilen Mikrowellenschaltungen im Frequenzbereich um 2 GHz. Auf der Basis von BST-Varaktoren wurden unterschiedliche abstimmbare Schaltungen wie z.B. Filter, Koppler und Leistungsteiler untersucht. Analytische Entwurfsmethoden werden vorgestellt und implementierte Prototypschaltungen verifiziert. Die Funktion solcher abstimmbarer Schaltungen wird mit Hilfe von Simulationen und Messungen untersucht.

# Index

<b>1. Introduction</b>	<b>5</b>
<b>2. Tunable Passive Components</b>	<b>8</b>
2.1. Ferroelectric Varactors . . . . .	8
2.1.1. Thin-Film Varactors . . . . .	10
2.1.2. Interdigital Varactors . . . . .	20
2.2. Microelectromechanical Systems – MEMS . . . . .	21
2.2.1. MEMS Varactor . . . . .	22
<b>3. Frequency Agile Filters</b>	<b>30</b>
3.1. Network Synthesis Method . . . . .	30
3.2. Transformations with Lumped Components . . . . .	33
3.3. Transformations with Distributed Components . . . . .	36
3.4. Lowpass Filter . . . . .	40
3.5. Notch Filter . . . . .	43
3.6. Bandpass Filter . . . . .	45
<b>4. Frequency Agile Power Dividers and Couplers</b>	<b>52</b>
4.1. Wilkinson Power Divider . . . . .	52
4.2. Branch-Line Coupler . . . . .	54
4.3. Equivalent Quarter-Wavelength Segments . . . . .	55
4.4. Frequency Agile Wilkinson Divider . . . . .	62
4.5. Frequency Agile Branch-Line Coupler . . . . .	64
<b>5. Prototype Implementation and Experimental Results</b>	<b>68</b>
5.1. Assembly Techniques . . . . .	68
5.2. Tunable Lowpass Filter . . . . .	71
5.3. Tunable Notch Filter . . . . .	75
5.4. Tunable Compline Filter . . . . .	79
5.5. Reduced Size Tunable Power Divider . . . . .	83
5.6. Reduced Size Tunable Branch-Line Coupler . . . . .	87

---

<b>6. Reconfigurable Front-End Systems</b>	<b>93</b>
6.1. Modulation Analysis . . . . .	93
6.2. Balanced Amplifier . . . . .	97
6.3. Reconfigurable Amplifier . . . . .	101
6.4. Bias Circuitry . . . . .	109
<b>7. Conclusion and Outlook</b>	<b>112</b>
<b>A. Transmission Matrix and Transformations</b>	<b>113</b>
<b>B. Two-Tone Measurement Setup</b>	<b>115</b>
<b>C. List of Abbreviations</b>	<b>117</b>
<b>Bibliography</b>	<b>118</b>
<b>Curriculum Vitae</b>	<b>129</b>
<b>Publications</b>	<b>130</b>

# 1. Introduction

Over the last decade mobile communication has become one of the driving forces in the global technology market. This becomes more evident when considering the numbers of overall sold handheld devices. Starting from the year 2006, where the number of one billion units was exceeded, a constant growth is taking place. By introducing the 3<sup>rd</sup> generation mobile phones, also called 3G phones, the operation in more communication standards was established. Typically, these handheld devices cover 4 to 5 standards including GSM/EDGE 850/900/1800/1900 MHz and WCDMA Band I at 2100 MHz. At the same time, the overall physical dimensions of the devices shrunk, leading to even tighter specifications for the analog front-end. A simplified schematic of a 3G front-end is depicted in Fig. 1.1.

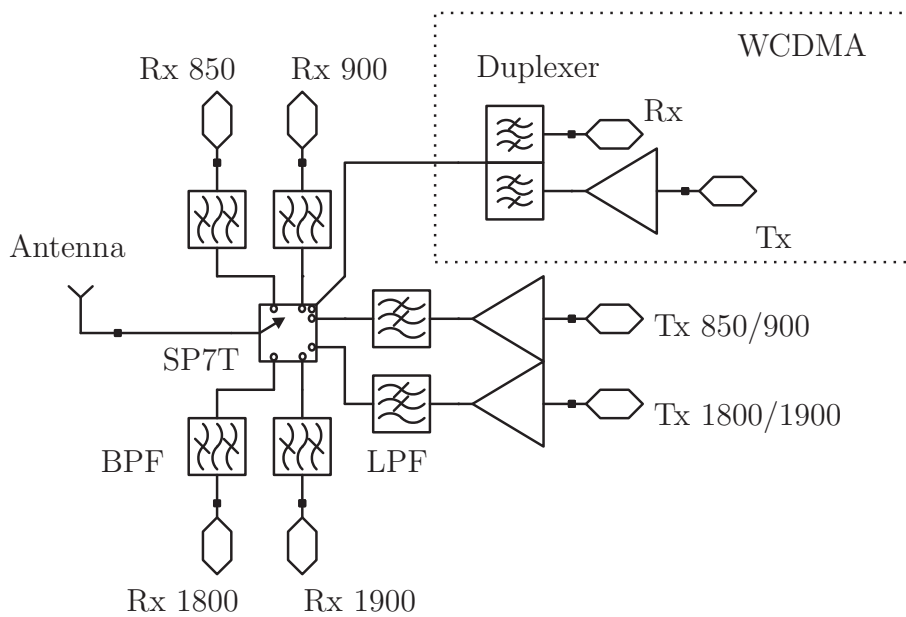


Figure 1.1.: Schematic of a 3G front-end architecture.

It consists of an antenna front-end module which incorporates a multi-pole switch, in this case an SP7T (Single-Pole Seven-Throw). The individual communication paths are switched to the antenna port depending on the operating mode. The indicated bandpass filters and the duplexer are implemented as surface acoustic wave (SAW) and film bulk acoustic resonator (FBAR) components [1]. This technology



allows for implementation of very compact filters with excellent RF performance in terms of overall losses and selectivity. These filters along with additionally electrostatic discharge (ESD) and matching circuitry are included in one common multi-band module [2], [3]. One further step to miniaturization is the implementation of modules, which combine power amplifiers and the corresponding duplexers or bandpass filters [4], [5]. The predominant technology for manufacturing this type of modules is based on an LTCC (Low Temperature Co-fired Ceramic) multilayer structure and flip-chip mounting [6], [7]. The overall dimensions of multi-band filter modules have been reduced significantly by these manufacturing techniques [8], [9].

Since the emerge of 3G phones additional services like satellite based navigation (GPS, Global Positioning System), wireless web access (IEEE 802.11 a/b/g), and Bluetooth (IEEE 802.15.1) communication have been added. These new functionalities are accompanied by further RF hardware blocks, since different frequency bands have to be covered.

It becomes clearly evident, that new concepts for reconfigurable architectures are needed in order to reduce the number of functional blocks within the front-end. One interesting possibility is the introduction of tunable and frequency agile subsystems, which add a tuning functionality. Tunable passive devices based on ferroelectrics or microelectromechanical systems (MEMS) have been investigated intensively over the last years. As a result of these efforts several implementations have been reported. The majority of them concern passive circuits, such as filters [10], [11], [12], matching networks [13], [14], [15], [16], phase shifters [17], [18], and baluns [19]. Concepts of adaptive antennas with tunable characteristics have been reported as well [20], [21]. Additionally, active microwave circuits with tunable characteristics have been presented, like voltage controlled oscillators [22], [23] and power amplifiers [24], [25], [26]. Despite the already proven potential and the interesting possibilities of such approaches, so far the investigations have been carried out mostly by academic research groups. Over the last years some work has also been triggered by industrial parties [27], since the potential use of such circuits in communication devices discloses a mass volume market.

Objective of this thesis is to provide a comprehensive understanding of the potential of tunable components in designing reconfigurable microwave circuits. Starting from a discussion on their physical and electrical properties, novel concepts and design methodologies of frequency agile microwave circuits are presented. In order to pave the way towards complete system solutions all implemented prototypes are investigated in terms of small and large signal performance. Additionally, one complete subsystem solution of a reconfigurable transmitter topology will be discussed. Operation in the system context with real world modulated signals is investigated and verified on the basis of simulations and measurements, respectively. In this work both types of elements, ferroelectric and MEMS-based components will be discussed in the following Chapter 2. In Chapter 3 and 4 methodologies of designing novel frequency agile subsystems such as filters, power dividers, and couplers

will be presented. Finally, in Chapter 5 these concepts are verified by implemented prototype boards based on ferroelectric thin-film varactors. All fabricated prototypes are characterized in terms of small and large signal performance through scattering parameter and two-tone measurements, respectively. In Chapter 6 a concept for a reconfigurable front-end subsystem is presented. System parameters such as linearity and modulation quality are addressed based on a simulation and measurement setup with modulated signals.

## 2. Tunable Passive Components

In this chapter the focus lies on the discussion of tunable passive components and their properties and potential for use in microwave circuits. There is a variety of technologies and materials for the implementation of tunable passive components. Among them, two have attracted significant attention over the last years, namely, ferroelectric materials and microelectromechanical systems (MEMS). Both component families will be discussed in this chapter in terms of their physical structure, RF performance, and possible application in reconfigurable and tunable microwave circuits.

### 2.1. Ferroelectric Varactors

Ferroelectricity, as a phenomenon concerning crystals which exhibit an electrical field dependent polarization, was for the first time reported for Rochelle Salt<sup>1</sup> in the early 1920's [28]. Since then, a vast number of ferroelectric materials have been reported, investigated, and used in electric or electronic systems for many decades. One field of application for ferroelectric components is the fabrication of memory devices [29], such as dynamic random access memory (DRAM) elements [30], [31]. Ferroelectric properties have also been investigated for non-solid materials, such as ferroelectric liquid crystals [32], [33]. These materials are well known from their use in liquid crystal displays (LCD) and have an intermediate state between a crystalline solid and a normal isotropic liquid. As opposed to regular isotropic liquids, these materials have a specific degree of molecular order and can be categorized in different groups. Among them, the nematic phase liquid crystals exhibit electrical properties similar to the ferroelectric solids. Such types of liquids have been used in microwave systems, mostly for phase shifters [34] and electronically steerable antennas [35]. Despite their potential for use in higher frequency ranges, they exhibit a slow response to the electrical field variations. Nevertheless, the continuous progress in processing and manufacture techniques have reinforced the interest of researchers over the past years in particular for microwave applications.

Subject of this section will be the ferroelectric varactors which are based on Barium-Strontium-Titanate (BST) as a dielectric material. Among the numerous ferroelectric candidates, BST appears to be the most appealing one since it exhibits

---

<sup>1</sup>Rochelle Salt is the common description for sodium potassium tartrate tetrahydrate  $NaKC_4H_4O_6 \cdot 4H_2O$ .

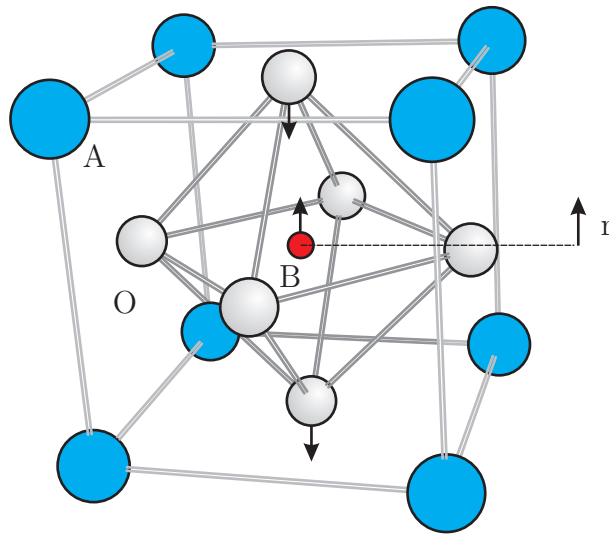


Figure 2.1.: Perovskite type crystal of the general form  $ABO_3$ .

high permittivity values and low intrinsic losses [36], [37]. BST is a composite material, consisting of Barium- and Strontium-Titanate forming a mixed crystal of the general form  $Ba_xSr_{(1-x)}TiO_3$ . The mixing ratio  $x$  has a significant impact on the overall electrical properties since it determines the transition point between the ferroelectric and the paraelectric phase within the crystal [38]. This mixed crystal belongs to the Perovskite<sup>2</sup> type structures and its geometry is depicted in Fig. 2.1. It is a centrosymmetric, namely cubic, structure of the general form  $ABO_3$ , where  $A$  is a monovalent or divalent metal and  $B$  is a tetra- or pentavalent metal. The atoms  $A$ , in this case Barium ( $Ba$ ) or Strontium ( $Sr$ ), are located at the cube corners. The atoms  $B$ , namely Titanate  $Ti$ , are located at the body center while the oxygen atoms  $O$  have their position at the face centers.

In absence of an external electrical field the perovskite type BST crystal remains centrosymmetric and the small Titanate ion is located at the center of the cubic structure. By applying an electrical field the Titanate ion is moved out of its stable position causing a nonlinear variation in the polarization of the material. This movement is related to the applied electrical field and causes a field dependent behavior of the material. By moving the center atom out of its stable position, the crystal becomes asymmetric which under certain conditions gives rise to noticeable piezoelectric effects. The field and temperature dependent properties of this material will be discussed on the basis of ferroelectric thin-film varactors in the following section.

<sup>2</sup>Perovskite is a mineral with chemical formula  $CaTiO_3$  and belongs to the oxygen octahedra crystals.

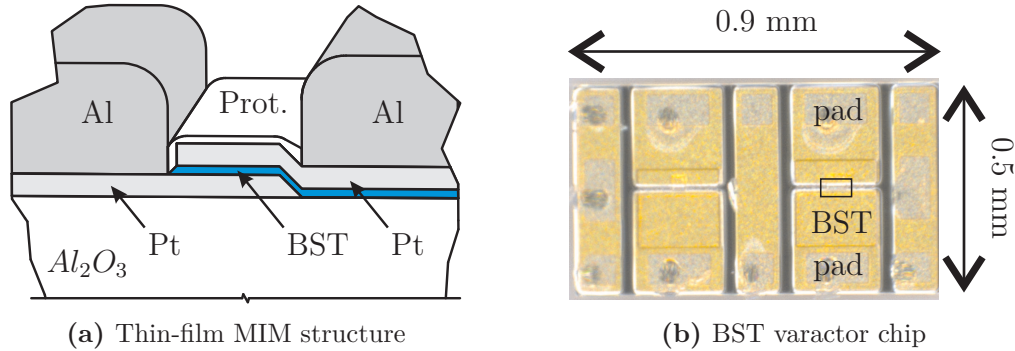


Figure 2.2.: Ferroelectric thin-film varactor in a metal-insulator-metal (MIM) structure and top view of used BST varactor chips.

### 2.1.1. Thin-Film Varactors

In this work, ferroelectric thin-film varactors are used as tuning elements for designing frequency agile microwave circuits. Thin-film varactors typically have the structure of the well known parallel plate capacitor, as indicated in Fig. 2.2(a). For this metal-insulator-metal (MIM) capacitor, the ferroelectric film of height  $d=300$  nm is located between the two metal electrodes. In this case, platinum (Pt) is the electrode metal, which is covered by an additional aluminum (Al) layer. Platinum is the most common choice for the electrode material, although it suffers from low conductivity, since it can be easily sputtered on the BST surface and annealed at high temperatures [39]. Different electrode materials, like copper and gold, and layer configurations have been reported as well [40], [41] leading to similar results. The choice of the electrode material is important in terms of the overall component performance. Early observations made clear, that the dielectric loss is influenced by the electrode material and the film thickness [42]. One approach aiming to explain this effect is based on the so called dead-layer theory [43], [44], [45]. Core assumption is the presence of intense space charge fields near the interface between ferroelectric material and metal electrode. The active area of the parallel plate capacitor is furthermore covered with a protecting isolating layer. The whole material stack is based on a ceramic alumina ( $Al_2O_3$ ) substrate. In Fig. 2.2(b), the top view of the actually used BST chips is presented. The active capacitor area of the MIM varactor is highlighted with a box and indicates the very compact dimensions which can be achieved. In this case, the zero bias capacitance is 5 pF. The MIM capacitor occupies only a small portion of the whole chip area. The by far larger portion is used for the electrode metalization and the pads. An electrical field  $\vec{E}$  is built by applying a bias voltage  $V$  on the electrodes. This field, which is straight forwardly related to the bias voltage, alters the permittivity of the BST film and can be described in a mathematical manner [46], [47]. For the discussed parallel plate structure, the voltage dependent capacitance  $C(V)$  can be described

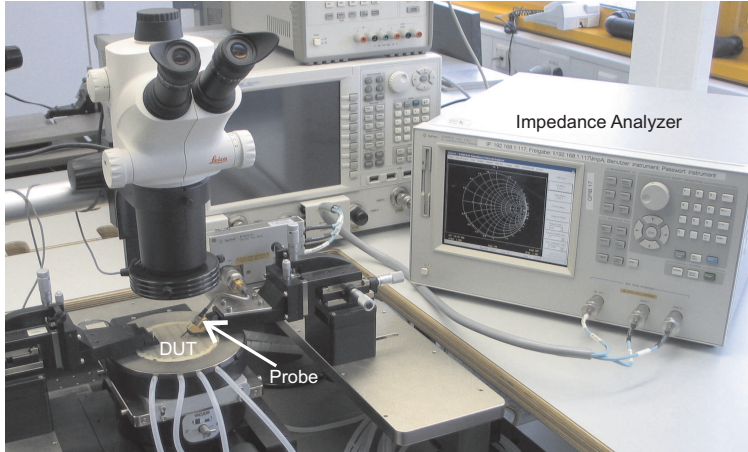


Figure 2.3.: On-wafer measurement setup for characterizing the ferroelectric varactors.

by a closed formula of the following form

$$C(V) = \frac{C_{max}}{2 \cosh\left(\frac{2}{3} \sinh^{-1}\left(\frac{2V}{V_{Cmax/2}}\right)\right) - 1}. \quad (2.1)$$

In (2.1),  $C_{max}$  and  $V_{Cmax/2}$  are the maximum capacitance and voltage where the capacitance reaches 50% of this value, respectively. The measurements were taken with an Agilent E4991A RF impedance analyzer [48] for frequencies up to 3 GHz by an on-wafer setup which is depicted in Fig. 2.3. An appropriate SOL (Short Open Load) calibration [49] was performed prior to the characterization. A comparison between modeled and measured capacitance of a BST varactor for different bias voltages is depicted in Fig. 2.4. The capacitance value  $C$  as well as the varactor quality factor  $Q$  were extracted from the measured input admittance  $Y$  according to the following set of equations.

$$C = \frac{\Im\{Y\}}{2\pi f} \quad (2.2)$$

$$Q = \frac{\Im\{Y\}}{\Re\{Y\}} \quad (2.3)$$

The maximum capacitance is always obtained at zero bias. For higher temperatures the relative permittivity  $\epsilon_r$  is decreasing, as predicted by the Ginzburg-Landau theory [50], since the temperature in the crystal moves far away from the phase transition point. Therefore the obtained capacitance is reduced as indicated in Fig. 2.5. At low temperatures a tunability, defined as  $(\epsilon_{rmax} - \epsilon_{rmin})/\epsilon_{rmax}$ , of more than

60% is achieved at a bias voltage of 20 V. In contrast to that, the varactor quality factor is increasing with rising temperatures, as shown in Fig. 2.6.

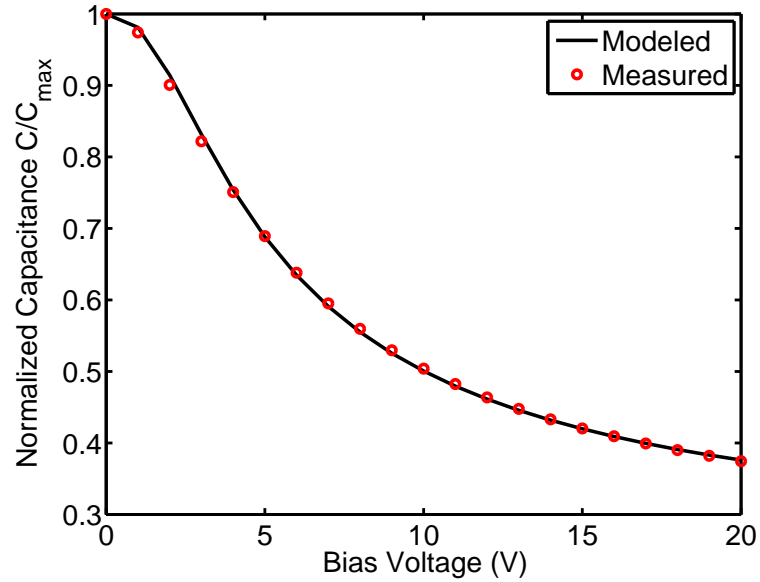


Figure 2.4.: Modeled and measured capacitance of a BST varactor with a zero bias capacitance of 5 pF.

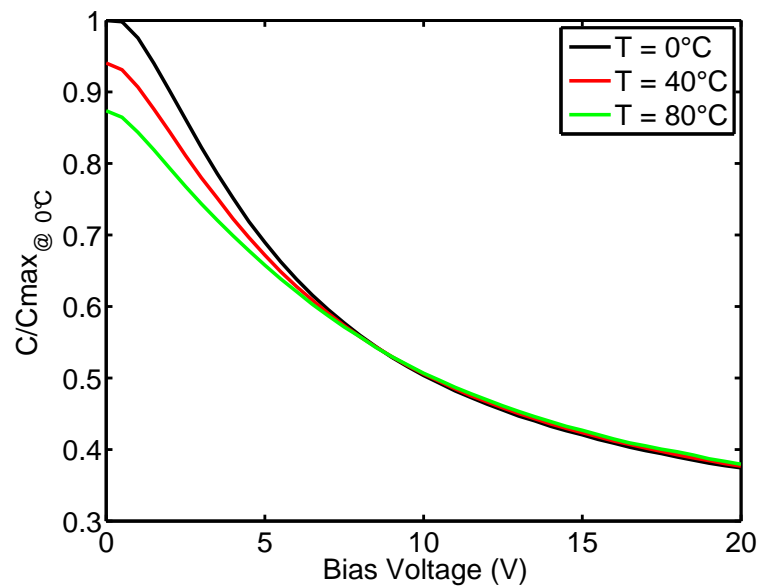


Figure 2.5.: Measured capacitance of a BST varactor with a zero bias capacitance of 5 pF at different temperature conditions.

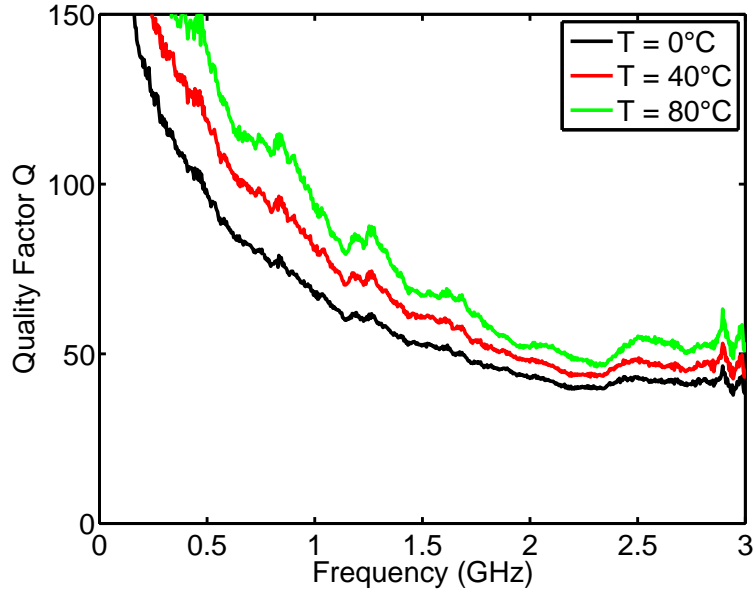


Figure 2.6.: Measured quality factor of a BST varactor at zero bias for different temperature conditions.

An additional phenomenon, that takes place when a bias voltage is applied, are the induced acoustic resonances. The perovskite-type BST crystal is symmetric in absence of an electrical field. By applying a bias voltage the crystal becomes asymmetric, thus piezoelectric, and introduces a parasitic resonance to the layered structure [51], [52]. In Fig. 2.7, at zero bias, the varactor quality factor  $Q$  is continuously declining over the operating frequency, as expected for a reactive element such as a capacitor.

As opposed to that, in Fig. 2.8, for a bias voltage of 20 V, there is a clear drop in the quality factor in the frequency region between 1.1 GHz and 1.5 GHz. This degradation in the quality factor is exactly due to the induced piezoelectric effects within the BST crystal. While for zero bias conditions the crystal structure is symmetric, it becomes asymmetric upon an applied electrical field and thus introduces stress to the crystal. The stress in the crystal structure causes a piezoelectric behavior which is expressed in terms of a lateral acoustic resonance for the parallel plate structure. The frequency allocation of this parasitic resonance depends on the acoustic properties of the electrode materials and the corresponding layer thicknesses [53], [54]. By comparing the modeled and measured quality factor curves good agreement is obtained for the zero bias case, whereas for applied bias some deviation occurs in the higher frequency range. The observed rise for the measured quality factors above 2.5 GHz are most likely due to the associated antiresonance of the parallel plate capacitor. This assumption becomes more reasonable by looking at the corresponding curve at zero bias since no similar effect is witnessed. During the period



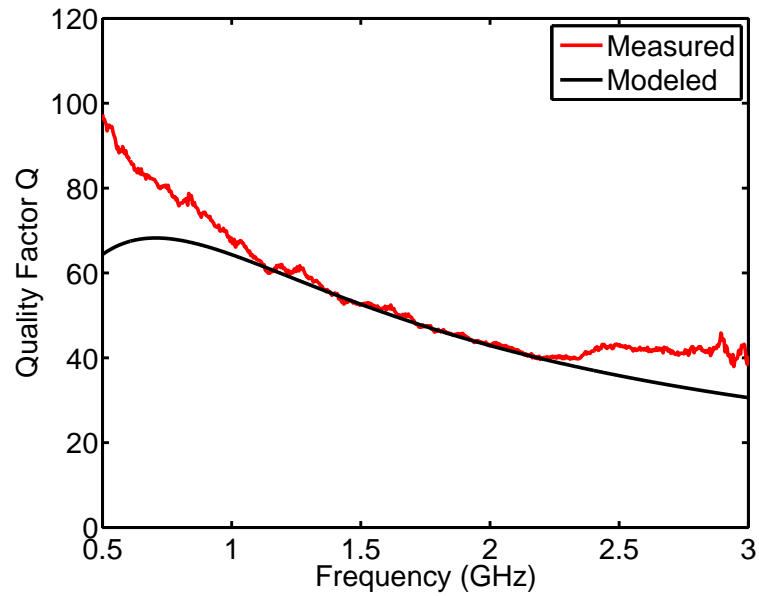


Figure 2.7.: Measured and modeled quality factor of BST varactor with a zero bias capacitance of 5 pF at zero bias.

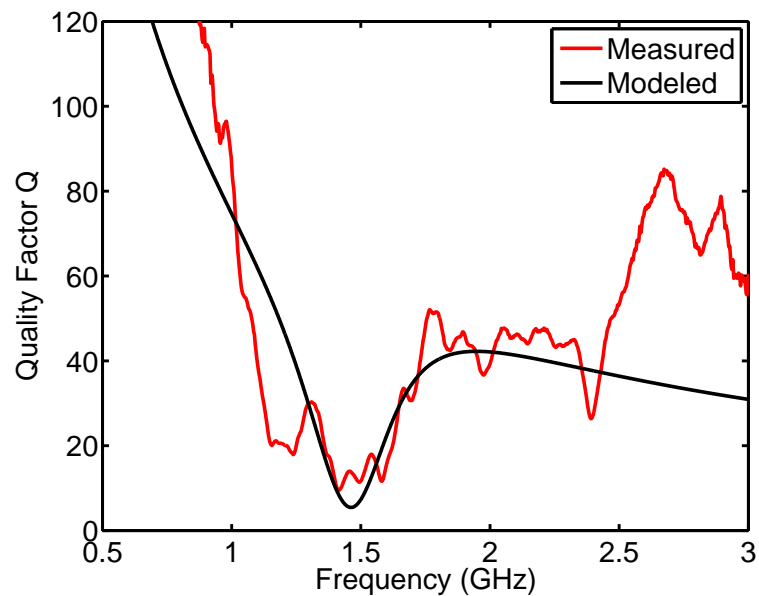


Figure 2.8.: Measured and modeled quality factor of BST varactor with a zero bias capacitance of 5 pF at bias voltage 20 V.

of the research project considerable effort by our industrial partner, namely the EPCOS AG, has been carried out in order to control this parasitic acoustic reso-

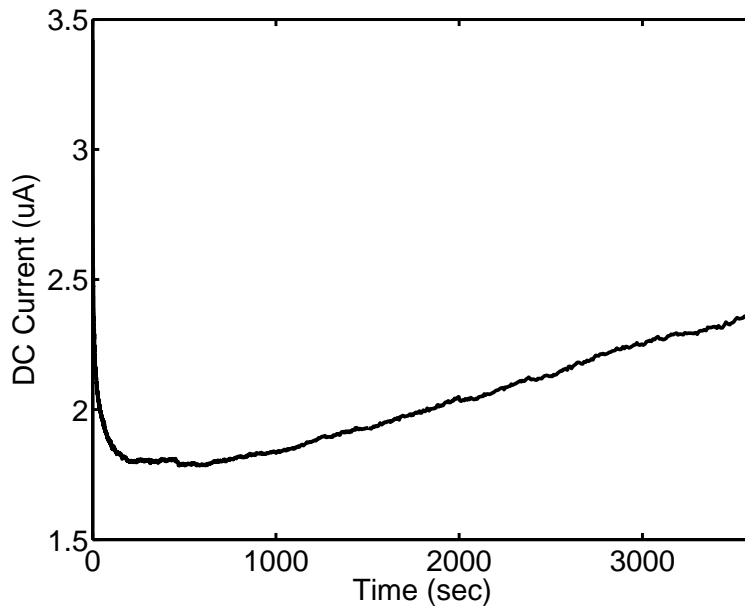


Figure 2.9.: Measured DC leakage current over a time period of 1 h at bias voltage of 20 V.

nance. As a result, the allocation of the resonance was placed in a frequency region where no critical communication bands have to be covered. The majority of the regulated communication bands are allocated around 0.8–1 GHz and 1.7–2.4 GHz. In these frequency regions, the worst case quality factors were around 40 at the higher frequency band. Although this is still a moderate performance, all circuits which are investigated in this work have been dimensioned for this frequency range around 2 GHz. The reason is simply the high density of regulated communication bands which have to be covered in this frequency region. Designing frequency agile and reconfigurable microwave circuits for these frequencies would be a step towards the previously defined goal of reducing the radio front-end complexity. As already stated before, the target application for reconfigurable microwave circuits is the integration in mobile communication devices. Aspects such as power consumption and voltage management are therefore of great significance. Theoretically the parallel plate structure has no power consumption since no static current is involved. Nevertheless, some leakage current is always associated with such structures. The transient response of the measured leakage current at the maximum bias voltage is given in Fig. 2.9. The obtained response is in line with previously reported data [55], [43]. Moreover, the polarization of the applied electrical field has an effect on the resulting leakage current as has been shown also in [56].

Specifications concerning linearity performance have to be investigated, moreover since for the discussed thin-film varactors DC and RF voltages are applied on the

same path. In other words, the RF voltage swing across the varactor terminals is somehow modulating the capacitance characteristic since a superposition of both voltages takes place. This effect can be quantified by considering the simulation setup of Fig. 2.10. An RF source produces a signal of certain power  $P_{in}$  and is fed to a 1 pF BST varactor, which is shunted at the other end. Additionally a bias voltage  $V_{Bias}$  is applied to the varactor. Components such as a DC-block capacitor and one RF-choke inductor are used for establishing the proper biasing conditions. As stated before, since the two signals are applied on the same varactor pads a superposition of both voltages results in the overall voltage  $V_{in}$  which is present across the tunable component. The amplitude of the RF signal that is added to the bias voltage depends on the signal power  $P_{in}$  and the position of the component within the network. Since the breakdown voltages of the investigated ferroelectric varactors were determined to be higher than 30 V, care has to be taken when operating at higher power levels. As indicated in Fig. 2.11, for rising power levels the added RF voltage swing reaches significant levels and could cause damage to the component. Furthermore, the superposition of both voltages causes somehow a modulation of the varactor capacitance around its operating DC point. A time variant varactor capacitance causes distortion and gives rise to nonlinear effects. This mechanism will become even more severe when considering operation with non constant envelope modulated signals. At this point it should be noted that a time variant RF signal, which passes the varactor, will not increase instantaneously the voltage swing according to the relation  $V_{RF} \propto \sqrt{P}$  since the frequency is also an important factor. Ferroelectric films exhibit time responses of several nanoseconds [57] and thus will not reply immediately causing a variation of the permittivity. Regardless of the response time, a certain degree of modulation will finally occur for the varactor capacitance. This mechanism is the primary reason for the nonlinear effects, which are associated with ferroelectric thin-film varactors.

One possibility to decrease these strong nonlinearities would be to design ferroelectric varactors with a smaller tuning ratio. Such components would exhibit tuning curves with a reduced capacitance slope. Applying an RF signal of the same power level to the varactor would produce smaller variations of the capacitance value, thus reduced nonlinearities. Nevertheless, this technique has a significant drawback which is caused by the reduced tuning ratio of the varactor capacitance. As will become clear in the next chapters, a high tuning ratio is essential for designing frequency agile and reconfigurable microwave circuits. A second more promising technique is the cascaded connection as depicted in Fig. 2.12, which relies on the simple voltage divider principle. By connecting several varactors in series and applying the proper biasing according to [58], an equivalent structure to Fig. 2.10 is obtained. In a first approximation the bias feeding lines can be ignored since they provide a high impedance path to the RF signal. Since the varactors are cascaded the total capacitance of the structure is given as

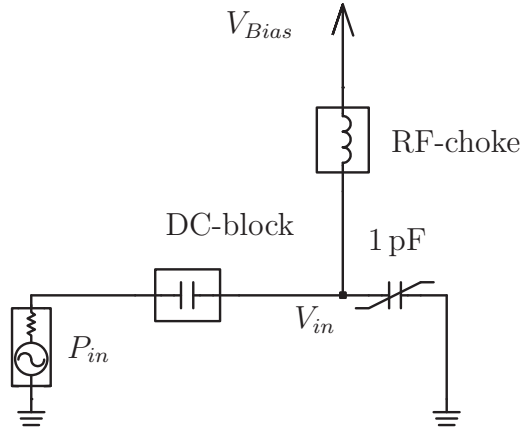


Figure 2.10.: Simulation setup of a 1 pF BST varactor with applied bias voltage  $V_{Bias}$  and RF signal of power  $P_{in}$ .

$$\frac{1}{C_{total}} = \frac{1}{C_1} + \frac{1}{C_2} + \dots + \frac{1}{C_n}. \quad (2.4)$$

In order to obtain the same equivalent capacitance as the original capacitor, the individual capacitors must have  $n$  times the initial capacitance, thus

$$C_1 = C_2 = \dots = C_n = nC. \quad (2.5)$$

The effect of the in series connected varactors is that the RF voltage is equally distributed over the varactors, thus a reduced voltage  $V_{ser}$  is resulting for each individual element. In Fig. 2.13 the corresponding peak to peak voltage swing for an RF power of 20 dBm drops to 2.5 V, compared to the value of 12.5 V in Fig. 2.11. It becomes evident that cascading many capacitors leads to rapidly rising capacitance values for the individual varactors. Nevertheless, for ferroelectric thin-film varactors this is still feasible since the high capacitance density of the parallel plate structure allows for implementations of large capacitances at considerably compact dimensions. In practical implementations the biasing circuitry appears to be more challenging since high impedance connections are needed. Finally, a combination of the large capacitance values and the needed high impedance biasing lines will introduce limitations to such structures.

A two-tone test (see Appendix B) was used in order to quantify the nonlinear effects associated with this type of ferroelectric thin-film varactors. A comparison between the experimental results and the simulation data provided by the equivalent model from [59] is given in Fig. 2.14. Excellent agreement is obtained for the fundamental tone while some deviation occurs for the intermodulation power levels. In particular, for lower signal power levels the measured intermodulation products exhibit a slope that differs from the simulated one. The expected inter-

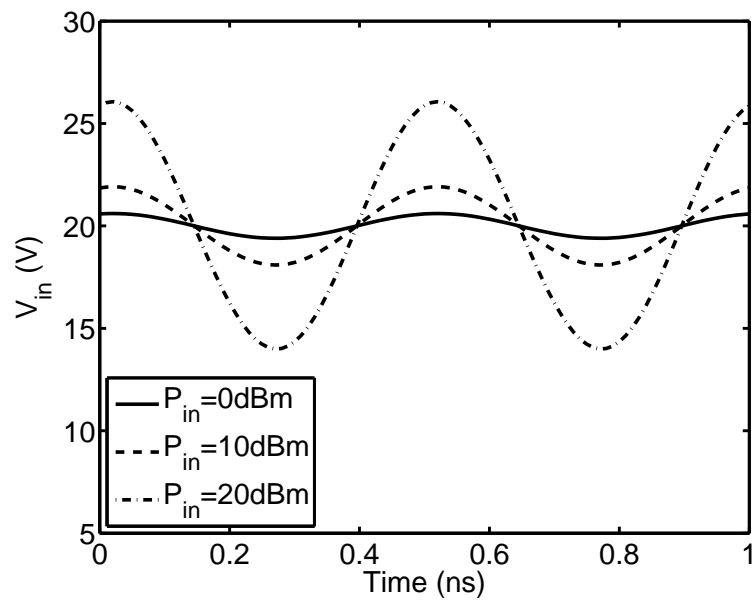


Figure 2.11.: Time domain response of input voltage  $V_{in}$  for an applied RF signal of frequency  $f=2\text{ GHz}$  and varying RF power levels. The bias voltage is set to  $V_{Bias}=20\text{ V}$ .

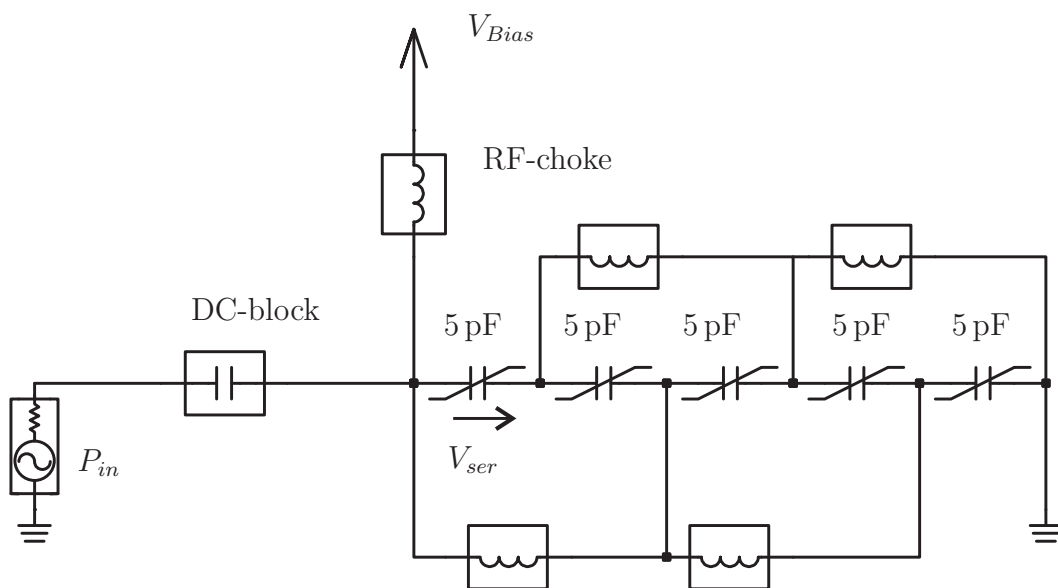


Figure 2.12.: Simulation setup of a series combination of 5 pF BST varactors with modified bias circuitry for applying  $V_{Bias}$ .

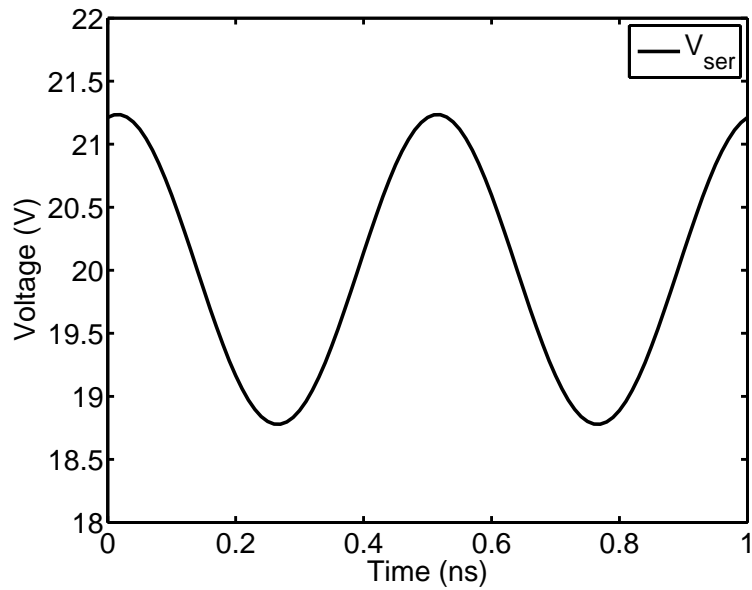


Figure 2.13.: Time domain response of voltage  $V_{ser}$  for an applied RF signal of frequency  $f=2$  GHz and RF power of 20 dBm. The bias voltage is set to  $V_{Bias}=20$  V.

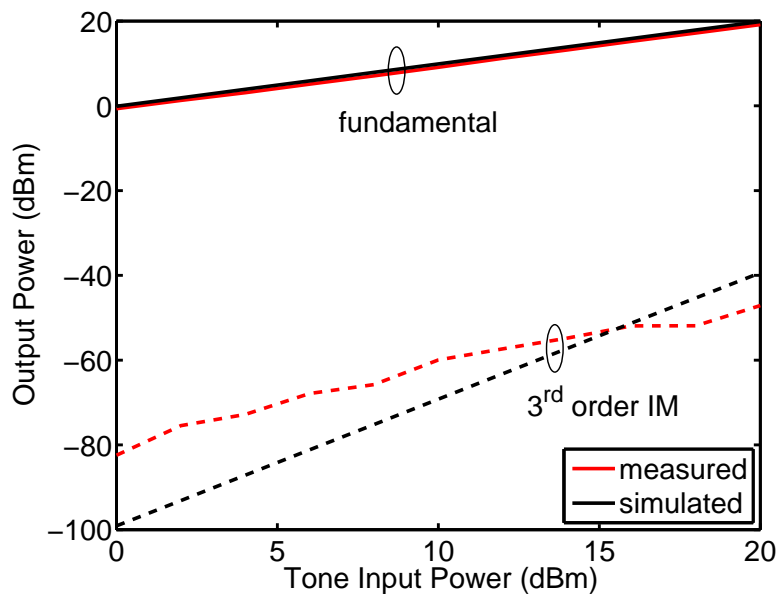


Figure 2.14.: Measured and simulated output power levels for the fundamental tone and the 3<sup>rd</sup> order intermodulation products for a two-tone measurement setup with frequencies  $f_1=1948$  MHz and  $f_2=1952$  MHz.

modulation products should rise with a factor of 3 compared to the linear behavior of the fundamental tone. This deviation for lower power levels is caused by the limited dynamic range of the measurement setup. The overall RF and acoustic behavior of BST thin-film varactors can be described by equivalent models, e.g. with Van Dyke's [60] and Butterworth's [61] approach, thus allowing for accurate linear and nonlinear simulations during the circuit design procedure. Having implemented such equivalent circuit models in commercially available design tools is the first step towards systematic investigations on frequency agile and reconfigurable microwave circuits. In this work, the circuit model from [59] is implemented in Agilent's Advanced Design System (ADS), which serves as the design tool for the microwave circuits, which will be discussed in the following chapters.

### 2.1.2. Interdigital Varactors

Besides the aforementioned parallel plate MIM structure, ferroelectric varactors can also be fabricated as planar capacitors. The geometry which is used in that case is based on the interdigital capacitor structure, as presented in Fig. 2.15(a).

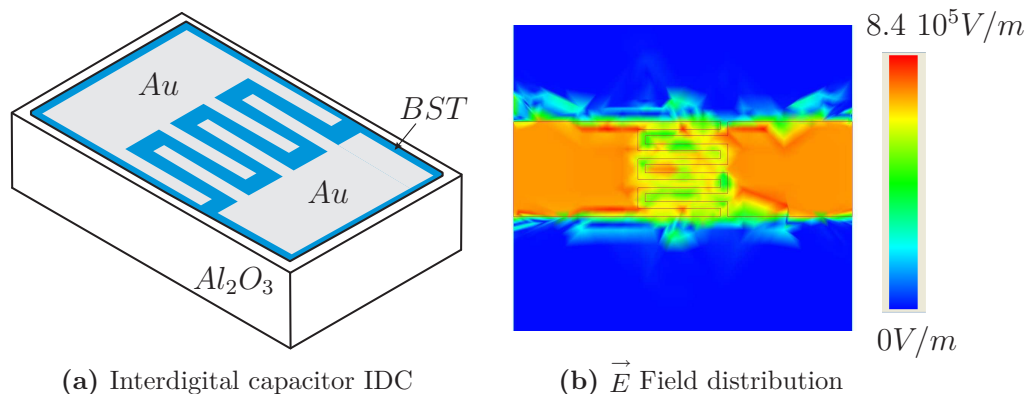


Figure 2.15.: Planar interdigital capacitor processed on a ferroelectric thick-film layer and the corresponding electric field distribution. Data computed by 3D electromagnetic field simulation in Agilent's EMDS tool.

Ceramic substrates are used as carriers for deposition of the ferroelectric bulk material [62]. Metal electrodes, mostly *Au* metalizations, are then chemically structured on the ferroelectric layer. A detailed description and investigation of such components is given in [63]. As opposed to the parallel plate capacitor, the electrical field is only partially passing through the ferroelectric material. Part of it is distributed through the air gap between the finger electrodes as depicted in Fig. 2.15(b). The wider spacing between the finger electrodes results in higher DC bias fields, which have to be applied in order to reach field density values which are comparable to the MIM capacitor. Bias voltages of approximately 100 V

are required for such components while the tunability is still moderate, typically around 30%. Latest results demonstrated enhanced performance in terms of tunability [64], as a consequence of coating the planar metal electrodes with polymer filling materials such as Parylene. Moreover, the interdigital capacitors allow for implementations with separated DC feed structures. Examples of such varactors have been reported in [65] using high resistive electrodes. Higher bias voltages along with the separated DC pads result in enhanced linearity performance for this type of ferroelectric varactors. As drawbacks remain the overall high bias voltages, which make the use in handheld devices hardly realizable. Moreover the limited maximal capacitance values of 2 pF, which have been reported for these components, introduce further limitations. Nevertheless, due to their good RF performance and simple manufacturing technology they remain an attractive solution for reconfigurable microwave circuits.

## 2.2. Microelectromechanical Systems – MEMS

Microelectromechanical systems became practical with the continuous progress witnessed in the fabrication of integrated circuits (IC). The ability to process structures on a micrometer scale by techniques of photolithography and chemical etching [66] disclosed a new field of applications, namely the micromachinery. Opposed to two dimensional surface structures of conventional IC's, microelectromechanical structures are based on three dimensional components. For this purpose two processing procedures were introduced, namely bulk- and surface micromachining [67]. Bulk micromachining concerns the creation of mechanical structures in the wafer bulk rather than on its surface. This is achieved by selectively removing some parts of the wafer or substrate material. However, more advanced techniques have been recently developed which are based on surface micromachining and a process called LIGA (Roentgen **L**ithografie **G**alvanik **A**bformung) [68]. MEMS components are inherently associated with mechanical movement, thus the actuation mechanism has a significant contribution to the overall behavior. The most common actuation mechanisms are based on electrostatic forces [69] and piezoelectric effects [70], [71]. Reliability is one important issue associated with MEMS devices since mechanical movement is involved. Switching cycles in the order of magnitude  $10^9$  have been reported, as well as operation with high power levels [72]. All of the aforementioned techniques introduced a whole new family of components based on a microelectromechanical approach. The most common structures that have been presented are inductors [73], [74], switches [75], [76], actuators [77], and varactors [78], [79], which will be the subject of investigation in the following section.



### 2.2.1. MEMS Varactor

The varactor component, which will be investigated in this work, is a rather macro scale electromechanical varactor from Siemens Corporate Technology in Munich and it comprises of a piezoelectrically actuated cantilever structure, as shown in Figs. 2.16 and 2.17. Construction details are presented in [80]. The whole layer stack is based on a ceramic substrate (LTCC) and a conductive path is provided through vias to the backside of the LTCC substrate.

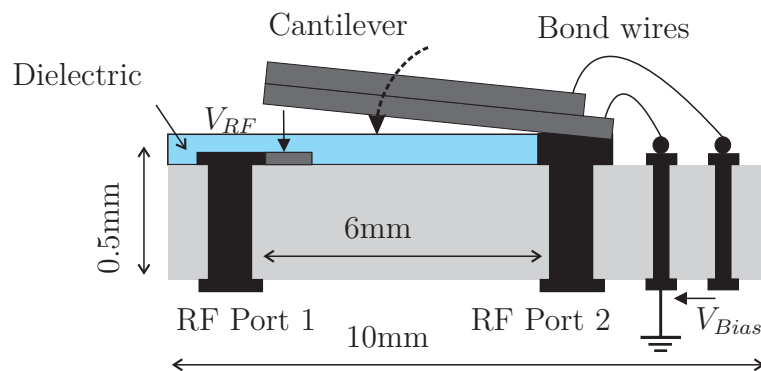


Figure 2.16.: Cantilever MEMS varactor.

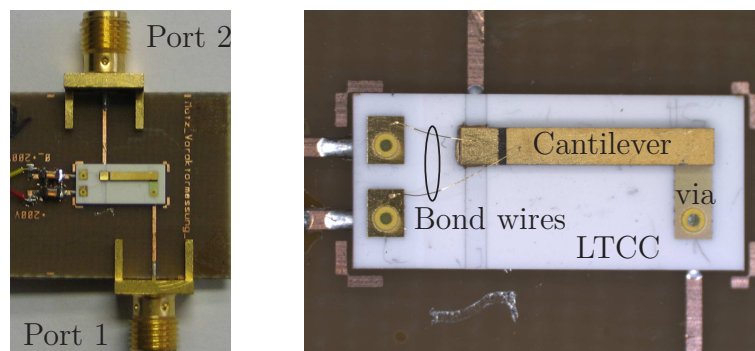


Figure 2.17.: Photograph of the MEMS varactor test board and magnified top view.

The upper electrode includes lead-zirconate-titanate (PZT) material and forms a cantilever which bends down due to piezoelectric activation. The tuning voltage  $V_{Bias}$  can be varied between 0 and 200 V, corresponding to an air gap in the range of 20 and  $0\ \mu\text{m}$  between the top and bottom RF electrodes, which are directly attached to the two RF ports. That means increasing the tuning voltage leads to larger bending and thus a smaller gap resulting in increased capacitance. By that a continuously tunable varactor is obtained. Besides this wanted piezoelectrical actuation there is a secondary unwanted electrostatic actuation caused by an

electrostatic force between the two RF electrodes forming the capacitance. By applying a large RF voltage, a parasitic electrostatic force pulling down the cantilever is found. As this force is proportional to  $V_{RF}^2$  it is always pulling down. This mechanism of self actuation by the carried RF signal is the main cause for nonlinearities in the RF path of the varactor. Electrostatic forces tend to be much smaller than piezoelectric ones, leading to very minor bending of the cantilever. The cantilever can also be treated as a mechanically oscillating system associated with a moving mass, a spring constant and damping by the air in the gap. From analysis of the mechanical dynamic properties a mechanical resonance frequency around a few kHz is found. For any wideband modulated signal that has larger bandwidth than the mechanical resonance, e.g. UMTS with 5 MHz channels, the nonlinear distortions due to self actuation are very low. The inertia of the mechanical system is too high to follow the fast envelope fluctuations. The highest capacitance is observed when the cantilever is most down and facing the dielectric layer that is capping the lower RF electrode. A parallel plate capacitor with distance  $d_k$  equal to the thickness of the dielectric capping layer,  $\varepsilon_k$  of the capping layer and area  $A$  equal to the electrode size of  $1 \text{ mm}^2$  is formed. The capacitance can be expressed as

$$C = \frac{\varepsilon_k \varepsilon_0 A}{d_k}. \quad (2.6)$$

Due to separation of the RF signal and the bias path it is possible to use the varactor in series configurations without additional circuitry such as bias-tees. This is a nice feature since this type of components would contribute to a degradation of the RF circuit performance.

Designing high performance microwave circuits is impractical without having appropriate models, which can be used in commercially available design tools. In our case we use Agilent's Advanced Design System (ADS) for implementing an equivalent circuit model, as in [59]. The core element of the proposed model is the symbolically defined device (SDD), as it is available in the ADS library. These SDD objects are powerful elements since they allow for implementation of equation based, user defined, nonlinear, and frequency dependent components as in [81], [82]. They can be used as multi-port elements and describe the relationship between port voltages and associated currents and their time derivatives along with currents from other devices. For an SDD device with  $n$  ports, the current at any port can be described in dependence of all other port voltages, as

$$i = f(v_1, v_2, \dots, v_n), \quad (2.7)$$

where  $f$  is a user defined function. In case of the investigated MEMS varactor the overall capacitance is described as

$$C = \frac{\varepsilon_0 A}{\frac{d_k}{\varepsilon_k} + g + z}. \quad (2.8)$$

In (2.8) the denominator includes all parameters which determine the cantilever movement and thus the distance between the two capacitor electrodes. The air gap  $g$  is directly proportional to the applied bias voltage and can be described by the following relation

$$g = g_{max} - (V_{Bias} + aV_{RF})b. \quad (2.9)$$

The constant  $a$  accounts for the crosstalk between the RF and DC path, while  $b$  is a constant determined by the cantilever geometry. The parameter  $z$  stands for the vertical movement of the cantilever tip and is related to the mechanical properties of the cantilever electrode. Considering the cantilever motion as a system with a single degree of freedom, allows for a simple representation with a differential equation of the following form [83].

$$M\ddot{z} + D\dot{z} + Kz = F_{el}(t) \quad (2.10)$$

In (2.10)  $M$  is the moved top electrode mass,  $D$  is the damping constant,  $K$  the stiffness parameter, and  $F_{el}(t)$  the parasitic actuating force. In this case,  $F_{el}$  is the electrostatic force. For a parallel plate capacitor with applied voltage  $V_{RF}$ , the stored energy is given as

$$W = \frac{1}{2}C_0V_{RF}^2, \quad (2.11)$$

where, in this case the capacitance is  $C_0 = \varepsilon_0 A / ((d_k / \varepsilon_k) + g)$  and the associated electrostatic force is then

$$F_{el}(t) = \left| \frac{dW(t)}{dg} \right| = \frac{\varepsilon_0 A V_{RF}^2}{2(d_k / \varepsilon_k + g)^2}. \quad (2.12)$$

Combining (2.9), (2.12) and (2.8) yields to the expected relation between bias voltage, cantilever movement, and the resulting capacitance variation.

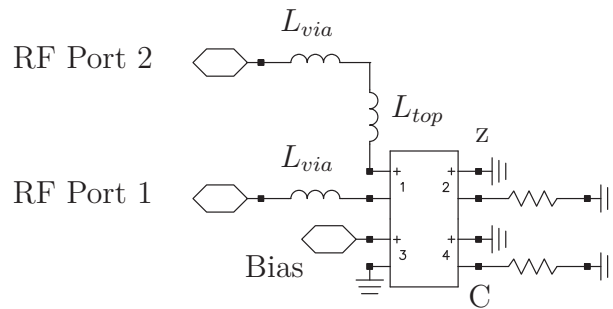


Figure 2.18.: Implemented MEMS varactor model using an ADS SDD element [84].

The implemented model using an ADS SDD element is depicted in Fig. 2.18. Both RF ports are connected through inductive elements to connector pair 1 of the SDD.

The lumped inductances account for the top electrode and the vias connections. The formed air gap and its relation to the applied bias voltage and RF signal according to (2.9) is formed at connector pair 3. Connector pair 2 of the SDD element is used for describing the cantilever movement parameter  $z$ , according to (2.10) and (2.12). Finally, at connector pair 4 of the SDD the overall varactor capacitance is described as in (2.8), taking into account all the aforementioned effects. Expressed in an ADS syntax the corresponding set of equations for the SDD element have the following form.

$$\begin{aligned}
I[1,1] &= \_v1 * i\_4 \\
F[2,0] &= (0.5 * \text{eps}0 * A / (d\_k / \text{eps\_k} + i\_3)^2) * \_v1^2 \\
F[2,0] &= k * i\_2 \\
F[2,1] &= \text{gamma} * i\_2 \\
F[2,2] &= M * i\_2 \\
H[2] &= -4 * \text{Pi}^2 * \text{freq}^2 \\
F[3,0] &= g_{\text{max}} - ((\_v3 + a * \_v1) * b) - i\_3 \\
F[4,0] &= \text{eps}0 * A / (d\_k / \text{eps\_k} + i\_2 + i\_3) - i\_4
\end{aligned}$$

The MEMS component was characterized by scattering parameter measurements which were taken with a vector network analyzer (VNA). The capacitance  $C$  of the varactor as well as its quality factor  $Q$  were calculated from the measured reactance, according to the relations

$$C = \frac{\Im\{Y_{21}\}}{2\pi f} \quad (2.13)$$

$$Q = \frac{\Im\{Y_{21}\}}{\Re\{Y_{21}\}} \quad (2.14)$$

where  $Y_{21}$  is the admittance of the transmission path. For the capacitance variation a comparison of measured and simulated data for different bias voltages is presented in Fig. 2.19. A large tuning ratio of more than 5:1 reveals the potential of using this element in tunable microwave circuits. The SDD model parameters were fitted appropriately to the measured reactance data of the varactor, leading to accurate modeling for the investigated frequency range, as indicated in Fig. 2.20. The good agreement qualifies the model for use in circuit simulations for designing microwave circuits with tunable or reconfigurable characteristics.

The measured quality factor values are displayed in Fig. 2.21 for different biasing conditions. Large fluctuations in the measured  $Q$  factors, especially for values greater than 70, are due to the limited capabilities of the network analyzer. For increasing quality factors the uncertainty of the network analyzer causes great variations. As it is readily seen, rapid degradation of the quality factor is taking place for higher frequencies. This is caused by the self resonance effect which occurs in

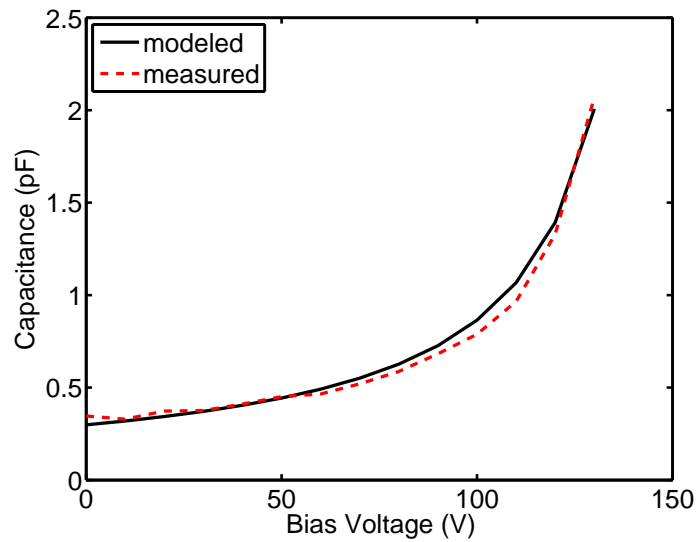


Figure 2.19.: Measured and modeled capacitance of cantilever varactor.

the frequency region below 1 GHz. The intrinsic self resonance of the varactor is expected to be at higher frequencies since the reference plane of the measurement setup included feeding microstrip lines of the test board as depicted in Fig. 2.17. Nevertheless, at lower frequencies the obtained quality factors allow for implementations of microwave circuits with reconfigurable or tunable characteristics.

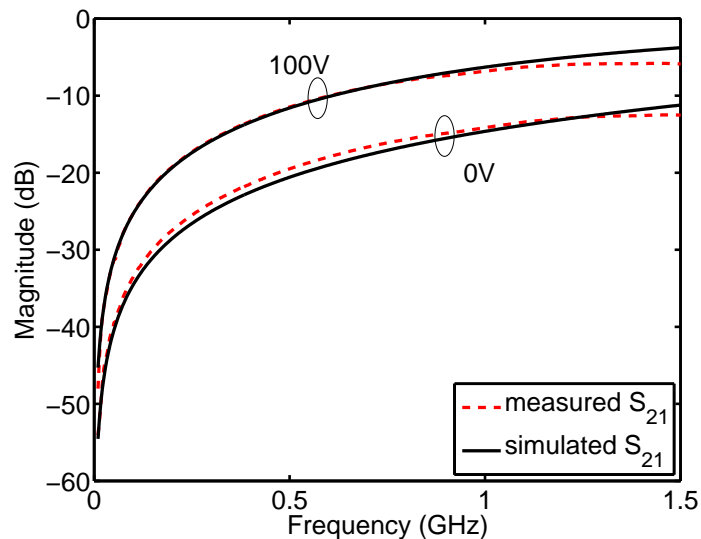


Figure 2.20.: Measured and modeled scattering parameters of MEMS varactor.

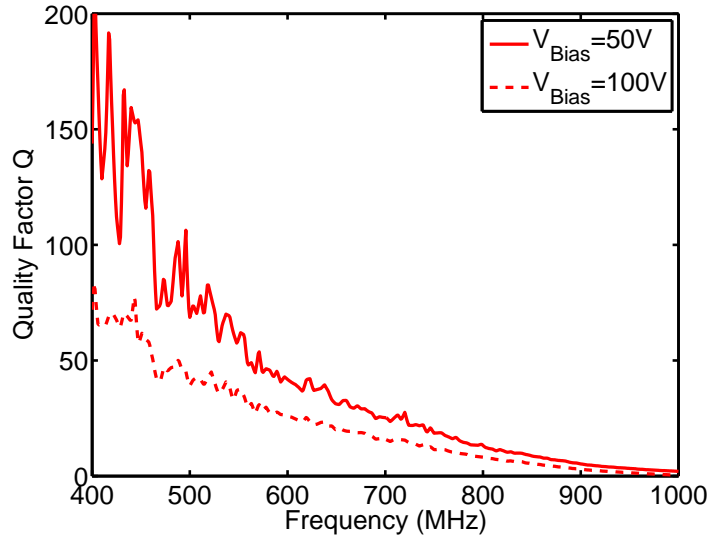


Figure 2.21.: Measured quality factor of MEMS varactor at different bias voltages.

Besides the capacitance variation and the frequency dependence, the varactor has to be characterized for its power handling capabilities. As can be seen in Fig. 2.22 the varactor performance can be described by the proposed model thus allowing for complete system investigations in circuit simulation tools at an early design stage. The MEMS varactor implies a mechanical movement of the piezoelectric cantilever as described in (2.10). This mass electrode system is characterized by a certain inertia. The electrostatic force  $F_{el}$  is ruled by the applied RF signal and its frequency, thus the cantilever movement will be also frequency dependent. Applying two sinusoidal tones of the following form  $V_{RF} \sin(\omega_1 t)$  and  $V_{RF} \sin(\omega_2 t)$ , would result according to (2.12) in an electrostatic force

$$F_{el}(t) \propto (V_{RF} \sin(\omega_1 t) + V_{RF} \sin(\omega_2 t))^2 \quad (2.15)$$

$$\propto V_{RF}^2 [\sin^2(\omega_1 t) + \sin^2(\omega_2 t) + 2 \sin(\omega_1 t) \sin(\omega_2 t)] \quad (2.16)$$

$$\propto V_{RF}^2 [\sin^2(\omega_1 t) + \sin^2(\omega_2 t) + \cos(\omega_1 t - \omega_2 t) - \cos(\omega_1 t + \omega_2 t)] \quad (2.17)$$

which depends on the tone distance. This relationship is investigated by the simulated data in Fig. 2.23. Varying the tone distance of a two-tone excitation, results in different frequencies for the mechanical cantilever movement. The resulting varying air gap of the MEMS varactor causes a modulation of the capacitance value and gives rise to intermodulation products. For both applied bias states there is a peak at 2.2 kHz where the cantilever movement reaches its resonance. For use in communication systems this condition should be rarely met, since the corresponding channel bandwidths are much wider. Therefore, interfering or blocking signals are unlikely to have such a narrow spacing which would cause high intermodula-

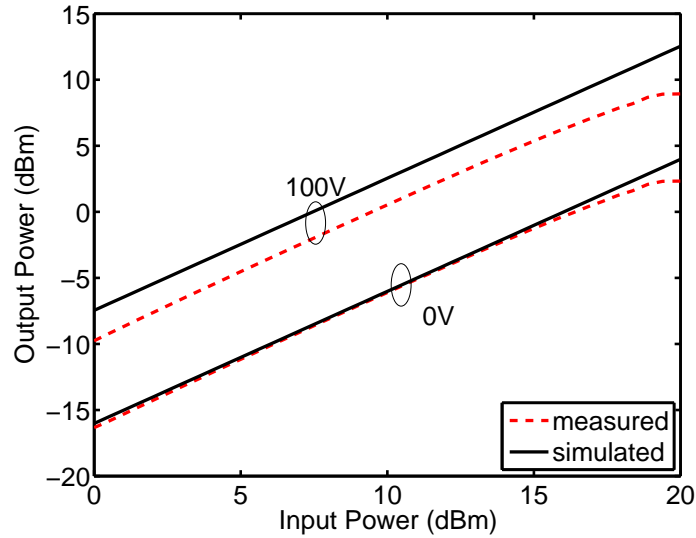


Figure 2.22.: Measured and modeled power handling of MEMS varactor at tone frequency of 850 MHz.

tion products. The excellent linearity provided by minimal self actuation effects qualifies the component for use in high power applications.

For the experimental verification a two-tone setup around the center frequency of 835 MHz with a tone distance of 5 MHz was selected. The measured response for the fundamental output tone and intermodulation products is depicted in Fig. 2.24. It is noteworthy that the measured power levels of the 3<sup>rd</sup> order intermodulation products are very low at all investigated bias states. As a result, they hardly exceed the noise level of the measurement setup, thus they can not be traced properly over the entire sweep range. The resulting intermodulation products are at least 70 dB lower than the fundamental tone over the whole power sweep range. It is evident that this cantilever MEMS varactor is very well suited even for high power microwave circuits since it exhibits excellent linearity [85]. Compared to ferroelectric varactors, the investigated MEMS element has a much higher tuning range while exhibiting even better linearity [86], [87]. This becomes even more evident when comparing these results with the previously discussed data of Fig. 2.14. At the same time, the high tuning voltages and the overall large component dimensions have to be considered as drawbacks compared to other technologies, namely ferroelectric components, which have a much higher potential for integration in mobile devices. Nevertheless, the overall performance in terms of capacitance tuning ratio and linearity performance qualify this type of MEMS varactor for designing reconfigurable microwave circuits with enhanced linearity specifications. Although the utilization in handheld devices appears to be impractical, the MEMS varactor is still an attractive solution for stationary devices with high power applications.

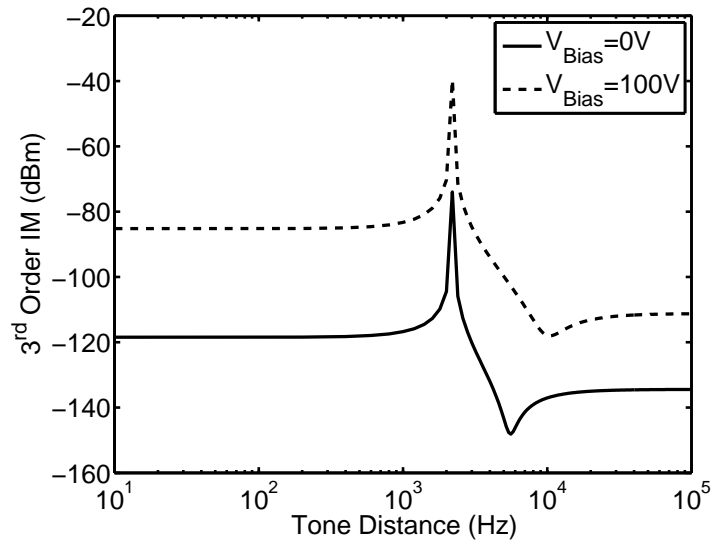


Figure 2.23.: Simulated data of the intermodulation product power levels for a two-tone excitation with varying tone distances. The per tone power level was set to a constant value of 20 dBm.

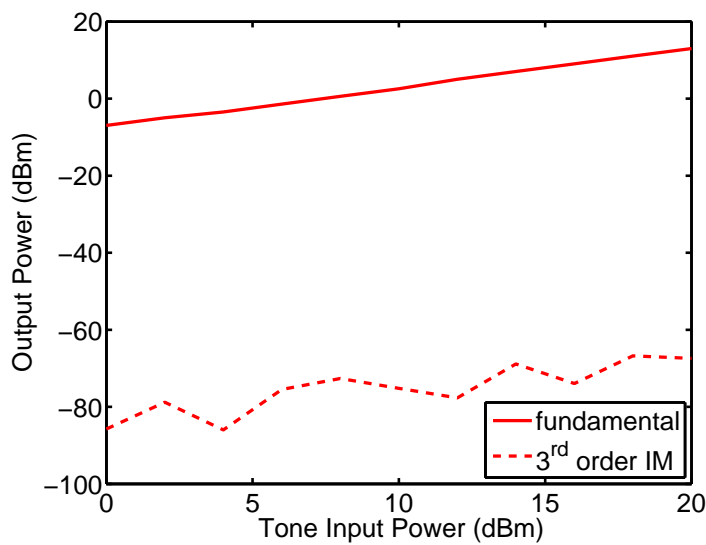


Figure 2.24.: Measured power levels of fundamental tone and  $3^{rd}$  order intermodulation product (IM) for a two-tone setup with a center frequency of 835 MHz and a tone distance of 5 MHz. The applied bias voltage is  $V_{Bias}=100$  V.



## 3. Frequency Agile Filters

The focus in this chapter lies on the principles of microwave filter design with lumped and distributed components. The potential of achieving frequency agile behavior based on tunable passive elements, as presented in Chapter 2, will also be addressed. Microwave filters have been used extensively in various applications over the last decades. The most obvious application is the rejection of unwanted signals in a specific frequency band, while allowing for a good transmission within the passband frequencies. Some basic filter structures, namely low-, high-, band-pass and bandstop filters, are the core structures for designing even more complex networks.

### 3.1. Network Synthesis Method

Numerous filter design techniques have been introduced since microwave filters have been investigated heavily over many years. Among all, the network synthesis method [88] appears to be the most appealing one, because it yields predictable network responses. In this section, this synthesis method is applied to the general lowpass filter structure depicted in Fig. 3.1. In this filter structure,  $g_0$  and  $g_{n+1}$  are

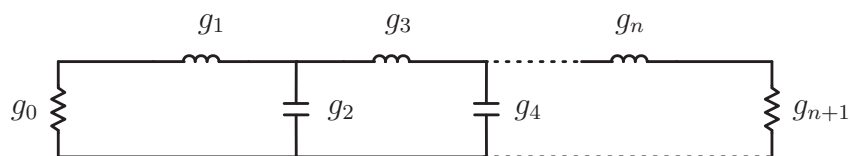


Figure 3.1.: General lowpass filter prototype.

the source and load conductances. For the general case these values are set to  $1 \Omega^{-1}$ , since the filter is designed for a port impedance of  $50 \Omega$ . The parameters  $g_k$ , where  $k=1\dots n$ , are the series inductances or the shunt capacitances. These values depend on the type of the selected transfer function. The most common type of functions are the maximally flat, also called Butterworth, and the Chebyshev type. The attenuation profile over the bandwidth of interest is described by the following set of equations. For a Butterworth characteristic, the frequency dependent attenuation

$A(\omega)$  can be described mathematically as

$$A(\omega) = 10 \log_{10} \left[ 1 + \epsilon \left( \frac{\omega}{\omega_1} \right)^{2n} \right] \quad (3.1)$$

$$\epsilon = 10^{\left(\frac{A_r}{10}\right)} - 1. \quad (3.2)$$

In the above equations,  $n$  is the filter order and  $A_r$  the attenuation level which is specified within the passband up to the corner frequency  $\omega_1$ . For the same parameters, the attenuation profile of a Chebyshev filter is given as

$$A(\omega) = 10 \log_{10} \left\{ 1 + \epsilon \cos^2 \left[ n \cos^{-1} \left( \frac{\omega}{\omega_1} \right) \right] \right\}, \quad \omega \leq \omega_1 \quad (3.3)$$

$$A(\omega) = 10 \log_{10} \left\{ 1 + \epsilon \cosh^2 \left[ n \cosh^{-1} \left( \frac{\omega}{\omega_1} \right) \right] \right\}, \quad \omega \geq \omega_1 \quad (3.4)$$

$$\epsilon = 10^{\left(\frac{A_r}{10}\right)} - 1. \quad (3.5)$$

The obtained response for these filter types is illustrated in Fig. 3.2. Although both

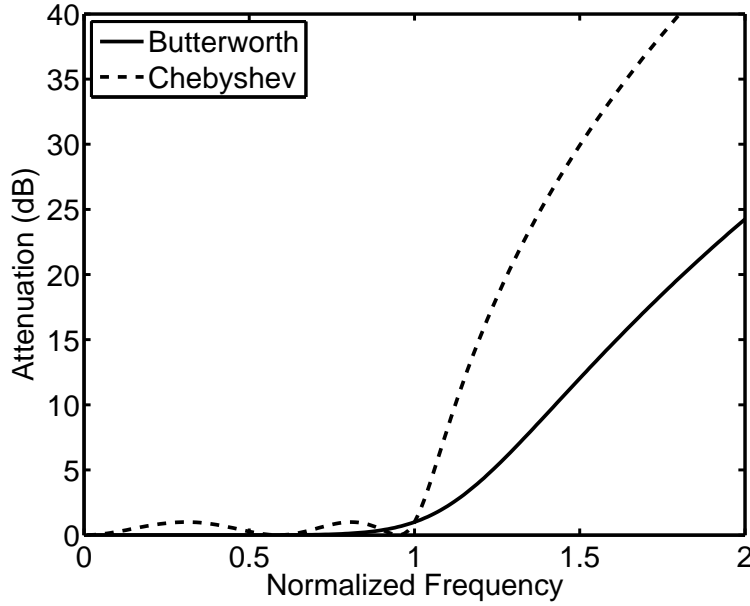


Figure 3.2.: Calculated attenuation profile for Butterworth and Chebyshev filter prototypes with the same corner frequency  $\omega_1$ , passband attenuation  $A_r=1$  dB, and filter order  $n=5$ .

filters have the same level of attenuation within the passband they exhibit a quite different behavior. The Chebyshev filter introduces ripple for the propagated signal in the passband compared to the Butterworth filter which has a smooth passband

profile. On the other hand, Chebyshev filters have a much steeper stopband transition leading to higher rejection of unwanted signals in the stopband region. The choice of the proper filter characteristic depends on the final application. Once this decision is made, e.g. for a Chebyshev type characteristic, the network element values can be derived from the following tables.

Order $n$	$g_1$	$g_2$	$g_3$	$g_4$	$g_5$	$g_6$
1	0.6986	1.0000	–	–	–	–
2	1.4029	0.7071	1.9841	–	–	–
3	1.5963	1.0967	1.5963	1.0000	–	–
4	1.6703	1.1926	2.2661	0.8419	1.9841	–
5	1.7058	1.2296	2.5408	1.2296	1.7058	1.0000

Table 3.1.: Normalized element values for Chebyshev filter having  $g_0=1$ ,  $\omega_1=1$ , and passband ripple 0.5 dB, according to [88].

Order $n$	$g_1$	$g_2$	$g_3$	$g_4$	$g_5$	$g_6$
1	1.0177	1.0000	–	–	–	–
2	1.8219	0.6850	2.6599	–	–	–
3	2.0236	0.9941	2.0236	1.0000	–	–
4	2.0991	1.0644	2.8311	0.7892	2.6599	–
5	2.1349	1.0911	3.0009	1.0911	2.1349	1.0000

Table 3.2.: Normalized element values for Chebyshev filter having  $g_0=1$ ,  $\omega_1=1$ , and passband ripple 1 dB, according to [88].

These normalized component values can be scaled for the desired corner frequency  $\omega$  and system impedance  $R_0$  according to the following set of equations. For resistances respectively conductances

$$R = \frac{R_0}{g_0} = R_0 \quad , \quad G = \frac{1}{g_0 R_0} = \frac{1}{R_0} \quad (3.6)$$

while for inductances

$$L = \left( \frac{R_0}{g_0} \right) \left( \frac{\omega_1}{\omega} \right) L_n = \frac{R_0}{\omega} g_n \quad (3.7)$$

and finally, for capacitances the formula is given as

$$C = \left( \frac{g_0}{R_0} \right) \left( \frac{\omega}{\omega_1} \right) C_n = \frac{\omega}{R_0} g_n. \quad (3.8)$$

In (3.7) and (3.8), the parameters  $L_n$ ,  $C_n$  represent the normalized values obtained from the above tables for the  $n^{th}$  network element.

## 3.2. Transformations with Lumped Components

The methodology presented in the previous section is a synthesis method which can be used as a basis for designing other type of filters as well. The topology in Fig. 3.1 can be adapted by appropriate transformations resulting in a bandpass or bandstop filter, according to Fig. 3.3. An example of a bandpass filter topology with passband corner frequencies  $\omega_1$  and  $\omega_2$ , is depicted in Fig. 3.4.

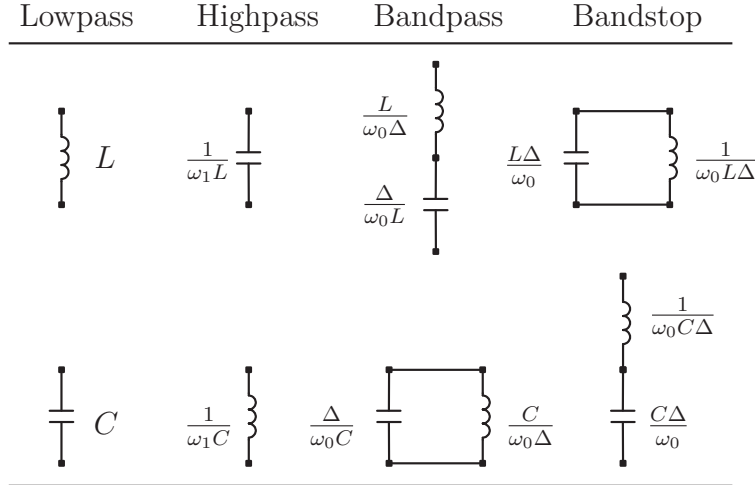


Figure 3.3.: Prototype Filter Transformations.

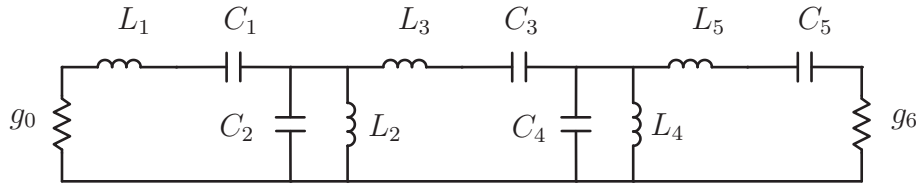


Figure 3.4.: General 5<sup>th</sup> order bandpass filter prototype.

As it is readily seen, the series inductive branches from Fig. 3.1 have been replaced by series  $LC$  resonators while the shunt capacitive branches are replaced by parallel  $LC$  resonators. For the shunt resonators, the reactive elements can be calculated according to the expression

$$Y_i = \omega_0 C_i = \frac{1}{\omega_0 L_i} = \frac{g_i}{\Delta}, \quad \text{for } i = 2, 4 \quad (3.9)$$

while for the series resonators the reactance is given as

$$Z_j = \omega_0 L_j = \frac{1}{\omega_0 C_j} = \frac{g_j}{\Delta}, \quad \text{for } j = 1, 3, 5. \quad (3.10)$$

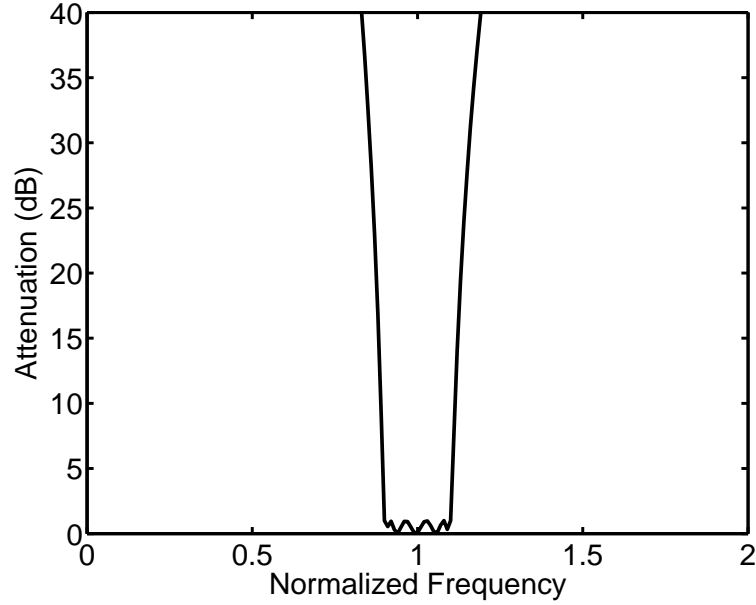


Figure 3.5.: Calculated attenuation profile for Chebyshev bandpass filter with fractional bandwidth  $\Delta=0.2$ , filter order  $n=5$ , and passband attenuation  $A_r=1$  dB.

In (3.9) and (3.10),  $\omega_0=\sqrt{\omega_1\omega_2}$  is the center passband frequency,  $\Delta=(\omega_2 - \omega_1)/\omega_0$  the fractional bandwidth, and  $g_i, g_j$  the filter prototype coefficients of the lowpass prototype. Substituting the normalized frequency  $\omega/\omega_1$ , in (3.4), with the following expression

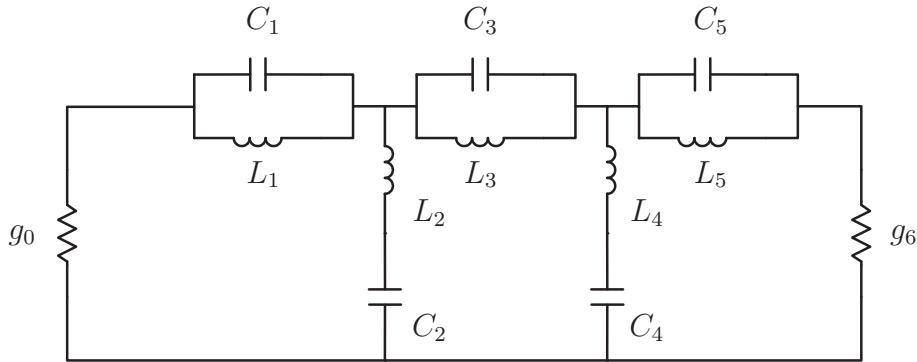
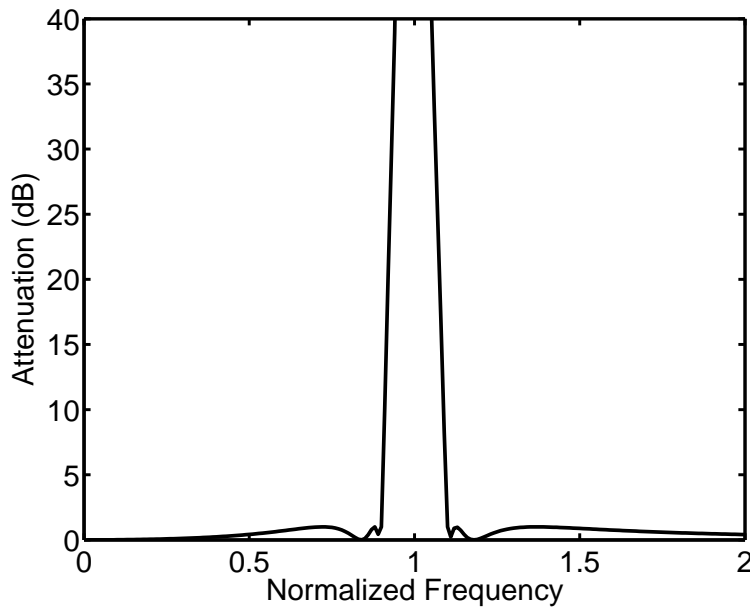
$$\frac{\omega}{\omega_1} = \frac{1}{\Delta} \left( \frac{\omega}{\omega_0} - \frac{\omega_0}{\omega} \right), \quad (3.11)$$

results in a response as indicated in Fig. 3.5. Selecting the appropriate parameters for the center frequency, fractional bandwidth, attenuation level, and filter order allows for designs of a filter with total control of its response.

The same methodology is applicable to a bandstop filter, which has the general form of Fig. 3.6. The reactance parameters of the series and shunt branches can be calculated, as in the case of the bandpass filter, from (3.9) and (3.10). Calculating the attenuation profile of the resulting bandstop filter is achieved by substituting the normalized inverse frequency  $\omega_1/\omega$ , in (3.4), with the following expression

$$\frac{\omega_1}{\omega} = \frac{1}{\Delta} \left( \frac{\omega}{\omega_0} - \frac{\omega_0}{\omega} \right). \quad (3.12)$$

This type of bandstop filter would exhibit an attenuation profile as in Fig. 3.7. In the same way as for the previously discussed bandpass filter, this design methodology results in filter circuits with predictable responses.

Figure 3.6.: General 5<sup>th</sup> order bandstop filter prototype.Figure 3.7.: Calculated attenuation profile for Chebyshev bandstop filter with fractional bandwidth  $\Delta=0.2$ , filter order  $n=5$ , and passband attenuation  $A_r=1$  dB.

As can be seen by the discussed prototype filters they have some common structures, namely resonators either as series or shunt LC branches as indicated in Fig. 3.8. The resonance frequency of such structures can be expressed directly as  $f = 1/(2\pi\sqrt{LC})$ . By introducing a tunable capacitive element, like the ones discussed in Chapter 2, a tuning functionality is achieved. Changing the capacitance  $C$  results in shifting the resonance frequency  $f$ . Assuming a tunability, defined as  $(C_{max} - C_{min})/C_{max}$ , of 60% which is typical for the used ferroelectric varactors

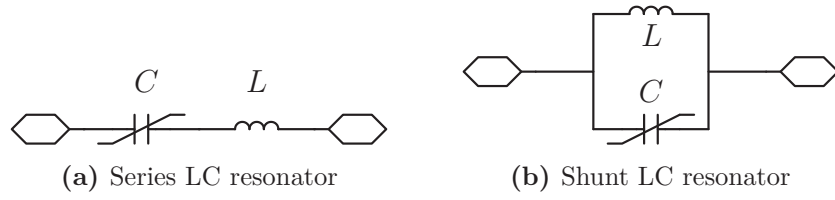


Figure 3.8.: Lumped element resonators with tunable capacitances; a) Series LC branch and b) Shunt LC branch.

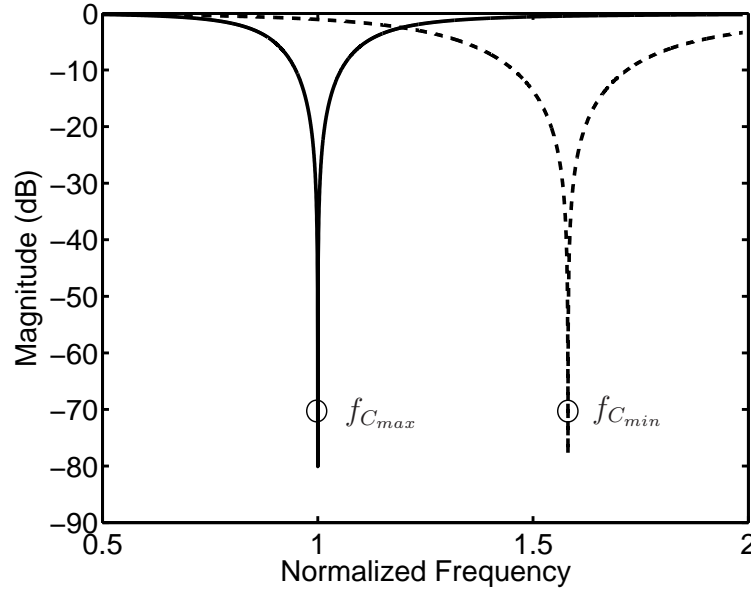


Figure 3.9.: Calculated transmission S-parameter  $S_{21}$  of shunt type LC resonator for two discrete capacitance values with assumed tunability of 60%.

would result in a frequency ratio of

$$\frac{f_{C_{min}}}{f_{C_{max}}} = \sqrt{\frac{C_{max}}{C_{min}}} = \sqrt{\frac{C_{max}}{0.4C_{max}}} = \sqrt{\frac{1}{0.4}} \approx 1.6. \quad (3.13)$$

The calculated transmission response of a shunt type resonator for two discrete capacitance values is depicted in Fig. 3.9. Combining several of those tunable resonator segments would result in bandpass or bandstop filters with tunable characteristics.

### 3.3. Transformations with Distributed Components

Lumped element filters, as they have been discussed in the previous section, perform well at lower frequencies. However as frequencies move into the microwave range

constraints arise since the lumped components can not be realized anymore. Main reasons are due to self resonance effects of lumped components and the low quality factors. As an example, the reflection coefficient of commercially available surface mount devices (SMD) is plotted over frequency in Fig. 3.10. As can be seen, both type of elements exhibit a resonance for higher frequencies, which is noticed by a change in the reactance. Considering the Smith chart representation of the reflection coefficient, it is visible that the reactance changes its behavior at the point of the self resonance frequency. An initially inductive element becomes capacitive and vice versa. The allocation of the resonance frequency depends on the intrinsic reactance and the component dimensions which determine the parasitic effects.

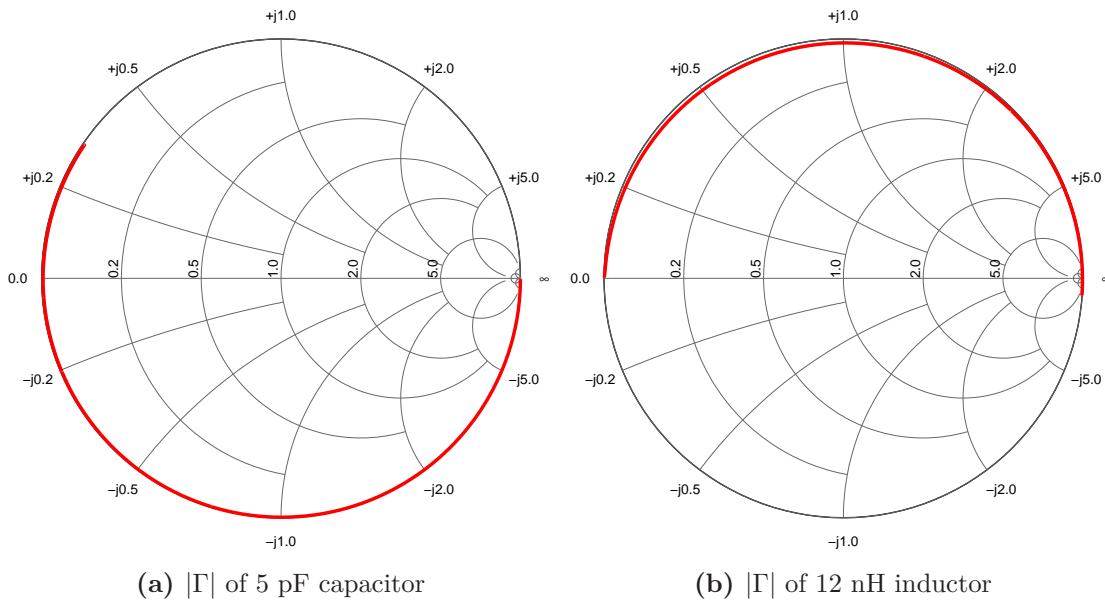


Figure 3.10.: Input reflection coefficient  $|\Gamma|$  of SMD type components for a frequency range up to 7 GHz; a) Murata GJM 0201-series 5 pF capacitor and b) Murata LQW 0402-series 12 nH inductor.

As a result, the quality factor near the resonance frequency drops dramatically while the inductive and capacitive impedances reach their maximum respectively minimum value. In other words, the implementation of microwave circuits at higher frequencies becomes impractical with lumped components since their performance degrades noticeably. As an alternative, lumped components can be substituted by their equivalent transmission line segments using the Richards transformation [89]. The transformation uses following expression

$$\Omega = \tan(\beta l) = \tan\left(\frac{\omega l}{u_p}\right), \quad (3.14)$$



where  $\Omega$  is an auxiliary frequency plane which repeats with a period of  $\omega l/u_p=2\pi$ . Using the mapping technique of (3.14) yields the equivalent transmission line structures, which are presented in Fig. 3.11. The reactance of an inductor can be written as

$$jX_L = j\Omega L = jL \tan(\beta l), \quad (3.15)$$

while the susceptance of a capacitor can be expressed as

$$jB_C = j\Omega C = jC \tan(\beta l). \quad (3.16)$$

The results from (3.15) and (3.16) indicate that an inductor can be replaced by a short circuited stub of characteristic impedance  $L$ , while a capacitor can be replaced by an open circuited stub of characteristic impedance  $1/C$ . Both transmission line segments have an electrical length of  $\beta l$ . All values for  $L$  and  $C$  refer to the prototype element values of the previous sections. As discussed for the general lowpass structure in Section 3.1, the normalized cut-off frequency was set to 1. In order to obtain the same normalized frequency, the Richards transformation leads to the condition

$$\Omega = \tan(\beta l) = 1, \quad (3.17)$$

which results in a stub length of  $l = \lambda/8$ , as indicated in Fig. 3.11.

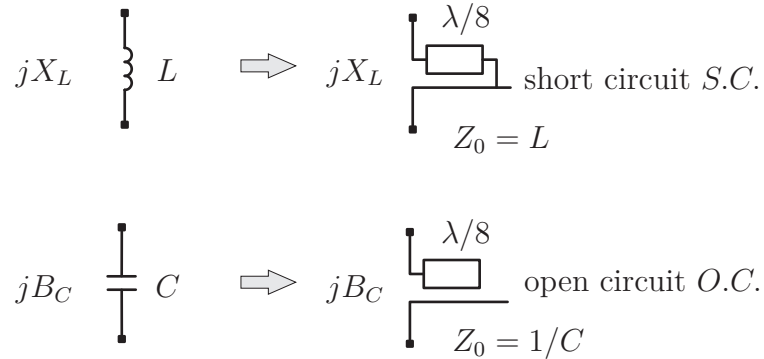


Figure 3.11.: Richards's transformations for lumped components.

Applying the aforementioned transformations to the 5<sup>th</sup> order lowpass filter of Fig. 3.1, results in a topology with distributed elements as depicted in Fig. 3.12. A comparison between the lowpass response for a lumped element and distributed filter, with the same cut-off frequency, is presented in Fig. 3.13. It is readily seen, that although both filters have almost identical network zeros, thus an equivalent passband performance, they have different performance in the stopband region. The distributed filter exhibits a much steeper pass- to stopband transition, leading to higher stopband rejection. At the same time, the periodicity of the transmission

line segments is resulting in a second passband region which occurs at the third harmonic of the cut-off frequency. Additional parameters which have to be taken into account are the overall circuit dimensions. Lumped element filters consisting of SMD type components can be designed to be very compact. Equivalent filters with distributed components have much larger dimensions since each transmission line segment has an electrical length of approximately  $\lambda/8$ .

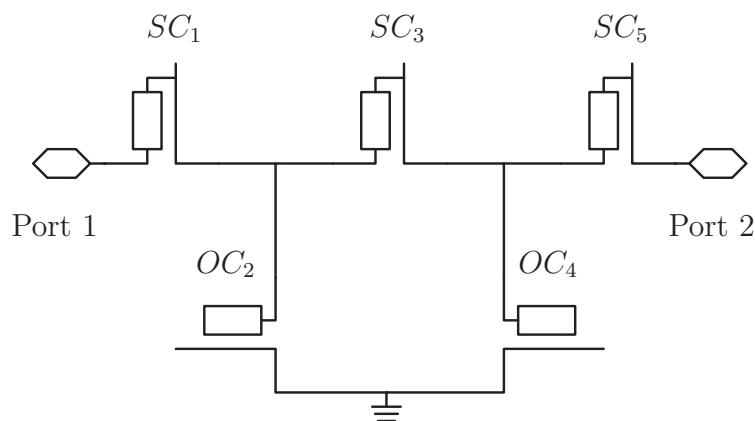


Figure 3.12.: 5<sup>th</sup> order lowpass filter with distributed elements.

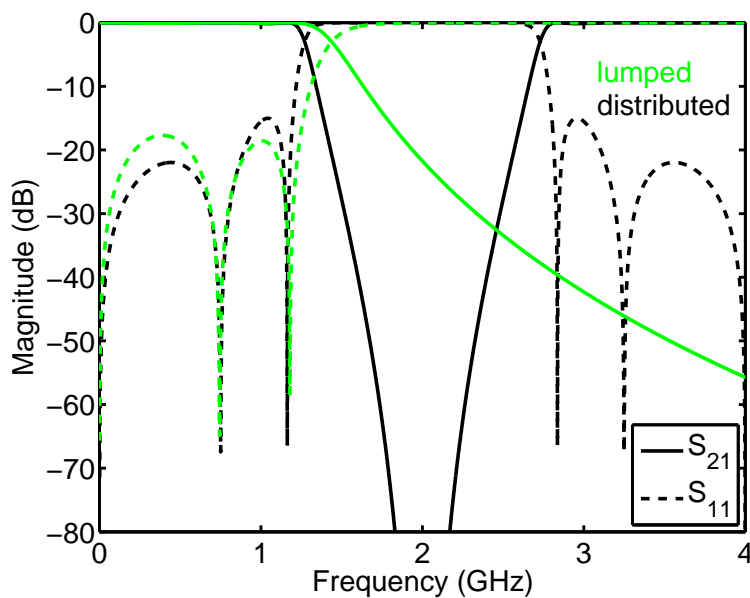


Figure 3.13.: Calculated response for equivalent 5<sup>th</sup> order lowpass filters with lumped and distributed components.

Whether the implementation is realized with lumped or distributed components,

finally is a question of the target application. For higher frequencies, where lumped components are impractical or degrade quickly, the distributed element approach is advantageously. On the other hand, for low frequencies lumped element implementations seem to be the better choice. A further important issue concerning filter design for microwave communication systems is the power handling capability of such circuits. When considering operation in high power systems, such as base station architectures, filter topologies based on waveguides appear to be the most suitable ones. High power handling capabilities and resonator quality factors with an order of magnitude of  $10^4$  lead to unsurpassed performance. The overall bulky dimensions and increased weight of such filter structures have to be considered as drawbacks. Nowadays, tuning of base station multiplexers or bandpass filters is achieved by using stubs which are inserted in waveguide resonator branches and are controlled by step motors. Alternatively, tunable elements such as the previously discussed ferroelectric- or MEMS-varactors could be used, leading to much higher integration levels.

In the following sections some filter topologies will be proposed, which are based on tunable passive elements. The main objective of these sections is to provide detailed design procedures, which lead to predictable network performances. By introducing the tunable elements an additional functionality is inserted, namely tunable or reconfigurable characteristics. The proposed filter networks of the following sections will be later on presented as prototype boards. The implementation of these circuits and their RF performance will be discussed in a separate chapter.

### 3.4. Lowpass Filter

Lowpass filters in various implementations are used in a large number of applications. Especially in transceiver architectures they can be used as output stages of power amplifiers. Their main objective is to allow for good transmission within their passband and attenuate the harmonic frequencies which may occur in the transmitter. The schematic of a tunable 5<sup>th</sup> order Chebyshev lowpass filter is shown in Fig. 3.14, where the initial capacitors were substituted by BST varactors. The

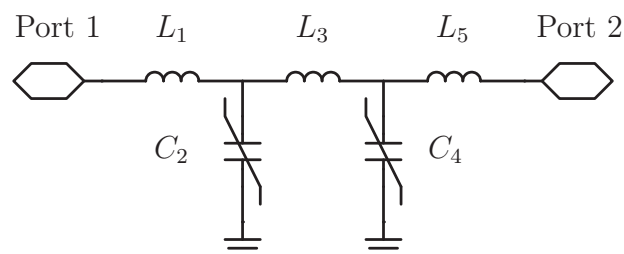


Figure 3.14.: Tunable 5<sup>th</sup> order lowpass filter with  $L_1=L_5 \neq L_3$  and  $C_2=C_4=C$ .

values for the reactive elements can be derived, e.g. from table (3.1), depending on the target filter performance as discussed in the previous sections. By scaling these prototype values for the system impedance  $Z_0$  and operating frequency  $\omega$  the final reactive element values are obtained. In a first approximation additional biasing components such as DC-block capacitors and RF-choke inductors, as they are typically needed in order to establish the proper biasing conditions for the ferroelectric varactors, will be neglected. Their contribution and use in the circuit will be addressed later on when the prototype boards and their fabrication is discussed. Computing the network  $ABCD$  parameters, as described in Appendix A, results in simply multiplying the chain matrices for all series and shunt branches.

$$M_{i=1,3,5} = \begin{bmatrix} A & B \\ C & D \end{bmatrix} = \begin{bmatrix} 1 & Z_i \\ 0 & 1 \end{bmatrix} \quad (3.18)$$

$$M_{j=2,4} = \begin{bmatrix} A & B \\ C & D \end{bmatrix} = \begin{bmatrix} 1 & 0 \\ Y_j & 1 \end{bmatrix} \quad (3.19)$$

All series branches with inductive elements of impedance  $Z_i=pL_i$  can be represented with the chain matrix in (3.18). Respectively, all shunt branches with capacitive elements of admittance  $Y_j=pC_j$  can be described with the chain matrix in (3.19). In both cases,  $p=j\omega$  is the complex angular frequency. The resulting  $ABCD$  matrix  $M_{total}=M_1 \cdot M_2 \cdot M_3 \cdot M_4 \cdot M_5$  is used to calculate analytically the transmission and reflection scattering parameters of the network. For port impedances of  $Z_0$ , the ratio between reflection and transmission S-parameters is given as

$$\begin{aligned} \frac{S_{11}(p)}{S_{21}(p)} &= \frac{1}{2Z_0} p^5 L_1^2 L_3 C^2 + \\ & p^3 \left( \frac{1}{Z_0} L_1^2 C + \frac{1}{Z_0} L_1 L_3 C - \frac{Z_0}{2} L_3 C^2 \right) + \\ & p \left( -Z_0 C + \frac{1}{2Z_0} L_3 + \frac{1}{Z_0} L_1 \right). \end{aligned} \quad (3.20)$$

The resulting conjugate complex zeros, which are the roots of the polynomial, are located at  $z_1=0$  and

$$z_2 = j\omega_2 = \pm \frac{\sqrt{2CL_3(-2L_1L_3 - 2L_1^2 + Z_0^2CL_3 + \alpha)}}{2CL_1L_3} \quad (3.21)$$

$$z_3 = j\omega_3 = \pm \frac{\sqrt{2CL_3(-2L_1L_3 - 2L_1^2 + Z_0^2CL_3 - \alpha)}}{2CL_1L_3} \quad (3.22)$$

with the constant  $\alpha$  given as

$$\alpha = \sqrt{-4L_1L_3^2Z_0^2C + 4L_1^4 + 4L_1^2L_3Z_0^2C + L_3^2Z_0^4C^2}. \quad (3.23)$$

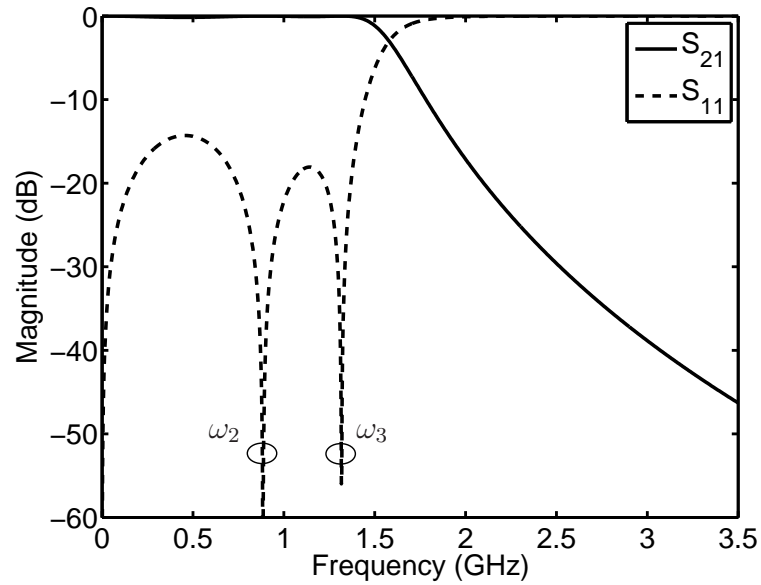


Figure 3.15.: Calculated S-parameters for an ideal 5<sup>th</sup> order lowpass filter with  $C=3$  pF,  $L_1=L_5=6.8$  nH, and  $L_3=12$  nH.

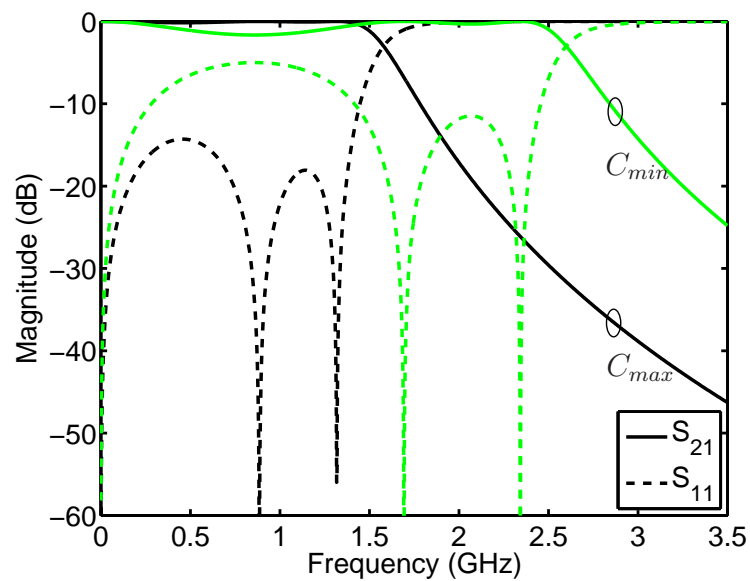


Figure 3.16.: Calculated S-parameters for an ideal 5<sup>th</sup> order lowpass filter with  $L_1=L_5=6.8$  nH,  $L_3=12$  nH, and two discrete capacitance values with a ratio of  $(C_{max} - C_{min})/C_{max}=0.4$ .

These three discrete frequency points, where the reflection tends toward zero, are readily seen in the calculated response of an ideal filter in Fig. 3.15. The frequency response of the filter can be altered by changing the capacitance value  $C$  and thus shifting the network zero locations. An example for the achievable tuning range, assuming a tunability of 60 % for the BST varactors, is demonstrated in Fig. 3.16. For real implementations a performance degradation is expected, since the calculations apply for lossless elements and ignore additional biasing components. Nevertheless, the potential of implementing a frequency agile filter is clearly demonstrated. Such filters can be used in multi-band transceivers of mobile radios in order to serve as an output filter for the power amplifier. Each supported frequency band could be covered separately since the BST varactors allow for a continuous tuning. Each bias setting would result in a different operating frequency.

### 3.5. Notch Filter

Bandstop or notch filter topologies can be derived from the discussed lowpass prototypes by a simple substitution of the shunt capacitive branches with series  $LC$  resonators. The series inductive branches are then substituted by parallel  $LC$  resonators. A second order tunable bandstop filter is depicted in Fig. 3.17. Two cascaded capacitors are used, instead of a single one, in order to simplify the bias supply and avoid additional DC-block capacitors.

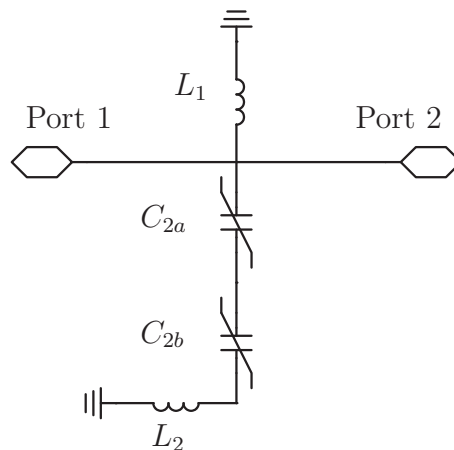


Figure 3.17.: Tunable bandstop filter with cascaded BST varactors  $C_{2a}=C_{2b}=C$ .

Applying the same principle as before, the transfer function of the network can

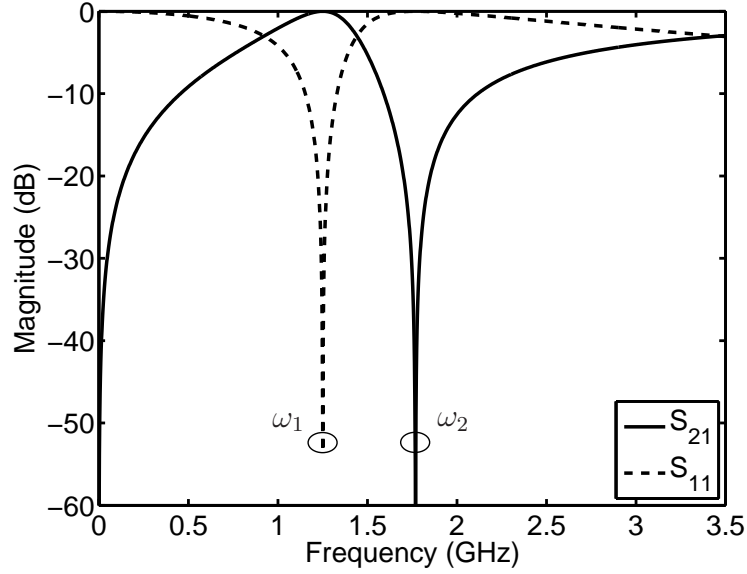


Figure 3.18.: Calculated S-parameters for an ideal notch filter with  $C=6$  pF and  $L_1=L_2=2.7$  nH.

be computed by multiplying the individual  $ABCD$  matrices.

$$M_1 = \begin{bmatrix} A & B \\ C & D \end{bmatrix} = \begin{bmatrix} 1 & 0 \\ Y_1 & 1 \end{bmatrix} \quad (3.24)$$

$$M_2 = \begin{bmatrix} A & B \\ C & D \end{bmatrix} = \begin{bmatrix} 1 & 0 \\ Y_2 & 1 \end{bmatrix} \quad (3.25)$$

The overall network transfer function is  $M_{total}=M_1 \cdot M_2$ . In (3.24) the shunt admittance in the first branch is  $Y_1=1/(pL_1)$  whereas in (3.25) the admittance of the second branch is calculated, from the series combination of the inductor and the two cascaded capacitors, as  $Y_2=1/[2/(pC) + pL_2]$ . The analytical expressions for the reflection and transmission S-parameters can be calculated from the overall  $ABCD$  matrix of the network. For port impedances of  $Z_0$ , the ratio between them is then given as

$$\frac{S_{11}(p)}{S_{21}(p)} = -\frac{Z_0}{2} \cdot \frac{2 + p^2C(L_1 + L_2)}{pL_1(2 + p^2L_2C)}. \quad (3.26)$$

Network parameters such as poles and zeros are readily extracted from (3.26). The conjugate complex network zeros, which are the roots of the numerator, are located at

$$z_1 = j\omega_1 = \pm\sqrt{-2/[(L_1 + L_2)C]}. \quad (3.27)$$

The corresponding conjugate complex poles, which are roots of the denominator,

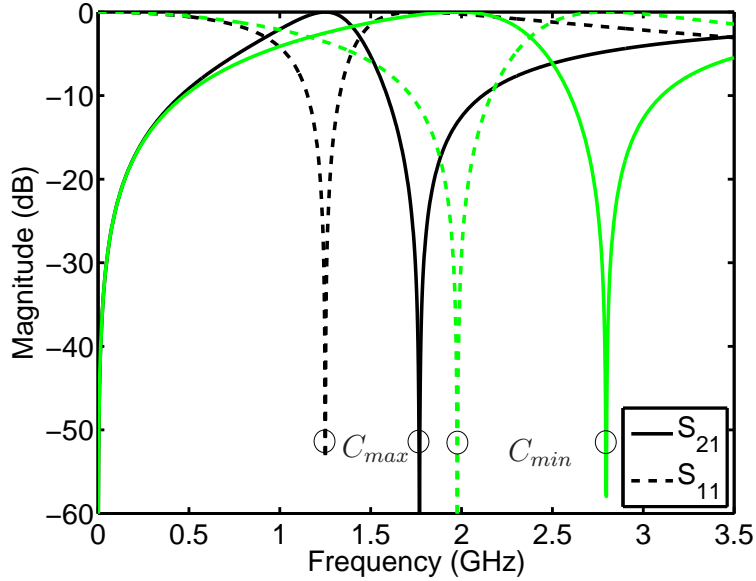


Figure 3.19.: Calculated S-parameters for an ideal notch filter with  $L_1=L_2=2.7$  nH and two discrete capacitance values with a ratio of  $(C_{max} - C_{min})/C_{max}=0.4$ .

are located at  $p_1=0$  and

$$p_2 = j\omega_2 = \pm\sqrt{-2/(L_2C)}. \quad (3.28)$$

Changing the capacitance value  $C$  results in shifting the zero and pole frequency and thus the pass- and stopband allocation respectively, as illustrated in Figs. 3.18 and 3.19. As it is readily seen from Fig. 3.19, this notch filter is suitable for multi-band operation since it covers the most relevant frequency bands from 1.7 GHz to 2.7 GHz. Shifting the notch frequency could be used in order to suppress crosstalk effects within the receiver or to block strong interfering signals. These unwanted scenarios reduce the sensitivity of the receiver and thus the overall radio front-end efficiency. Again, a real implementation with lumped finite- $Q$  elements would result in performance degradation. This type of filter, in combination with the previously described lowpass filter which exhibits a comparable tuning range, could be used in front-end architectures in order to ensure a band selective and reconfigurable operation.

### 3.6. Bandpass Filter

Bandpass filters represent probably the most significant filter group since they are used in the majority of communication systems. In front-end architectures,



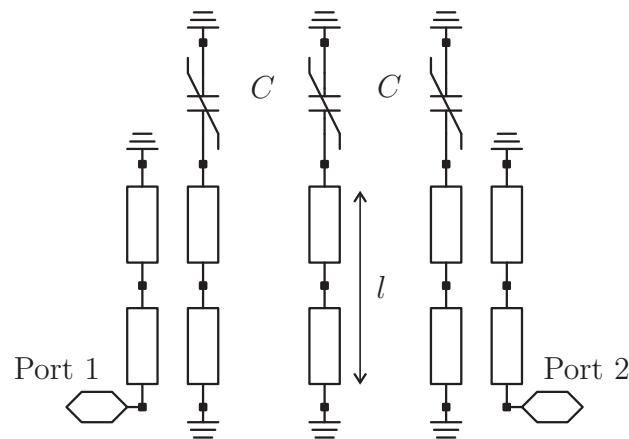


Figure 3.20.: Comblines bandpass filter topology.

whether for mobile or base station devices, bandpass filters are the first filter stage and usually they are located right after the antenna port. Among the possible candidates for distributed filters with relative narrow passbands the combline type filter [88] is a very popular one and is the topology of choice for this work. The operating principle is based on loading coupled transmission line resonators with capacitive elements and thus reducing the electrical length of the resonator. A detailed description of the tuning mechanism of such filters is given in [90]. An example of a combline filter topology is presented in Fig. 3.20. The resonators consist of microstrip line segments, which are short circuited at the lower end and terminated at the other end with lumped capacitive elements. Using this type of resonator loading allows for implementations of resonator branches which are shorter than the conventional quarter wavelength segments. For the three stage filter in Fig. 3.20 the loading elements are represented by the capacitances  $C$ . The additional input and output segments serve for impedance matching and do not insert additional resonances. Alternatively, tapped input and output resonator stages can be used as will be discussed later on.

The coupling between the individual resonator branches is achieved by the fringing fields between the resonator lines, thus it is predominantly of magnetic nature. As a consequence, tight resonator coupling results in narrow spaced resonator segments. By terminating the resonators with the lumped capacitances, their electrical length is made significantly shorter than  $\lambda/4$  at the midband frequency. This bandpass filter topology can be implemented in a very compact manner since the electrical lengths of the resonators are much shorter than in other types of coupled resonator filters. An additional argument which favors the combline filter is the fact that it implies inherently capacitive elements as resonator loads. Thus it became attractive to use tunable capacitors in order to alter the resonance behavior of those branches. The actual combline filter exhibits attenuation poles at  $\omega_1=0$

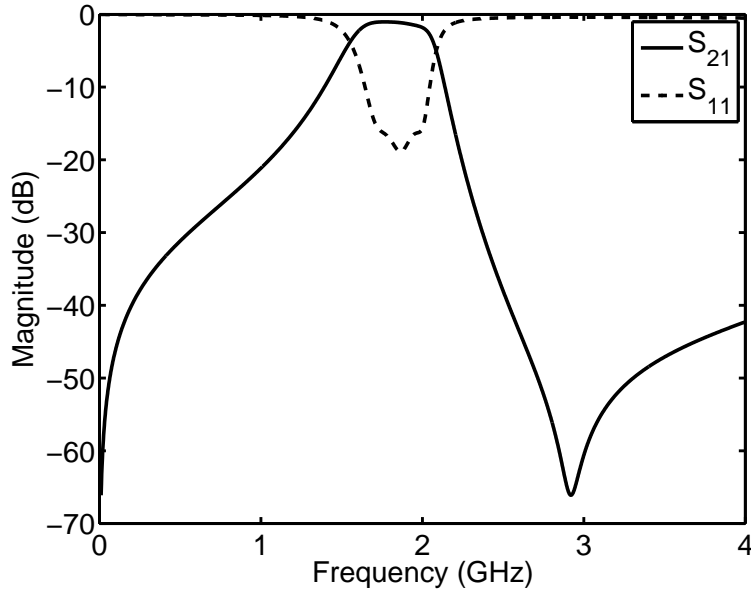


Figure 3.21.: Calculated S-parameters for a 3-stage combline filter with a center frequency of 1.9 GHz and a fractional bandwidth of  $\Delta=0.1$ .

and  $\omega_2=\omega_0\lambda_0/(4l)$ , where  $\omega_0$  is the passband center frequency,  $\lambda_0$  the wavelength at this point, and  $l$  the total resonator length. The asymmetric pole allocation leads to a slow pass- to stopband transition in the lower stopband and a broad upper stopband. A typical combline filter response is depicted in Fig. 3.21.

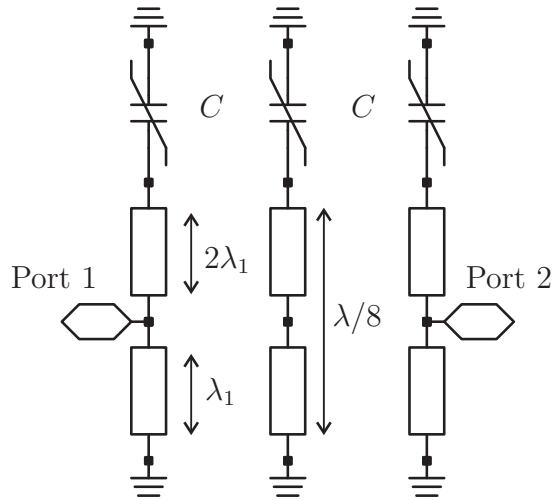


Figure 3.22.: Combline bandpass filter topology with tapped input and output segments.

Alternatively to the topology presented in Fig. 3.20, the combline filter can be

designed with tapped input and output line segments obtaining the filter structure of Fig. 3.22. This modified structure can be designed analytically according to [91], [92] and has the advantage of even more compact overall dimensions. An equivalent circuit representation of the combline filter with tapped input and output segments is given in Fig. 3.23. For this equivalent structure the three resonator branches with length of approximately  $\lambda/8$  are represented by shunt branches of admittance  $Y_i$  where  $i=1,2,3$ . The coupling between them is established by two line segments of the same electrical length  $\lambda/8$  with admittances of  $Y_{12}, Y_{23}$  respectively. The tapped input and output segments are represented by an L shaped segment with two transmission lines of admittance  $Y_t$  and electrical lengths of  $\lambda_1, 2\lambda_1$ . Based on this equivalent circuit the following set of equations is used to calculate the network parameters.

$$Y_t = Y_{11} - \frac{Y_{12}^2}{Y_{22}} \quad (3.29)$$

$$Y_1 = \frac{Y_{12}}{Y_{22}}(Y_{12} - Y_{22}) \quad (3.30)$$

$$Y_2 = Y_{22} - Y_{12} - Y_{23} \quad (3.31)$$

$$Y_3 = Y_{33} - Y_{23} \quad (3.32)$$

For the above set of equations,  $Y_{11}, Y_{22}, Y_{33}$  are the admittances of the individual resonator lines while the coupling parameters  $Y_{12}$  and  $Y_{23}$  can be calculated according to following expressions

$$Y_{i,i+1|i=1,N-1} = \frac{\Delta b}{\sqrt{g_i g_{i+1}}} \tan(\theta_0) \quad (3.33)$$

$$b = \frac{Y_a}{2} \left[ \frac{\theta_0}{\sin^2(\theta_0)} + \cot(\theta_0) \right], \quad (3.34)$$

where  $\theta_0, Y_a, \Delta, N$  are the electrical lengths at the midband frequency, admittance, fractional bandwidth, and the filter order, respectively. The values of  $g_i$  correspond to the element values of the lowpass filter prototype which is discussed in Section 3.1. Regardless of which configuration is finally chosen the tuning mechanism, namely capacitive loading of a resonator, remains the same. This tuning principle is illustrated in Fig. 3.24. Assuming an arbitrary transmission line segment of characteristic impedance  $Z_0$  and electrical length  $\theta$  which is loaded by a lumped element with complex impedance  $Z_L=1/(j\omega C)$ , results in an input impedance of the following form

$$Z_{in} = Z_0 \frac{Z_L + jZ_0 \tan(\theta)}{Z_0 + jZ_L \tan(\theta)}. \quad (3.35)$$

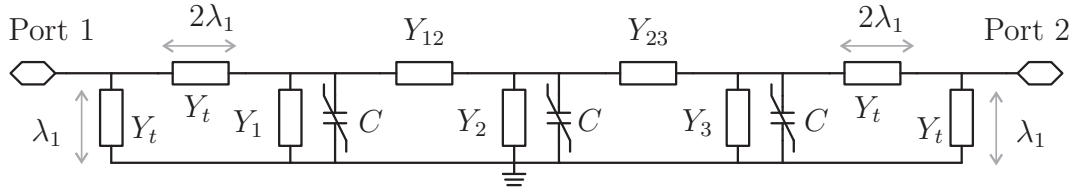


Figure 3.23.: Equivalent circuit of combline bandpass filter with tapped input and output segments.

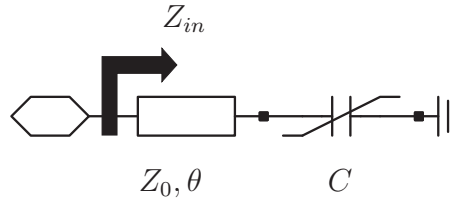


Figure 3.24.: Transmission line segment of arbitrary characteristic impedance  $Z_0$  and electrical length  $\theta$  loaded with a lumped capacitance  $C$ .

Substituting the expression for  $Z_L$  in (3.35) results in

$$Z_{in} = Z_0 \frac{\frac{1}{j\omega C} + jZ_0 \tan(\theta)}{Z_0 + j\frac{1}{\omega C} \tan(\theta)} = Z_0 \frac{-j(\frac{1}{\omega C} - Z_0 \tan(\theta))}{Z_0 + \frac{1}{\omega C} \tan(\theta)}. \quad (3.36)$$

The cascaded connection of the two elements is expected to give an impedance of  $Z_{in}=0$  at the resonance frequency, thus solving (3.36) results in a resonance frequency of

$$f = \frac{1}{2\pi C Z_0 \tan(\theta)}. \quad (3.37)$$

It is readily seen from (3.37) that a change in the capacitance  $C$  would result in an immediate shift of the resonance frequency. Exactly this mechanism forms the basis of designing tunable combline filter structures. Criteria for selection of the appropriate electrical lengths for the resonators and tuning capacitances are given in [93]. As mentioned before, the combline filter exhibits a transmission response which is not symmetrical around its passband. This behavior can be readily seen by the data presented in Fig. 3.21. The allocation of the attenuation poles leads to a slow pass- to stopband transition in the lower stopband and a much broader upper stopband. In order to achieve a symmetric response around the passband a modified filter version can be used, which is depicted in Fig. 3.25.

Compared to the previously discussed filter this topology includes a second capacitor  $C_p$ , which is added to the lower resonator end. By using this capacitive loading an attenuation pole is added at the lower stopband. This principle is reported in [94] and has been implemented in a similar way in [95]. As presented

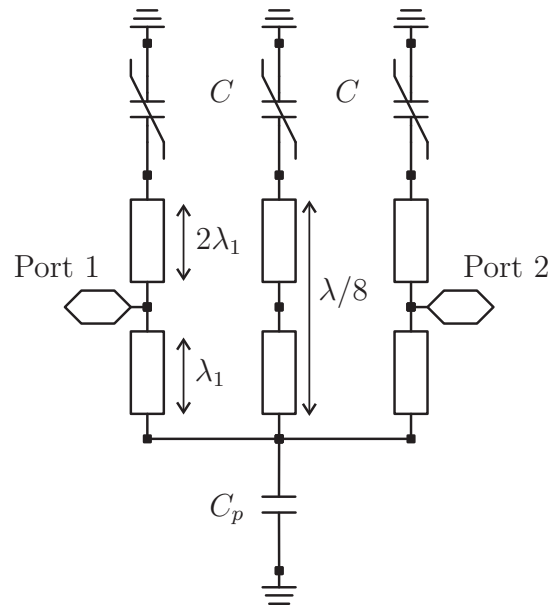


Figure 3.25.: Modified combline bandpass filter.

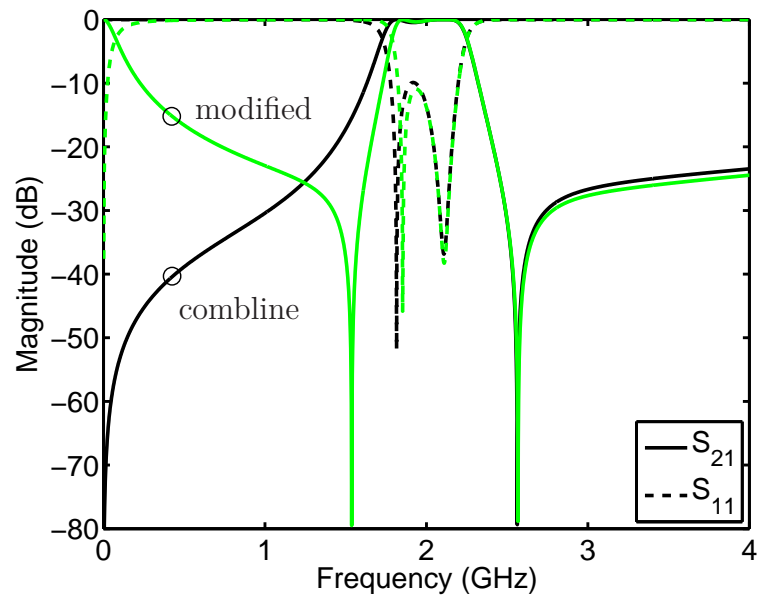


Figure 3.26.: Calculated S-parameters for original combline filter and the modified version of Fig. 3.25.

in Fig. 3.26 the insertion of an attenuation pole in the lower stopband results in a much higher selectivity in the transition between pass- and stopband while the passband response is retained. Appropriate dimensioning of the capacitance  $C_p$  and

thus the allocation of the attenuation pole can be used as an additional optimizing parameter. Furthermore, choosing a tunable capacitance at this point instead of a constant value one would yield tunable bandpass filters with not only reconfigurable center frequencies but further tunable stopband characteristics. This is an attractive feature for reconfigurable front-end architectures, since future communication standards, like 4G LTE (Long Term Evolution), will support variable channel bandwidths. The frequency range, which could be covered by a tunable bandpass filter by using ferroelectric varactors with a tunability of 60% is demonstrated in Fig. 3.27.

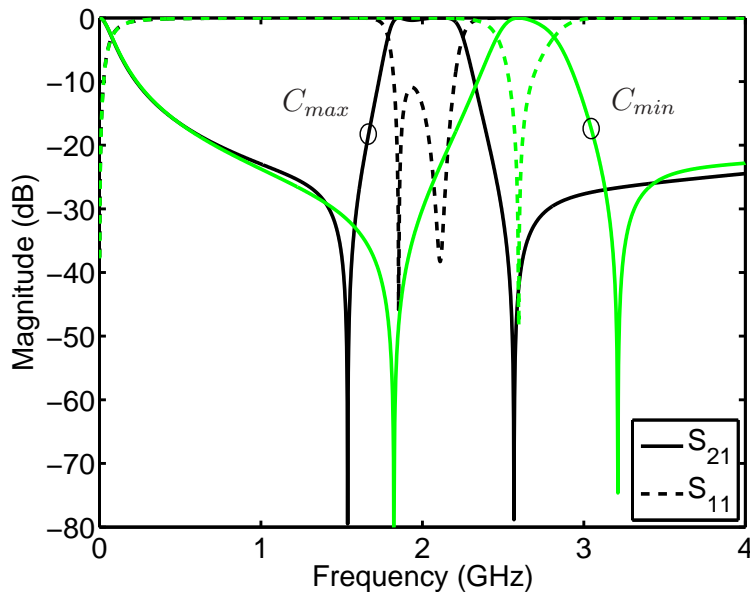


Figure 3.27.: Calculated S-parameters of the proposed tunable combline filter for two discrete capacitance values with a ratio of  $(C_{max} - C_{min})/C_{max}=0.4$ .

Some interesting issues should be noticed by observing the response of the filter. Altering the loading capacitance for the resonators causes a change in the resonance behavior thus for the value of  $C_{min}$  the coupling of the resonators is disturbed in a way that the filter appears to have a single pole. A second fact which is important for the filter performance is the allocation of the attenuation pole in the lower stopband. As opposed to the attenuation pole in the upper stopband, which is inherently present, the attenuation pole in the lower stopband is not shifted by the same amount as the passband center frequency. This is due to the fact that the lower attenuation pole is determined mainly by the fixed capacitor  $C_p$ . As a consequence the passband bandwidth is altered as well.

## 4. Frequency Agile Power Dividers and Couplers

The focus in this chapter lies on the principles of microwave power dividers and couplers which are based on transmission line segments. Such microwave circuits have been used in various applications such as Doherty amplifiers, balanced amplifiers, and balanced mixers. Tight coupling structures, like 3 dB-couplers, can be hardly implemented with planar coupled lines due to the impractical very narrow spacing between the line segments. Thus other topologies like Wilkinson power dividers and branch-line couplers have to be used. These topologies will be subject of investigation in this chapter. The potential of achieving a frequency agile behavior based on tunable passive elements will also be discussed. By introducing the tunable passive elements a novel methodology of designing reduced size frequency agile circuits is obtained for this type of circuits.

### 4.1. Wilkinson Power Divider

A power divider topology which was presented for the first time by Wilkinson in [96] and is since then known simply as the Wilkinson divider is presented in Fig. 4.1.

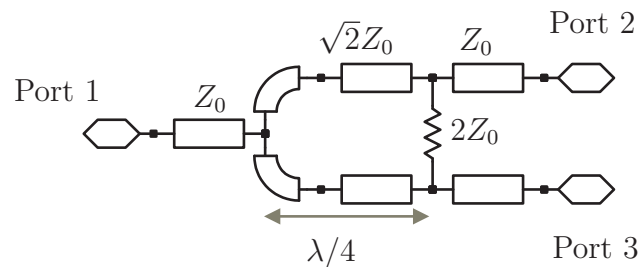


Figure 4.1.: Wilkinson power divider.

As opposed to other power divider structures, such as T-splitters or resistive dividers, the Wilkinson divider allows for matching at all ports while achieving perfect isolation between the outputs at the resonance frequency. The input and output port impedances are  $Z_0$  while the  $\lambda/4$  segments have a characteristic impedance of  $\sqrt{2}Z_0$ . The output ports 2 and 3 are connected through a resistor with  $R=2Z_0$  thus enabling impedance matching at all ports and isolation between them at the  $\lambda/4$

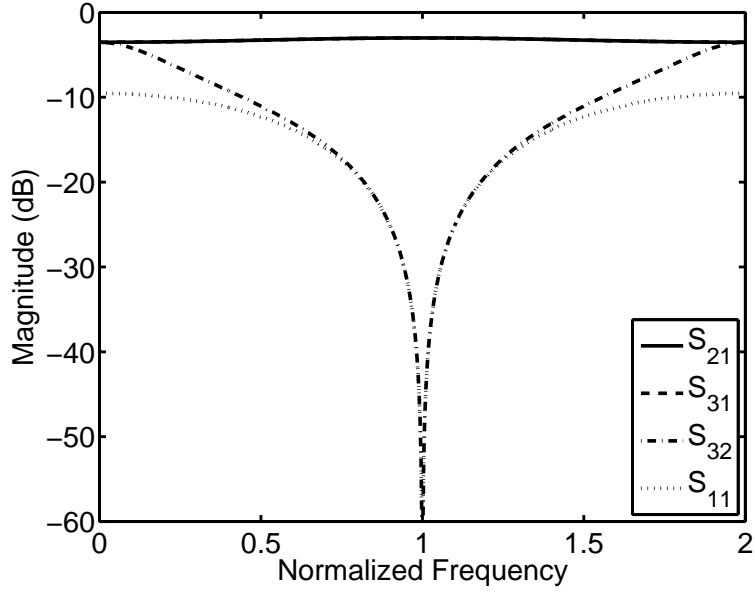


Figure 4.2.: Calculated S-parameters for an ideal Wilkinson divider network.

resonance frequency. Symmetric power splitting is achieved with no phase difference,  $\Delta\phi=0$ , for the two transmission paths. Although the Wilkinson divider can also be designed for an arbitrary power division, we will consider only the equal split 3 dB case in this work. Following the detailed analysis given in [97], based on even and odd mode excitations, the Wilkinson divider can be summarized by a  $3\times 3$  scattering matrix of the following form

$$[S] = \begin{bmatrix} S_{11} & S_{12} & S_{13} \\ S_{21} & S_{22} & S_{23} \\ S_{31} & S_{32} & S_{33} \end{bmatrix} = \begin{bmatrix} 0 & -j/\sqrt{2} & -j/\sqrt{2} \\ -j/\sqrt{2} & 0 & 0 \\ -j/\sqrt{2} & 0 & 0 \end{bmatrix}. \quad (4.1)$$

The calculated performance of an ideal network according to (4.1) is depicted in Fig. 4.2. As expected for a quarter-wavelength based structure the useful bandwidth of operation is somehow limited due to the narrowband resonance. In practical implementations, where finite quality factors impose more limitations a bandwidth of less than 10% around the resonance frequency should be considered realistic. An increased operational bandwidth is achievable by a multi-sectional design, which obviously leads to larger circuit dimensions. Although the transmission line segments can be implemented in various ways we will focus on microstrip line based implementations.



## 4.2. Branch-Line Coupler

Quadrature hybrids, also called branch-line couplers, are four-port couplers based on quarter-wavelength segments and have a structure as in Fig. 4.3.

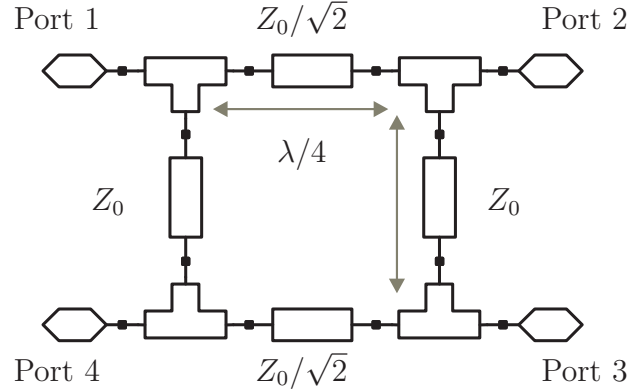


Figure 4.3.: Quadrature hybrid or branch-line coupler.

The inserted power at port 1 is equally divided at the output ports 2 and 3 at the  $\lambda/4$  resonance frequency. At this point port 4 is isolated. The output signals have a phase difference of  $\Delta\phi=90^\circ$ . The characteristic impedance of the series branches is  $Z_0/\sqrt{2}$ , whereas the parallel branches have a characteristic impedance of  $Z_0$ . Applying the same analysis as for the Wilkinson divider, the network can be summarized by its  $4\times 4$  scattering parameter matrix which has the following form

$$[S] = \begin{bmatrix} S_{11} & S_{12} & S_{13} & S_{14} \\ S_{21} & S_{22} & S_{23} & S_{24} \\ S_{31} & S_{32} & S_{33} & S_{34} \\ S_{41} & S_{42} & S_{43} & S_{44} \end{bmatrix} = \begin{bmatrix} 0 & -j/\sqrt{2} & -1/\sqrt{2} & 0 \\ -j/\sqrt{2} & 0 & 0 & -1/\sqrt{2} \\ -1/\sqrt{2} & 0 & 0 & -j/\sqrt{2} \\ 0 & -1/\sqrt{2} & -j/\sqrt{2} & 0 \end{bmatrix}. \quad (4.2)$$

The calculated performance of an ideal network according to (4.2) is depicted in Fig. 4.4. Similar to the previously discussed circuit the branch-line coupler exhibits also a narrowband performance, which is established by the quarter-wavelength segments. The response observed in Fig. 4.4 refers of course to an ideal network where limitations due to losses and finite quality factors are neglected. Nevertheless, in microstrip based implementations this type of circuits exhibit very low losses and can be used for applications where tight coupling is required over a limited bandwidth. Coupler topologies with larger operating bandwidths could be implemented as multiple section couplers as in [98], [99].

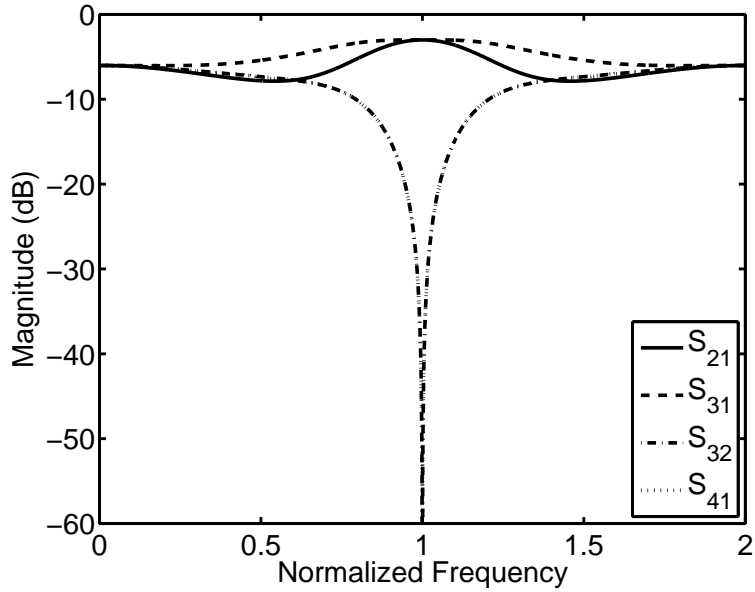


Figure 4.4.: Calculated S-parameters for an ideal branch-line coupler network.

### 4.3. Equivalent Quarter-Wavelength Segments

The proposed methodology is based on the principle of substituting  $\lambda/4$  transmission line segments of initial characteristic impedance  $Z$  with equivalent lowpass structures [100]. The resulting new transmission line segments can be made significantly shorter by raising their characteristic impedance level to  $\sqrt{2}Z$  and add shunt capacitors at the ends, as depicted in Fig. 4.5.

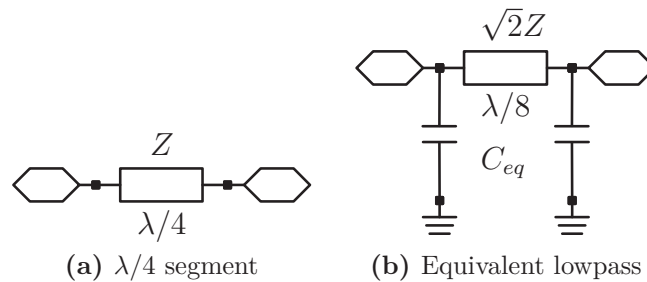


Figure 4.5.: Quarter-wavelength transmission line segment and its equivalent lowpass structure.

The capacitance value for the equivalent lowpass structure can be calculated by comparing the network parameter matrix of the quarter-wavelength segment with the corresponding matrix of the lowpass structure. For the general transmission line segment of characteristic impedance  $Z$  and electrical length  $\theta$ , the  $ABCD$  matrix

is given as

$$M = \begin{bmatrix} A & B \\ C & D \end{bmatrix} = \begin{bmatrix} \cos(\theta) & jZ \sin(\theta) \\ j \sin(\theta)/Z & \cos(\theta) \end{bmatrix}. \quad (4.3)$$

For the case where  $\theta=\pi/2$ , the matrix is reduced to

$$M = \begin{bmatrix} 0 & jZ \\ j/Z & 0 \end{bmatrix}. \quad (4.4)$$

The overall  $ABCD$  matrix of the equivalent lowpass structure can be calculated by multiplying the individual chain matrices of the two shunt capacitors and the reduced length transmission line segment. Thus,  $M_{total}=M_1 \cdot M_2 \cdot M_3$ , where

$$M_1 = M_3 = \begin{bmatrix} A & B \\ C & D \end{bmatrix} = \begin{bmatrix} 1 & 0 \\ j\omega C_{eq} & 1 \end{bmatrix} \quad (4.5)$$

$$M_2 = \begin{bmatrix} A & B \\ C & D \end{bmatrix} = \begin{bmatrix} \sqrt{2}/2 & jZ \\ j/(2Z) & \sqrt{2}/2 \end{bmatrix}. \quad (4.6)$$

The resulting overall  $ABCD$  matrix  $M_{total}$  then is given as

$$\begin{bmatrix} -\omega C_{eq}Z + 1/\sqrt{2} & jZ \\ j[\omega\sqrt{2}C_{eq}Z + (1/2) - \omega^2 C_{eq}^2 Z^2]/Z & -\omega C_{eq}Z + 1/\sqrt{2} \end{bmatrix}. \quad (4.7)$$

Comparing (4.4) and (4.7) results in a single solution for  $C_{eq}$

$$C_{eq} = \frac{1}{\omega\sqrt{2}Z} = \frac{1}{2\pi f\sqrt{2}Z}. \quad (4.8)$$

By presenting a closed formula in (4.8) it is possible to design fully scalable equivalent quarter-wavelength transmission line segments. For each starting characteristic impedance  $Z$  and resonance frequency  $f$  a single capacitance value  $C_{eq}$  is calculated. The performance equivalence in terms of transmission amplitude and phase of such structures is depicted in Figs. 4.6 and 4.7 respectively. From the presented response it becomes clear that the two networks have identical behavior around their resonance frequency in both amplitude and phase. Thus, as predicted by the previous analysis, the lowpass structure can substitute a quarter-wavelength transmission line segment without any noticeable change at the obtained resonance frequency. Nevertheless one significant difference which is noticed by the transmission characteristic of Fig. 4.6 is the lowpass behavior, which results in a roll-off of the transmission curve with increasing frequencies. This effect will become more significant when cascading several of these sections since the order of the resulting lowpass function will increase.

On the other hand it is evident that, by changing the capacitance value  $C_{eq}$  the resonance frequency  $f$  is altered. Limiting factors could only be the resulting

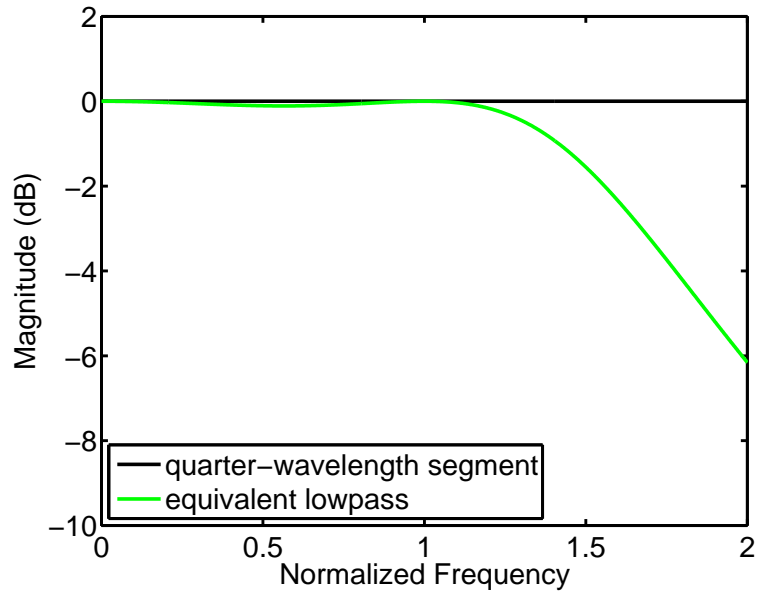


Figure 4.6.: Calculated transmission parameter  $S_{21}$  of an ideal quarter-wavelength transmission line segment of characteristic impedance  $Z_0=50\Omega$  and its equivalent lowpass network.

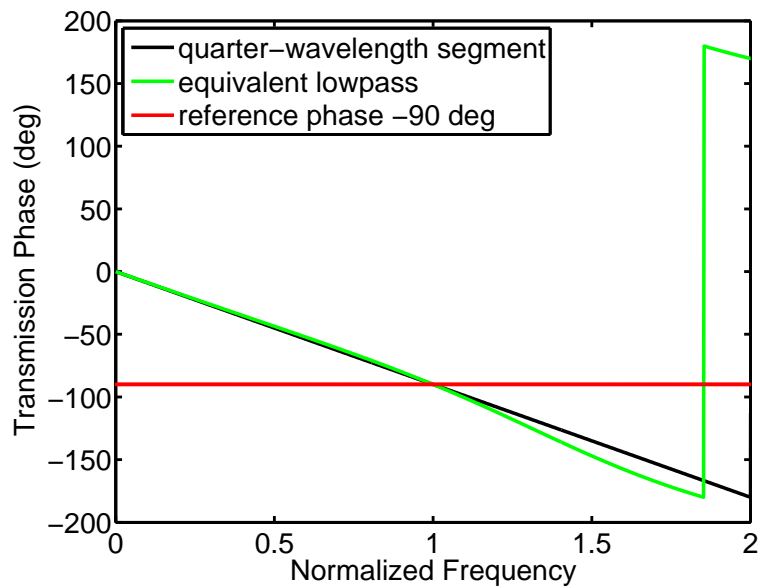


Figure 4.7.: Calculated transmission phase of an ideal quarter-wavelength transmission line segment of characteristic impedance  $Z_0=50\Omega$  and its equivalent lowpass network.

impedance values for real implementations, e.g. in microstrip technology and the varying line impedance for different frequencies. Nevertheless, by using tunable capacitors, such as BST varactors, a tuning functionality is achieved. Assuming an equivalent lowpass segment as in Fig. 4.5 with variable capacitance values for  $C_{eq}$  results in a frequency agile response presented in Figs. 4.8 and 4.9. As can be seen by the presented response, the corresponding magnitude and phase curves are shifted toward higher frequencies when the capacitance of the lowpass structure is lowered, as predicted by (4.8). The tuning range that is achieved is clearly demonstrated by the response of the transmission phase in Fig. 4.9. More than 30% tuning for the resonance frequency, namely the point where the phase reaches the value of  $-90^\circ$ , is achieved. The corresponding amplitude curve of Fig. 4.8 indicates the same shift in frequency. One issue that should be noted is the minor degradation in the transmission, which is noticed by a small amount of insertion loss. As was mentioned before changing the capacitance value  $C_{eq}$  results in a slightly detuned characteristic impedance. Nevertheless, since the observed degradation is negligible compared to the potential of achieving a wide tuning range, this technique is found to be interesting for microwave designs. Understanding this operational principle yields to designs of more complex topologies, which are based on  $\lambda/4$  segments.

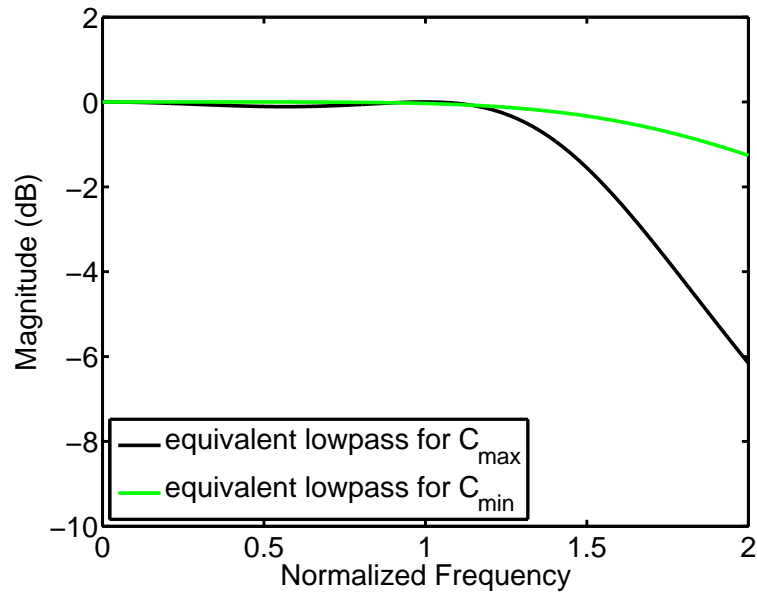


Figure 4.8.: Calculated transmission parameter  $S_{21}$  of an equivalent lowpass segment for two discrete capacitance values  $C_{max}$ ,  $C_{min}$ , where a tunability of 60% is assumed.

As an alternative to the equivalent lowpass structure of Fig. 4.5 a purely lumped element network can be used as indicated in Fig. 4.10. Applying the same methodology as for the reduced size equivalent transmission line segment, results simply

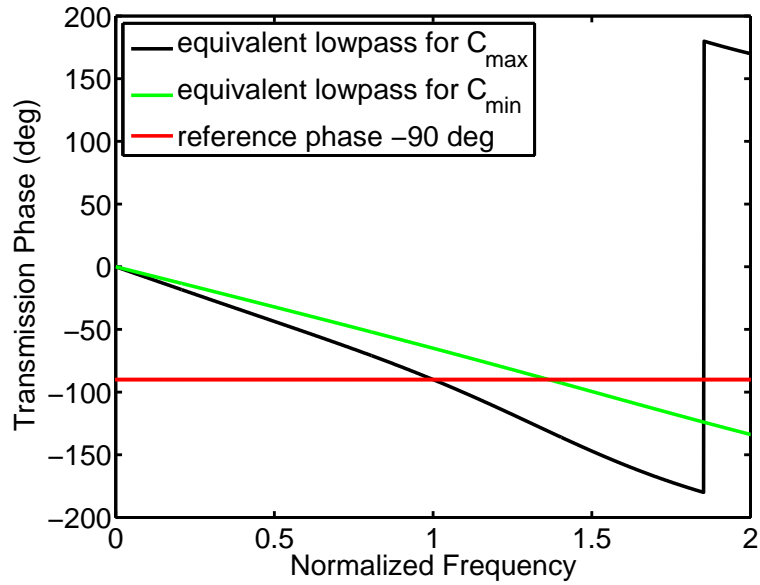


Figure 4.9.: Calculated transmission phase of an equivalent lowpass segment for two discrete capacitance values  $C_{max}$ ,  $C_{min}$ , where a tunability of 60% is assumed.

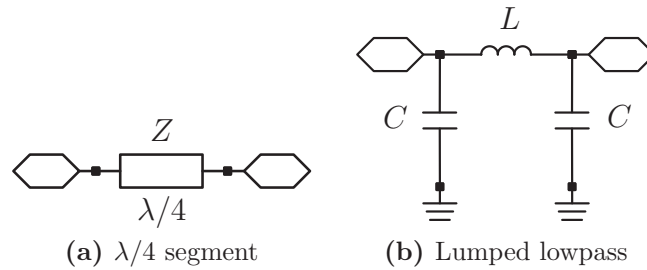


Figure 4.10.: Quarter-wavelength transmission line segment and its equivalent lumped element lowpass structure.

in multiplying the individual  $ABCD$  matrices as follows

$$\begin{aligned}
 M_{total} &= \overbrace{\begin{bmatrix} 1 & 0 \\ j\omega C & 1 \end{bmatrix}}^C \cdot \overbrace{\begin{bmatrix} 1 & j\omega L \\ 0 & 1 \end{bmatrix}}^L \cdot \overbrace{\begin{bmatrix} 1 & 0 \\ j\omega C & 1 \end{bmatrix}}^C \\
 &= \begin{bmatrix} 1 - \omega^2 LC & j\omega L \\ 2j\omega C - j\omega^3 LC^2 & 1 - \omega^2 LC \end{bmatrix}.
 \end{aligned} \tag{4.9}$$

Comparing this matrix expression to the initial quarter-wavelength matrix in (4.4)

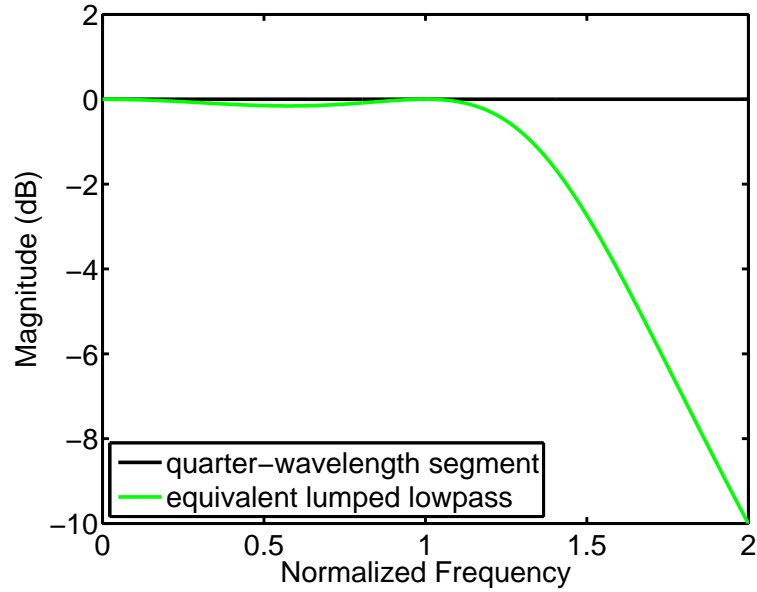


Figure 4.11.: Calculated transmission parameter  $S_{21}$  of an ideal quarter-wavelength transmission line segment of characteristic impedance  $Z_0=50\Omega$  and its equivalent lumped lowpass network.

yields the following set of equations

$$L = \frac{Z}{\omega} \quad (4.10)$$

$$C = \frac{1}{Z\omega}. \quad (4.11)$$

The corresponding response for the lumped element lowpass structure is given in Fig. 4.11, while in Fig. 4.12 the phase of the transmitted signals is presented. It is worth mentioning that the lumped lowpass exhibits a narrower resonance. This can be noticed also by the transmission phase curve in Fig. 4.12, which has a higher negative slope than the corresponding curve in Fig. 4.7. The tuning potential of the equivalent lumped lowpass segment is demonstrated in Figs. 4.13 and 4.14. Examples of lumped element couplers have been reported in [101]. Even tunable lumped branch-line couplers have been implemented on the basis of ferroelectric varactors [102].

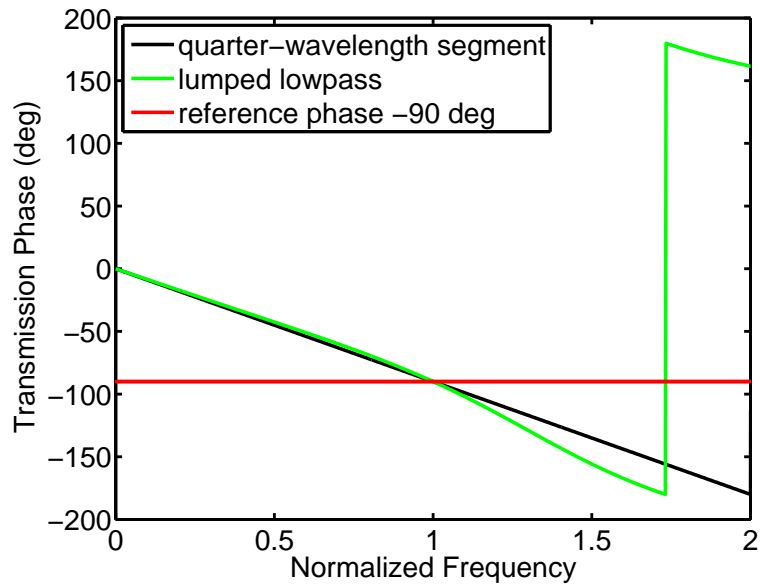


Figure 4.12.: Calculated transmission phase of an ideal quarter-wavelength transmission line segment of characteristic impedance  $Z_0=50\Omega$  and its equivalent lumped lowpass network.

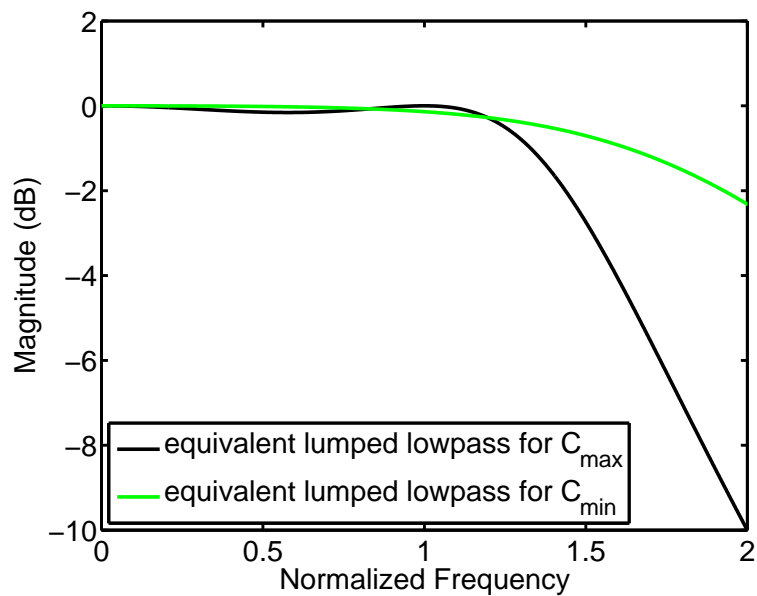


Figure 4.13.: Calculated transmission parameter  $S_{21}$  of an equivalent lumped lowpass segment for two discrete capacitance values  $C_{max}$ ,  $C_{min}$ , where a tunability of 60% is assumed.



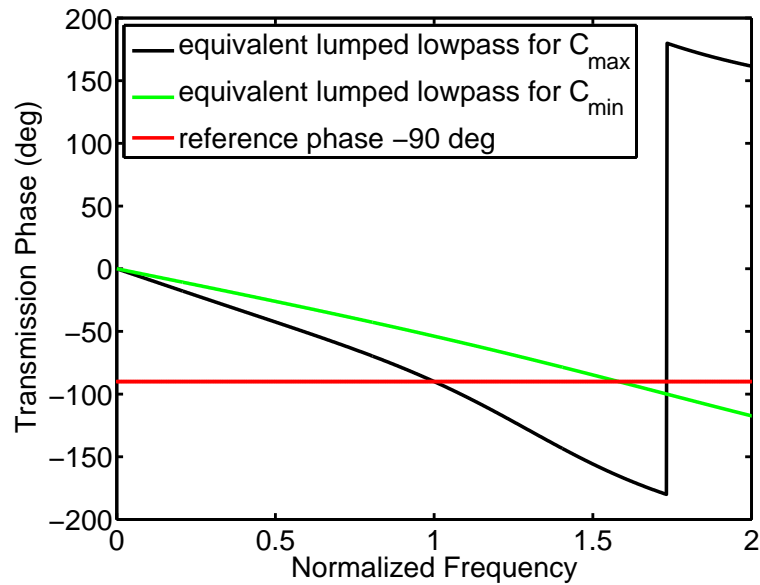


Figure 4.14.: Calculated transmission phase of an equivalent lumped lowpass segment for two discrete capacitance values  $C_{max}$ ,  $C_{min}$ , where a tunability of 60 % is assumed.

#### 4.4. Frequency Agile Wilkinson Divider

Based on the methodology which was described in the previous section, a reduced size topology of the original Wilkinson divider is presented in Fig. 4.15. The new transmission line segments have a shorter electrical length and a higher characteristic impedance. Lumped capacitors are used in order to compensate for the shorter propagation path.

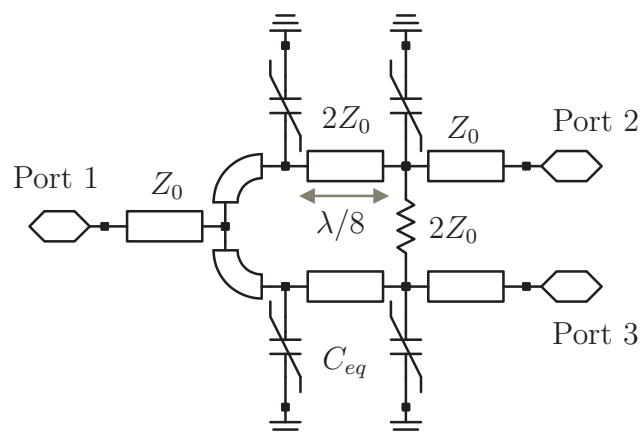


Figure 4.15.: Reduced size Wilkinson divider.

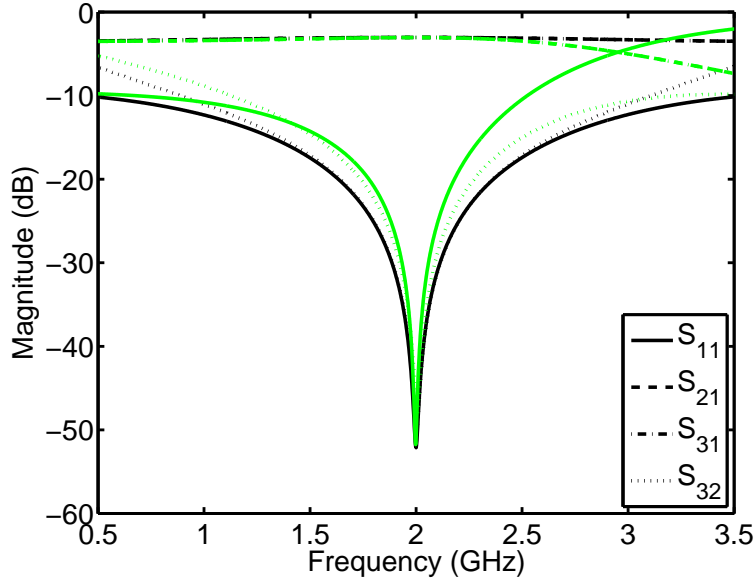


Figure 4.16.: Calculated scattering parameters of an ideal Wilkinson divider (black) and its modified reduced size version (green). Both circuits are designed for an operation at  $f=2$  GHz.

The  $\lambda/4$  transmission line segment of impedance  $\sqrt{2}Z_0$  can be substituted by an equivalent segment of length  $\lambda/8$  with an impedance of  $2Z_0$  by adding two lumped capacitors to the transmission line, with a capacitance value of

$$C_{eq} = \frac{1}{4\pi f Z_0}. \quad (4.12)$$

A comparison between a Wilkinson divider designed for operation at a frequency of 2 GHz and its modified reduced size version is given in Fig. 4.16. By observing the obtained response it becomes clear that the behavior at the frequency of resonance is identical. The modified version exhibits a somehow narrower resonance, which is caused by the dominant reactance change of the capacitively loaded transmission line segments. This effect can be also explained by the plotted phase curve in Fig. 4.7. The negative slope of the lowpass phase curve is higher than the corresponding phase curve slope of the quarter-wavelength transmission line segment. The aforementioned lowpass behavior is also witnessed for the transmission parameters  $S_{21}$  and  $S_{31}$  which tend to attenuate the higher frequency parts.

Assuming a reduced size Wilkinson divider, which is based on the ferroelectric varactors with a tunability of 60 %, results in the response presented in Fig. 4.17. Although some detuning occurs, as discussed previously, the isolation and return loss values are better than 15 dB at all tuning states. A tuning range of more than 25 % is achieved for the operating frequency while an absolutely symmetrical power

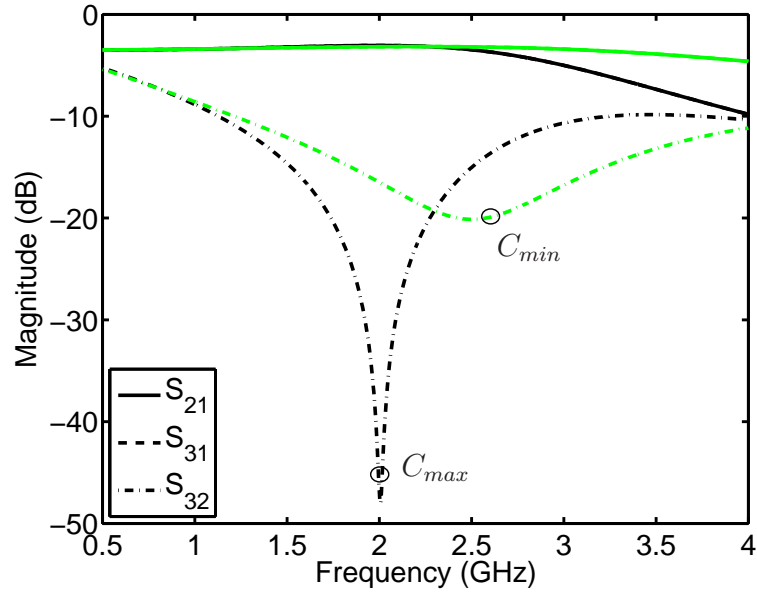


Figure 4.17.: Calculated scattering parameters of a reduced size Wilkinson divider for two discrete capacitances  $C_{max}$ ,  $C_{min}$ , where a tunability of 60% is assumed.

division is achieved. The proposed design allows for much more compact circuit dimensions compared to a multiple section network.

## 4.5. Frequency Agile Branch-Line Coupler

The reduced size topology in Fig. 4.18 uses the same principle as the previously discussed power divider. The series  $\lambda/4$  branches with  $Z_0/\sqrt{2}$  are substituted by lowpass segments with  $Z_0$  and shunt capacitors  $C_1 = 1/(2\pi f Z_0)$ . The parallel  $\lambda/4$  segments with  $Z_0$  are substituted by lowpass segments with  $\sqrt{2}Z_0$  and shunt capacitors  $C_2 = 1/(2\pi f \sqrt{2}Z_0)$ . In order to reduce the overall complexity the shunt capacitors at the transmission line ends were combined into the value

$$C_{eq} = C_1 + C_2 = \frac{1 + \sqrt{2}}{2\pi f \sqrt{2}Z_0}. \quad (4.13)$$

This equivalent capacitance serves as a shunt element for both transmission line segments that meet at each port, thus allowing for a more compact design with reduced complexity. The response obtained from such a network is given in Fig. 4.19 and Fig. 4.20 and compared to the original coupler performance.

As it is the case for the Wilkinson divider, the modified branch-line coupler has a slightly narrower resonance compared to the original coupler performance. One

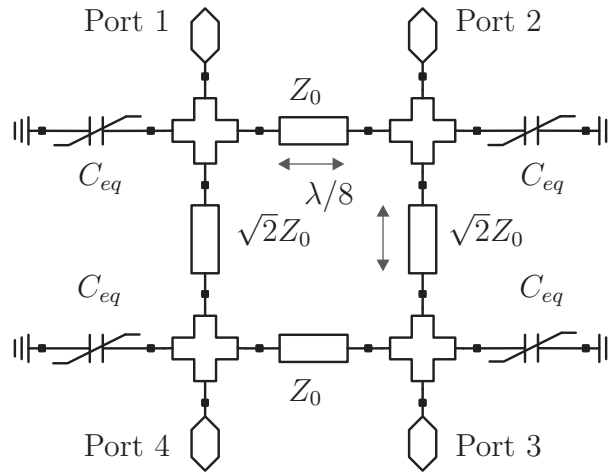
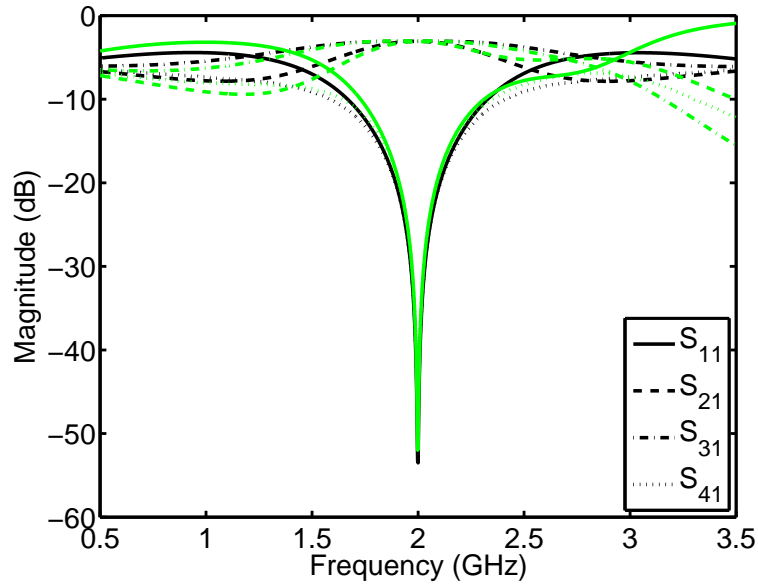


Figure 4.18.: Reduced size branch-line coupler.

Figure 4.19.: Calculated scattering parameters of an ideal branch-line coupler (black) and its modified reduced size version (green). Both circuits are designed for an operation at  $f=2$  GHz.

point which should be noticed is that an enhanced lowpass filtering is observed for the output branches. The varying roll-off in the transmission parameters  $S_{21}$  and  $S_{31}$  is a result of the higher order filtering, which is applied for a signal propagating from the input port 1 to the output port 3. Analogically to the previously investigated power divider, the branch-line coupler can be designed with a frequency agile behavior by using ferroelectric varactors. Assuming a tunability of 60% for

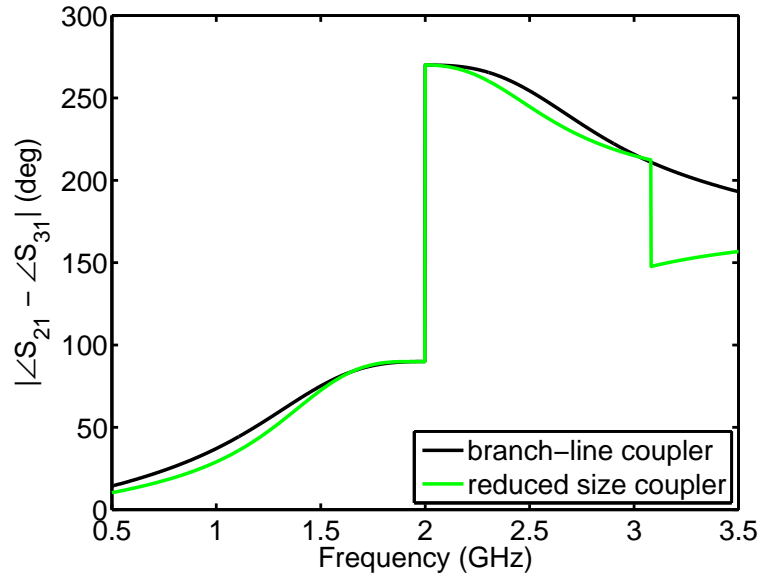


Figure 4.20.: Calculated phase difference between outputs of an ideal branch-line coupler and its modified reduced size version. Both circuits are designed for an operation at  $f=2$  GHz.

those tuning elements would result in a frequency agile performance as indicated in Fig. 4.21 and Fig. 4.22. By observing the obtained response it becomes evident that this methodology yields absolutely predictable coupler performance in both amplitude and phase over the whole tuning range. While a tuning of more than 25 % is obtained in the operating frequency, perfect 3 dB power coupling is retained. The desired phase offset of  $90^\circ$  at the output ports is obtained at all operating cases. Covering the same frequency bands with a multiple section coupler as in [103] would result in much larger circuit dimensions. Additionally, the lowpass filtering which is witnessed at all transmission paths would be absent. The significance of this effect will become more evident when discussing the performance of the implemented prototype circuits in the following chapter.

An operation in combination with a multi-band power amplifier, e.g. as a balanced amplifier, would be an interesting scenario since each supported frequency band could be covered selectively. Additional to this frequency agile operation, significant harmonics suppression would be performed due to the lowpass filtering for the output signals.

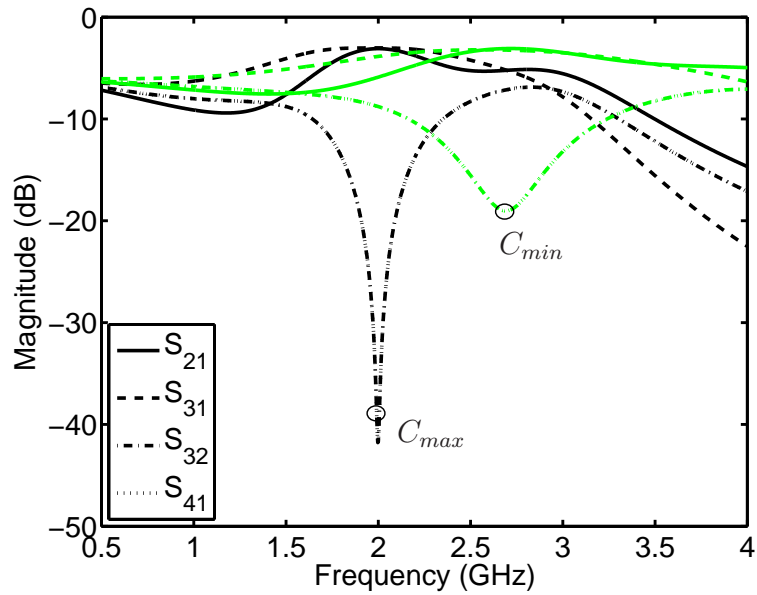


Figure 4.21.: Calculated scattering parameters of an ideal reduced size branch-line coupler for two discrete capacitance values  $C_{max}$ ,  $C_{min}$ , where a tunability of 60% is assumed.

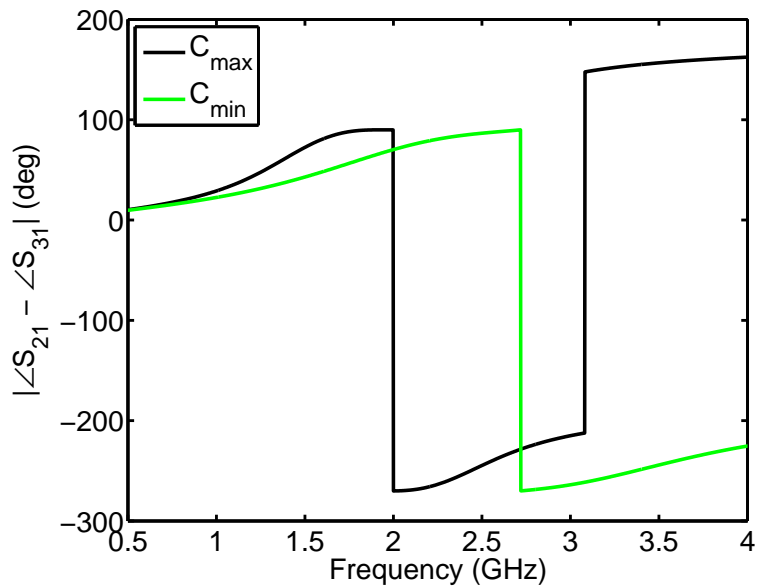


Figure 4.22.: Calculated phase difference between outputs of an ideal reduced size branch-line coupler for two discrete capacitance values  $C_{max}$ ,  $C_{min}$ , where a tunability of 60% is assumed.

# 5. Prototype Implementation and Experimental Results

In the previous chapters the focus was on the properties of the tunable passive devices and the operation inside microwave circuits in order to achieve frequency agile behavior. Filter designs as well as new approaches for designing reduced size frequency agile power dividers and couplers were presented. All aforementioned microwave circuits have been implemented in terms of prototype boards, which will be the subject of this chapter. Experimental results concerning small signal performance and linearity will be presented as well.

## 5.1. Assembly Techniques

The performance of hybrid microwave circuits consisting of planar transmission lines and discrete lumped components is greatly determined by the structure of the components and their assembly within the circuit. This becomes even more significant when considering tunable reactive components such as the ferroelectric varactors. Therefore care has to be taken for the assembly of such components since they are much more vulnerable than conventional industrial components, e.g. SMD type components. As was presented before, the used ferroelectric varactors have a parallel plate structure and can not be processed directly on a substrate along with other metal traces.

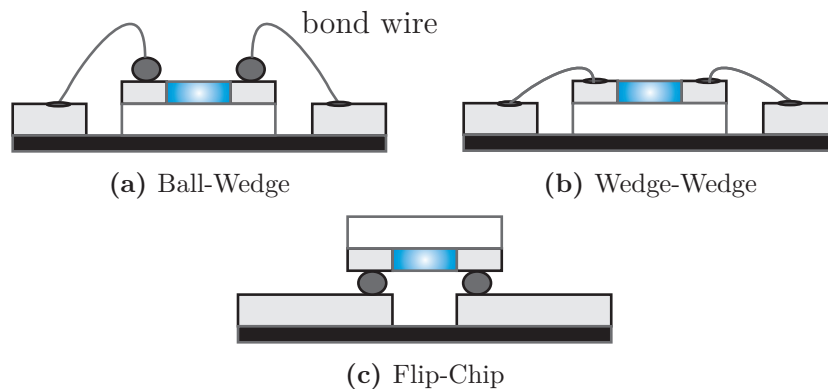


Figure 5.1.: Different assembly techniques for interconnections of hybrid circuits.

Conventional interconnection techniques such as soldering are not feasible for such components. Thus other approaches have to be considered. Some of the commonly used assembly techniques are presented in Fig. 5.1. Wire assemblies such as ball-wedge or wedge-wedge techniques have been used extensively for interconnecting semiconductor dies within front-end modules. In both cases a metallurgical connection between the chip pads and the board metal traces is established. The proper wire material, e.g. gold or aluminum, is depending on the bonding process, pad metalization, and the target application. One common characteristic of all wire assemblies is the fact that they suffer from parasitic inductances, which are associated with the wires. In case of wedge-wedge assemblies, the resulting wire inductances are significantly reduced since the wire loop is much smaller.

Assuming a simplified representation of the wire as a straight conductor of length  $l$  and radius  $r$ , results in a self-inductance according to the following expression [104]

$$L \approx \frac{\mu_0 l}{2\pi} \left[ \ln \left( \frac{2l}{r} \right) - \frac{3}{4} \right]. \quad (5.1)$$

Calculating the wire self-inductance for different values of the radius  $r$  and wire length  $l$  results in the data of Fig. 5.2. As it is clearly seen even short wire lengths result in noticeable inductance values especially for decreasing wires thicknesses. Techniques to reduce the interconnection inductance is to use parallel bond wires or thicker diameters. In both cases limitations are set due to the pad geometry of the chips which have to be interconnected. As opposed to wire assemblies, flip-chip techniques allow for compact and simpler interconnections between the chip pads and the metal traces. In this case stud bumps made of gold are placed on the varactor pads. The whole chip is then turned upside down and positioned on the metal traces. The connection is made either metallurgically or by using a conductive adhesive or solder paste. Such interconnections have been used widely for high frequency microwave circuits. Equivalent models can be used for the flip-chip interconnects [105] allowing for accurate simulations in the early circuit design stage. The impact of the wire inductance is demonstrated in Fig. 5.3, where the effective capacitance of a varactor in flip-chip assembly is compared to an assembly with a single bond wire on each varactor pad.

It is readily seen that for higher operating frequencies the parasitic wire inductance causes significant deviations from the nominal capacitance. The rapidly rising effective capacitance could be disadvantageously for broadband designs or multi-band operation. In contrast to that, the flip-chip configuration has an extremely flat response over frequency indicating its suitability even for high frequency operations. This feature along with the resulting smaller footprint of such assemblies makes flip-chip the most suitable solution for this task. Thus all prototype boards, which are about to be discussed, have been fabricated with flip-chip connected varactors. Gold stud bumps were placed on the varactor pads as indicated in Fig. 5.4



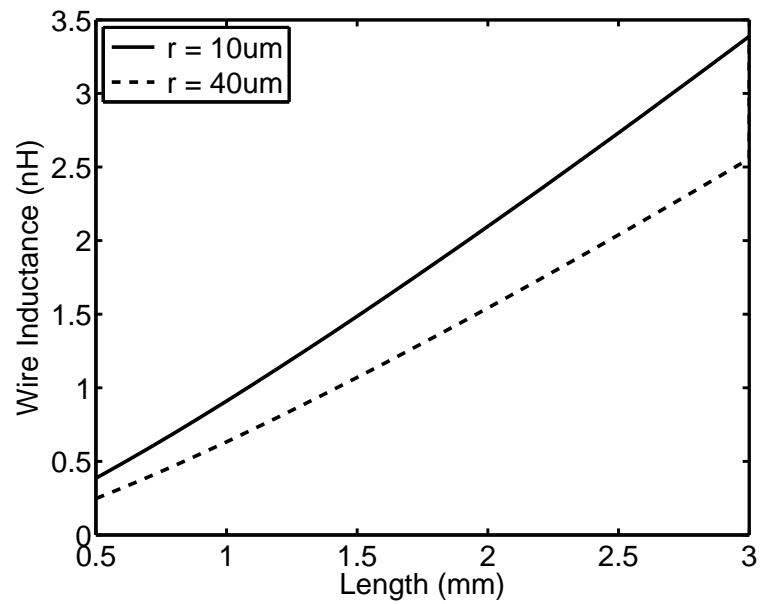


Figure 5.2.: Calculated self-inductance of a straight wire of length  $l$  and radius  $r$ .

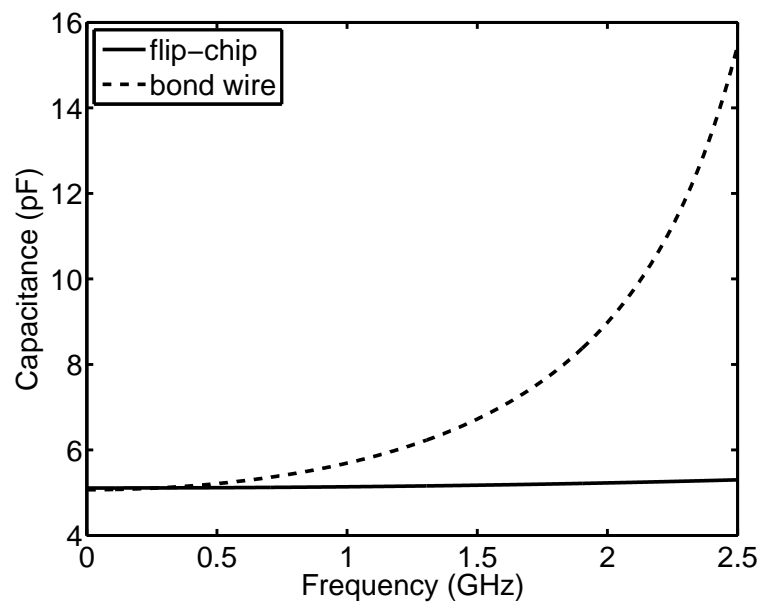


Figure 5.3.: Calculated effective capacitance of a 5 pF varactor interconnected in a flip-chip and ball-wedge assembly respectively.

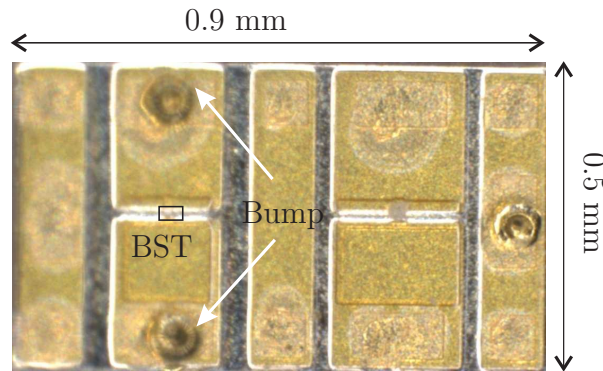


Figure 5.4.: Photograph of BST varactor chip with gold stud bumps positioned on the varactor pads.

and connected to the board metal traces via a conductive adhesive<sup>1</sup> which is heated up after positioning the ferroelectric varactor chips. By using this procedure no gold metalization is needed at the board metal traces allowing for inexpensive and rapid prototyping. The stud bumps have a diameter of approximately  $60 \mu\text{m}$  and occupy almost the whole pad area. It is readily seen that the gap between the metal traces for a flip-chip assembly corresponds to the mean pad distance of the chip. In this case a  $200 \mu\text{m}$  wide gap is chosen to ensure the proper positioning. As stated before, by using this type of assembly a more compact circuit design is resulting.

## 5.2. Tunable Lowpass Filter

The schematic of the fabricated 5<sup>th</sup> order tunable Chebyshev lowpass filter is depicted in Fig. 5.5.

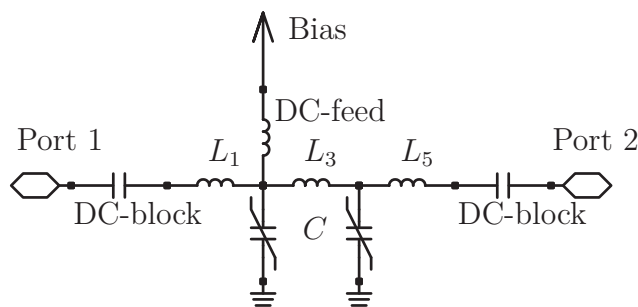


Figure 5.5.: Tunable 5<sup>th</sup> order lowpass filter with  $L_1=L_5=6.8 \text{ nH}$ ,  $L_3=12 \text{ nH}$  and BST varactors with a zero bias capacitance of  $C=3 \text{ pF}$ .

<sup>1</sup>Loctite 3880

Compared to the structure of Fig. 3.14 additional biasing components such as DC-block capacitors and one RF-choke inductor are used. These elements represent the mandatory overhead which is associated with such circuits, since the tuning voltage has to be applied to the varactors. With the DC-block capacitors current flow along the network ports is avoided, while the RF-choke inductor presents a high impedance path to the RF signal. Although the investigation in the previous chapters neglected the contribution of these elements to the circuit performance they have an impact in real implementations. Lumped inductors used as RF-chokes exhibit a finite isolation towards the RF signal and hence have to be chosen carefully. In the same way, DC-block capacitors have to be dimensioned for operation near their self resonance frequency in order to provide the lowest possible series impedance to the RF signal.

A photograph of the fabricated tunable lowpass prototype filter is given in Fig. 5.6. The prototype was fabricated on a Rogers RO3010 substrate ( $h=0.625$  mm and  $\epsilon_r=10.2$ ). The actual footprint of the circuit consists only of 0402-series SMD components and the BST varactors. The additional feeding microstrip lines serve for the bias and to mount the coaxial SMA connectors. The ferroelectric varactors were assembled in a flip-chip procedure in order to minimize the interconnection parasitics and the associated loss mechanisms for higher operating frequencies.

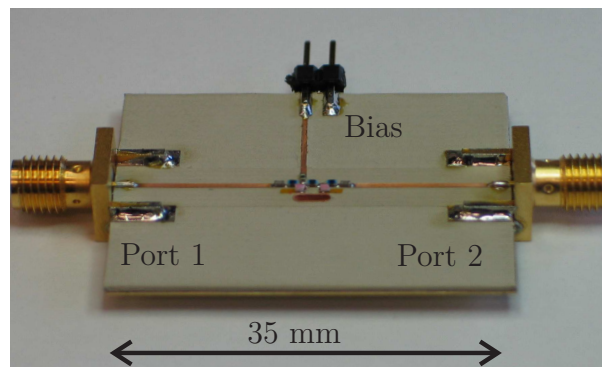


Figure 5.6.: Fabricated prototype board of the proposed tunable lowpass filter.

The measured filter performance for different bias voltages is depicted in Fig. 5.7. All scattering parameters were measured with a Rohde & Schwarz ZVB vector network analyzer (VNA). As it is readily seen, the lowpass filter exhibits two network zeros as predicted by the previously given analysis. By changing the bias voltage the capacitance values of the ferroelectric varactors are altered thus the passband of the filter is shifted according to (3.21) and (3.22). The second network zero is shifted from 1.5 GHz to approximately 2 GHz indicating a tunability of more than 30% for the filter. Attenuation levels of more than 30 dB are exhibited for the second harmonic at all operating bias states. Besides the significant tuning range some additional points should be noted. The observed high transmission losses of

about 4 dB in the passband are partially caused by the moderate quality factors of the ferroelectric varactors. Additionally, some performance degradation is also caused by the biasing components. The choke inductor does not provide a constant isolation over frequency since its impedance is increasing almost exponentially in the vicinity of the self resonance frequency. In a similar way, the series impedance presented by the DC-block capacitors is tending towards zero only for frequencies close to the resonance point. One possibility to reduce the number of biasing components is to use cascaded varactors and thus avoiding additional DC blocking capacitors.

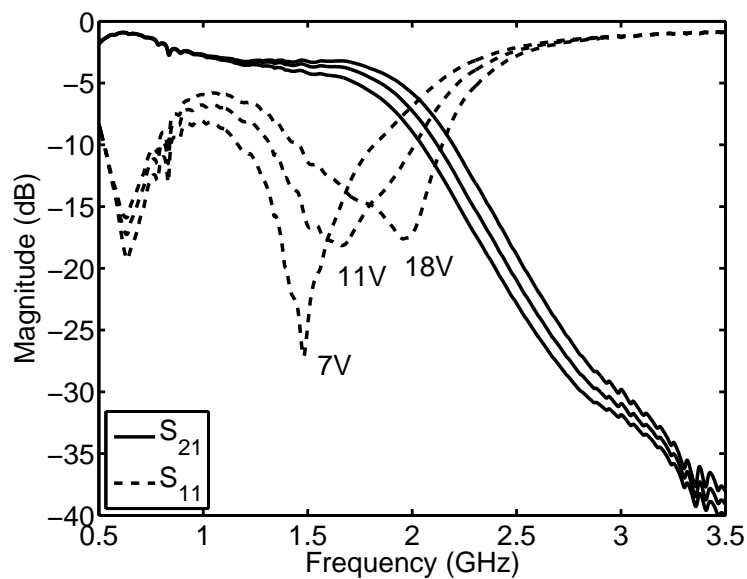


Figure 5.7.: Measured transmission and reflection parameters of the fabricated tunable lowpass filter for different bias voltages.

A comparison between measured and simulated performance for the proposed tunable lowpass filter is given in Fig. 5.8. The simulated curves refer to the results of the Momentum electromagnetic co-simulation. Higher insertion loss is noticed which is due to imbalances of the varactor values and some imperfections of the assembly. Nevertheless, a predictable performance is obtained. The potential of using such tunable filters, e.g. as an output stage of a multi-band power amplifier, is clearly demonstrated. Considering operation with varactors of higher quality factors would directly yield improved filter performance. Moreover, fabrication and assembly techniques with industrial processes would further enhance the filter performance and its reproducibility. The advantage over conventional filter approaches would be the frequency selective operation since each supported communication band could be covered separately resulting in improved return loss in the passband

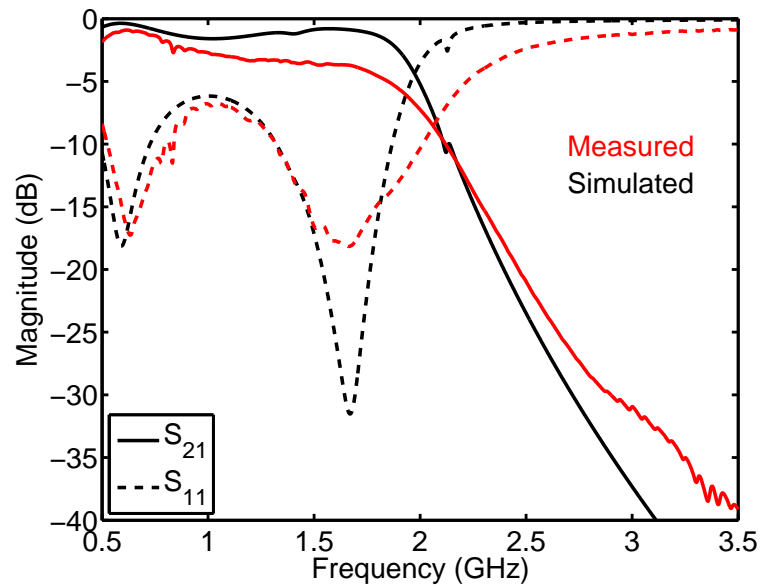


Figure 5.8.: Measured and simulated filter performance at a bias voltage of 11 V.

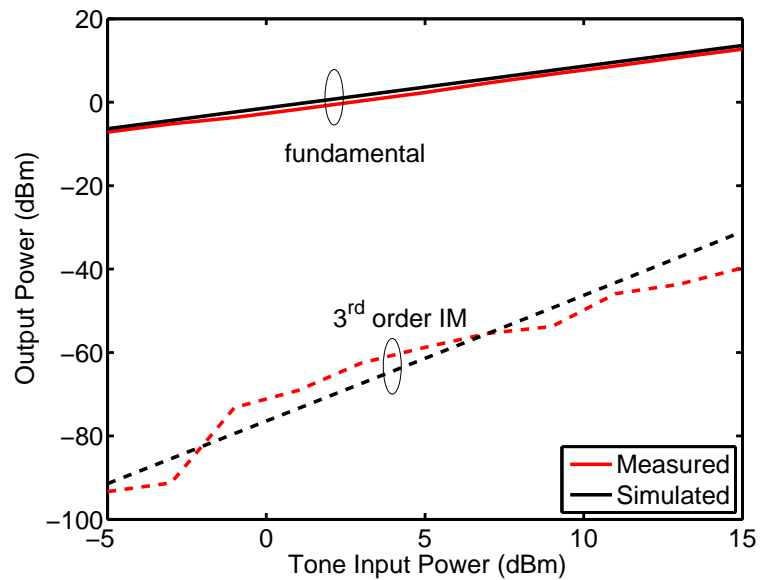


Figure 5.9.: Measured and simulated filter performance for a two-tone test with fundamental tone frequencies of  $f_1=1948$  MHz and  $f_2=1952$  MHz. The bias voltage was set to 20 V.

and harmonics suppression in the stopband. Since only one bias voltage is used there is no need for sophisticated tuning algorithms. Each bias voltage could be directly mapped to the resulting filter corner frequency. Additional to scattering parameter measurements a two-tone test (refer to Appendix B) was performed. A comparison between measured and simulated data is given in Fig. 5.9. It should be noted that the applied bias conditions establish an operation around the value of 20 V which exhibits the lowest possible capacitance slope. Thus the observed intermodulation products are considerably small. Further improvement of the linearity is expected by using cascaded varactors, as has been discussed previously.

### 5.3. Tunable Notch Filter

The schematic of the fabricated tunable bandstop filter is depicted in Fig. 5.10. Two cascaded BST varactors have been used. Thus a simplified biasing circuitry is obtained since there is no need for DC-block capacitors in the RF path.

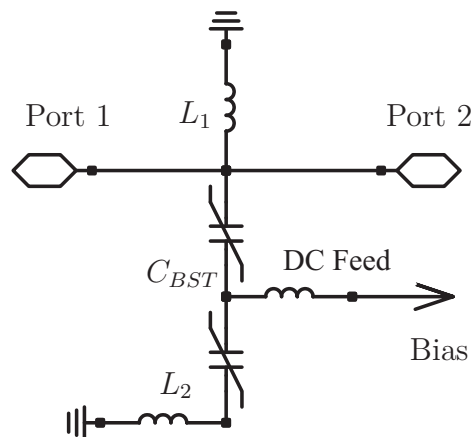


Figure 5.10.: Tunable bandstop filter with  $L_1=L_2=2.7$  nH and BST varactors with a zero bias capacitance of  $C_{BST}=5$  pF.

A photograph of the fabricated tunable lowpass prototype filter is given in Fig. 5.11. The prototype was fabricated on a Rogers RO3010 substrate ( $h=0.625$  mm and  $\epsilon_r=10.2$ ). The actual circuit footprint consists only of 0402-series SMD components and the BST varactors. The additional feeding microstrip lines serve for the bias and to mount the coaxial SMA connectors. The ferroelectric varactors were assembled in a flip-chip procedure similar to the previously discussed lowpass prototype. The measured scattering parameters for the implemented notch filter are presented in Fig. 5.12 and Fig. 5.13 respectively. A continuously tunable stopband filtering is achieved from 1.5 GHz to 2.1 GHz with a minimum attenuation of 17 dB. The return loss for the passband region is exceeding 13 dB while the insertion

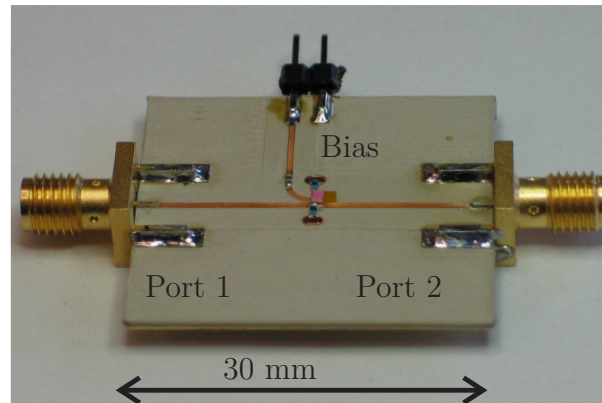


Figure 5.11.: Fabricated prototype board of the proposed tunable notch filter.

loss is approximately 1 dB. Thus selective filtering of unwanted blocking signals is possible in this frequency range.

As predicted by (3.27) and (3.28), the pole and zero allocation of the filter is shifted toward higher frequencies by raising the bias voltage and thus decreasing the capacitance value of the BST varactors. A comparison between measured and simulated filter performance for the same bias state is given in Fig. 5.14. As predicted by the previously given analysis, the notch filter exhibits one network zero and one pole resulting in a pass- and stopband, respectively. The measured allocation of the pass- and stopband matches the simulated data, whereas some deviations occur in the frequency region above the stopband. This difference is caused probably by the equivalent varactor model itself, since it is difficult to fit the model parameters to the actual measurement curves over the entire frequency region of interest and simultaneously for all bias conditions.

The linearity of the filter was determined by using the same two-tone setup as for the lowpass prototype. The bias voltage was set to 20 V in order to set the passband region around the center frequency of 1.95 GHz. The measured output power levels of the fundamental tone and the intermodulation products are given in Fig. 5.15. Similar to the previously discussed lowpass filter, the bias voltage of 20 V was chosen in order to move the filter passband in the region of the center frequency of 1.95 GHz. At the same time, a high tuning voltage results in an optimum operating bias point since the superposition of the DC and RF signal causes the lowest possible capacitance variation. The capacitance characteristic  $C(V)$  gets more flat with increasing bias, as demonstrated in Fig. 2.4.

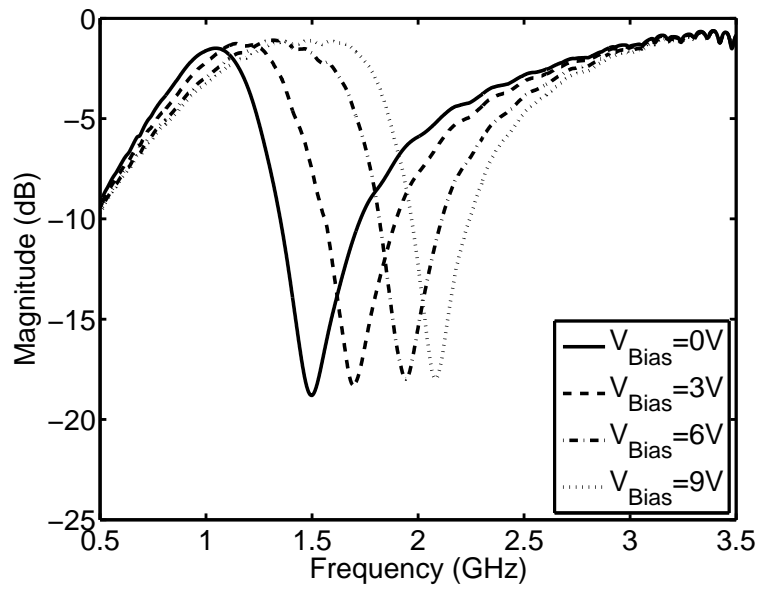


Figure 5.12.: Measured transmission parameter  $S_{21}$  of the fabricated tunable notch filter for different bias voltages.

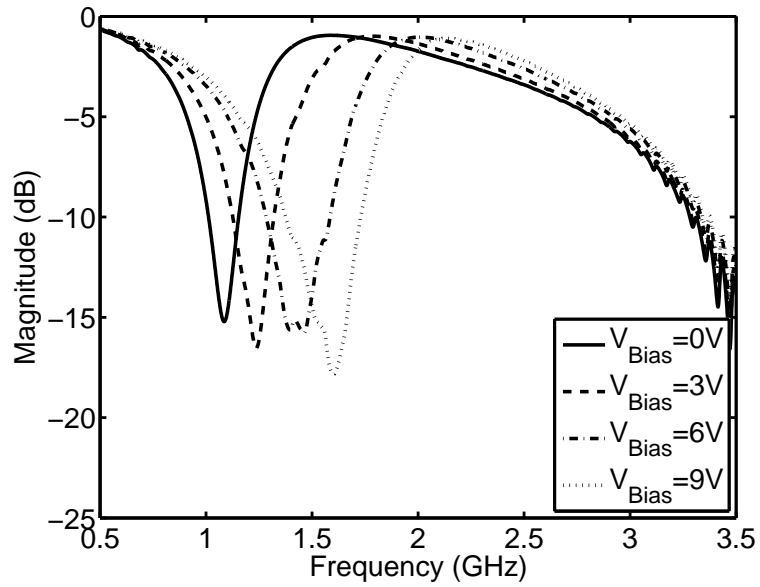


Figure 5.13.: Measured input reflection parameter  $S_{11}$  of the fabricated tunable notch filter for different bias voltages.



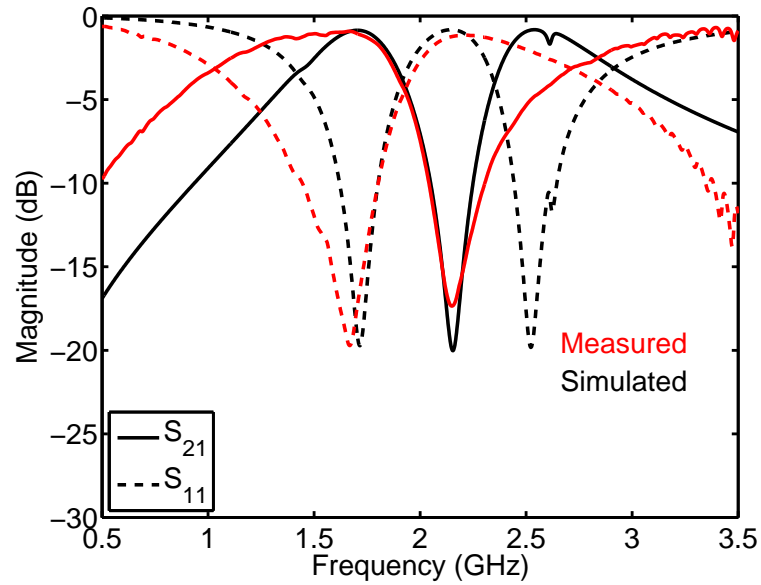


Figure 5.14.: Measured and simulated filter performance at a bias voltage of 11 V.

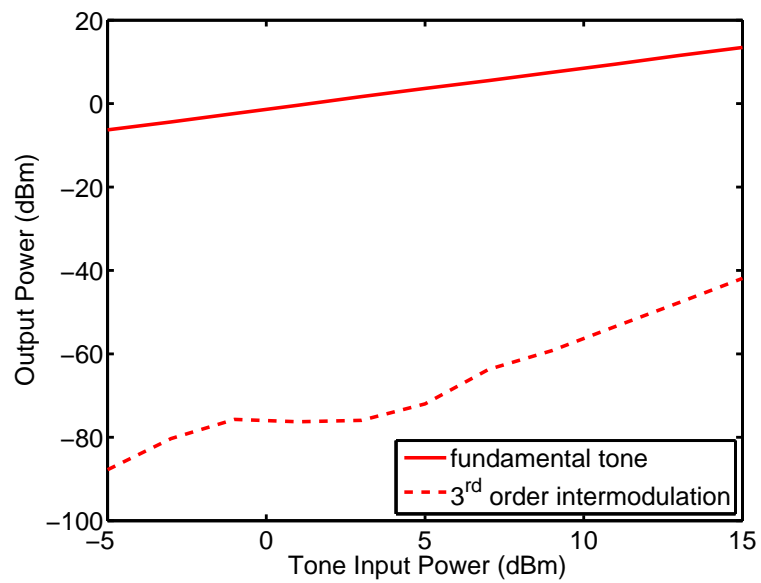


Figure 5.15.: Measured filter performance for a two-tone test with fundamental tone frequencies of  $f_1=1948$  MHz and  $f_2=1952$  MHz. The bias voltage was set to 20 V.

## 5.4. Tunable Comblin Filter

The proposed tunable comblin bandpass filter is presented in Fig. 5.16. It consists of three coupled microstrip resonator branches with tapped input and output ports. By using the BST varactors at the resonator ends a continuous tuning of the passband center frequency is achieved. Additional lumped components such as RF-choke inductors are used to establish the proper biasing conditions. The cascaded combination of  $C_1$  and  $C_{BST}$  represent the tunable capacitive load for the resonator branches. By cascading the two capacitors several advantages are obtained. The capacitor  $C_1$  operates as a DC-block element and voltage divider for the BST varactor at the same time. Thus there is no need for additional DC-block elements for the RF ports which would decrease the circuit performance. Since  $C_1$  is an SMD type capacitor it exhibits a much higher quality factor and in combination with the BST varactor an improved tunable load is presented to the resonator branches. The transition from the lower resonator end to the common capacitor pad is realized via gold bond wires. As opposed to a layout with metal traces connecting to  $C_2$ , this topology retains the coupling between the resonator branches.

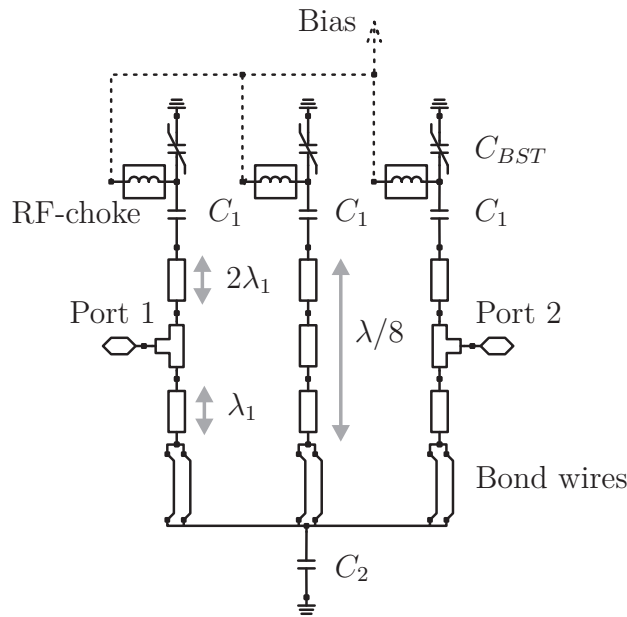


Figure 5.16.: Schematic of proposed tunable comblin filter.

A prototype of the proposed comblin filter was fabricated on a Rogers RO4003C substrate with height  $h=0.2$  mm and dielectric constant  $\epsilon_r=3.38$ . The circuit trace is depicted in Fig. 5.17. The microstrip resonators have a width of  $w=0.25$  mm and the spacing between them is  $s=0.15$  mm. All BST varactors have a zero bias capacitance of  $C_{BST}=5$  pF and were assembled in a flip-chip procedure in order to minimize the interconnection parasitics. Together with the fixed capacitors  $C_1=1$  pF

they form the variable capacitive load for the resonators. As previously discussed, an attenuation pole is introduced in the lower stopband through the capacitor  $C_2$ . In this case a fixed SMD type capacitor with  $C_2=12\text{pF}$  is used.

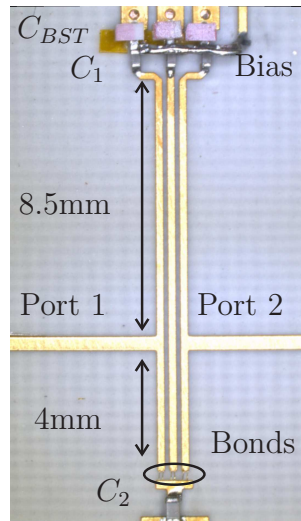


Figure 5.17.: Circuit trace of fabricated tunable combline filter.

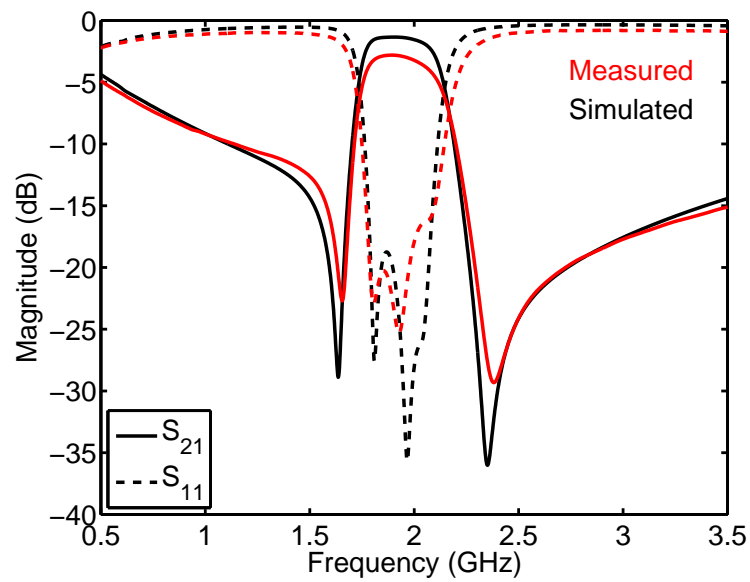


Figure 5.18.: Measured and simulated performance for the implemented prototype filter at zero bias.

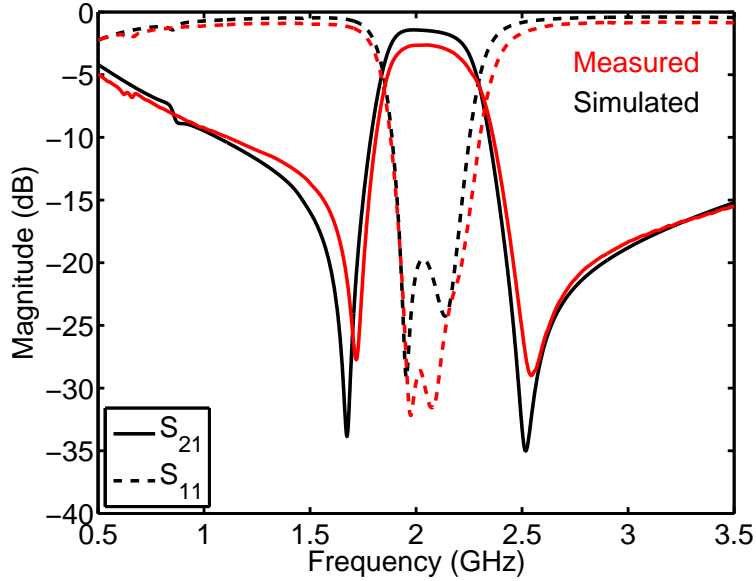


Figure 5.19.: Measured and simulated performance for the implemented prototype filter at bias voltage  $V_{Bias}=15$  V.

As presented in Fig. 5.18 and Fig. 5.19 excellent agreement is obtained between the simulated and measured performance for different bias states. The simulated data refers to the results of the co-simulation in ADS and Momentum. Minor deviations are due to varactor value imbalances and mismatches. The passband region of the filter can be tuned continuously from 1.8 GHz to 2.1 GHz with a worst case insertion loss of less than 3 dB while exhibiting return loss of more than 20 dB at all bias conditions. The slightly different performance in terms of transmission and return losses are due to the varying quality factors  $Q$  of the varactors. Each bias voltage results in a center passband frequency  $f_0$ , insertion- (IL), and return loss (RL), respectively. The filter performance at different bias states is summarized in table 5.1.

Table 5.1.: Tunable Bandpass Filter Performance

Bias (V)	$f_0$ (GHz)	IL (dB)	RL (dB)
0	1.85	2.8	20
5	1.90	2.7	22
10	1.97	2.6	26
15	2.02	2.6	28

The small tuning range is due to the chosen series connection of the BST varactor and the capacitor  $C_1$ . Furthermore, it should be noted that the attenuation pole in the upper stopband is clearly shifted when the bias is changed. The allocation of

the inserted attenuation pole in the lower stopband remains almost constant, since it is determined by the fixed value capacitor  $C_2$ . As a consequence, the bandwidth of the passband region is slightly altered. One important issue is, that the filter retains the shape of its passband characteristic at all bias conditions since the transition to both stopband regions are almost identical. Compensation of some minor difference in the stopband skirts could be implemented by using a variable capacitance for the lower resonator ends. A second tuning element would be inserted at the expense of higher circuit complexity and lower Q factor for the resonators. Nevertheless, a tunable filter bandwidth would result which is an attractive feature for reconfigurable front-end systems. Linearity issues were investigated by a two-tone test. The output power at one fundamental tone as well as the power of the third order intermodulation products is displayed in Fig. 5.20. The bias voltage was set to 5 V and the power of each input tone is swept over a range of 20 dB. For the maximum applied input power level of 15 dBm per tone, the output referred third order intercept point ( $OIP_3$ ) is calculated as

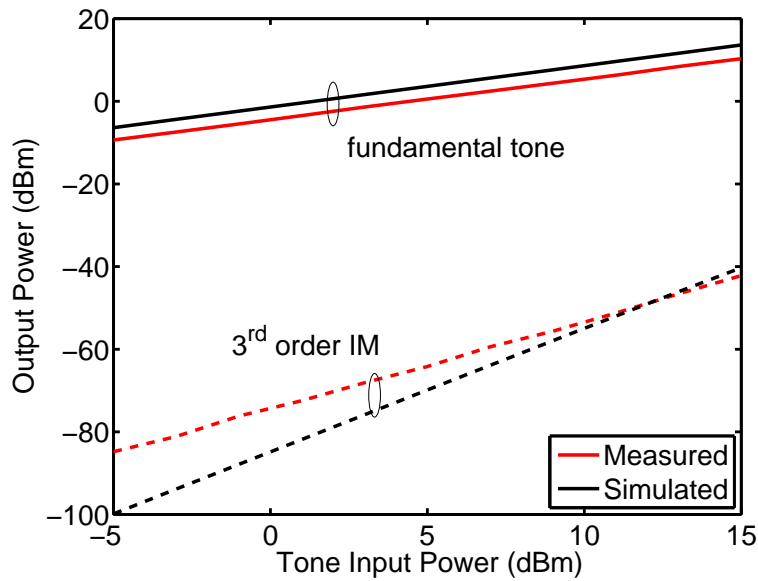


Figure 5.20.: Measured and simulated output power levels of fundamental tone and 3<sup>rd</sup> order intermodulation products for a two-tone setup with  $f_1=1948$  MHz and  $f_2=1952$  MHz.

$$OIP_3 = P_{out} + \frac{\Delta}{2} = 36.5 \text{ dBm.} \quad (5.2)$$

In (5.2),  $P_{out}$  and  $\Delta$  are the output power and the level difference between fundamental tone and intermodulation product, respectively.

## 5.5. Reduced Size Tunable Power Divider

The previously discussed frequency agile reduced size power divider is given in detail in Fig. 5.21, with all the needed biasing components indicated. A prototype board of the proposed tunable power divider was implemented on a Rogers RO3010 substrate with height  $h=1.27$  mm and dielectric constant  $\epsilon_r=10.2$ .

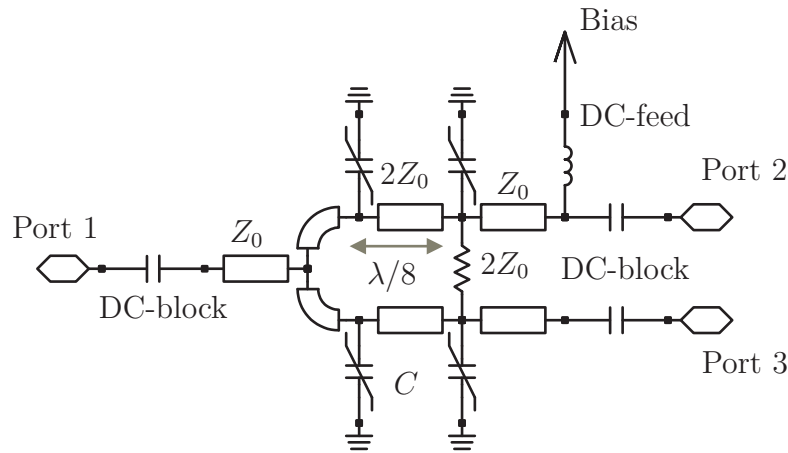


Figure 5.21.: Reduced size frequency agile power divider.

The circuit trace of the fabricated prototype is depicted in Fig. 5.22. Additional biasing components such as DC-block capacitors  $C_b$  at all RF ports and one RF-choke inductor  $L_c$  are used in order to establish the proper biasing conditions for the BST varactors. The DC-block capacitors behave at these frequencies nearly as a through connection while the choke inductor presents a high impedance path to the RF signal traveling on the microstrip lines. Therefore, the impact of the biasing elements can be almost neglected. It is worth mentioning that by using the proposed design it is possible to tune simultaneously all varactors. The bias circuitry is simplified since a single tuning voltage is required.

All BST varactors were assembled in a flip-chip procedure in order to eliminate the resulting parasitic wire inductance and the associated loss mechanisms of conventional wire assemblies. Gold stud bumps were placed on the varactor chip pads and connected to the metal traces of the board via a conductive adhesive. The measured transmission and reflection parameters of the tunable and reduced size power divider are presented for three discrete bias states in Figs. 5.23-5.25. From (4.12) the varactor values for the target frequency region are calculated. For the implemented prototype, varactors with nominal capacitance  $C=1$  pF serve as tuning elements. As can be seen the well known narrowband performance of the original Wilkinson divider is obtained for different frequencies. Tuning the varactor value leads to different resonance frequencies for the equivalent  $\lambda/4$  transmission line segments. A continuous tuning range from 1.7 GHz to 2.1 GHz is obtained.

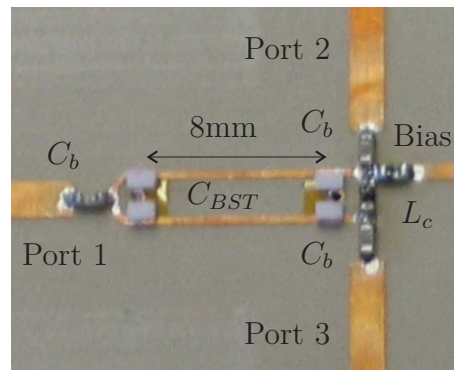


Figure 5.22.: Circuit trace of fabricated tunable power divider.

The insertion loss of the circuit, compared to the ideal 3 dB power splitting, varies from 0.6 dB to 1.2 dB within the operating bandwidth of each state.

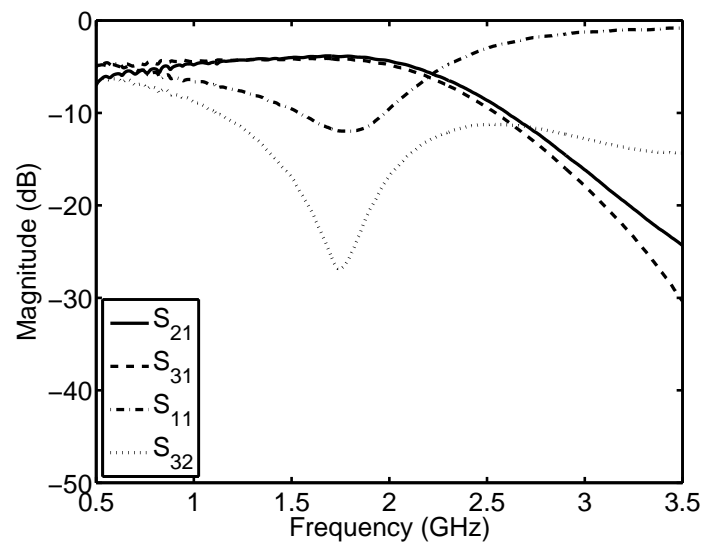


Figure 5.23.: Measured transmission and reflection S-parameters for tunable Wilkinson divider prototype at bias state  $V_{Bias}=2$  V.

The resulting amplitude and phase difference for the two transmission paths is depicted in Fig. 5.26. Symmetrical power splitting is achieved, in both amplitude and phase, thus fulfilling the divider operation. The indicated small differences are mainly due to varactor value tolerances. The worst case amplitude- and phase difference is 0.5 dB and  $9^\circ$ , respectively. A comparison between measured and simulated network performance is given in Fig. 5.27. As has been demonstrated previously, the electromagnetic co-simulation of the circuit traces and the BST varactor models leads to good agreement compared to the measurement results.

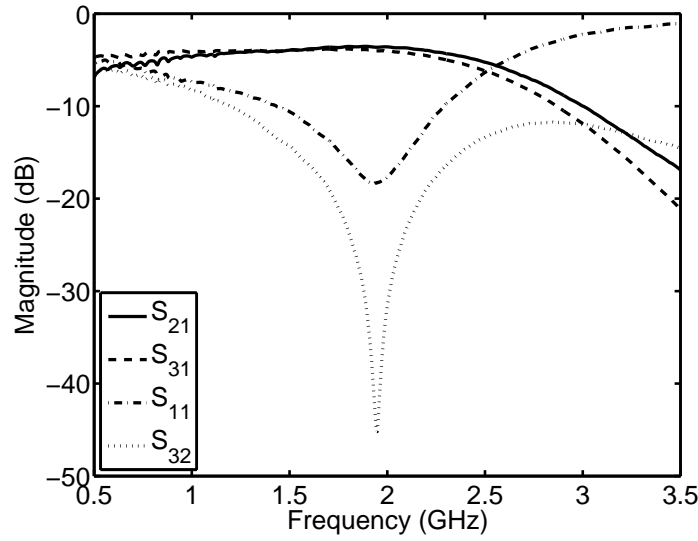


Figure 5.24.: Measured transmission and reflection S-parameters for tunable Wilkinson divider prototype at bias state  $V_{Bias}=6$  V.

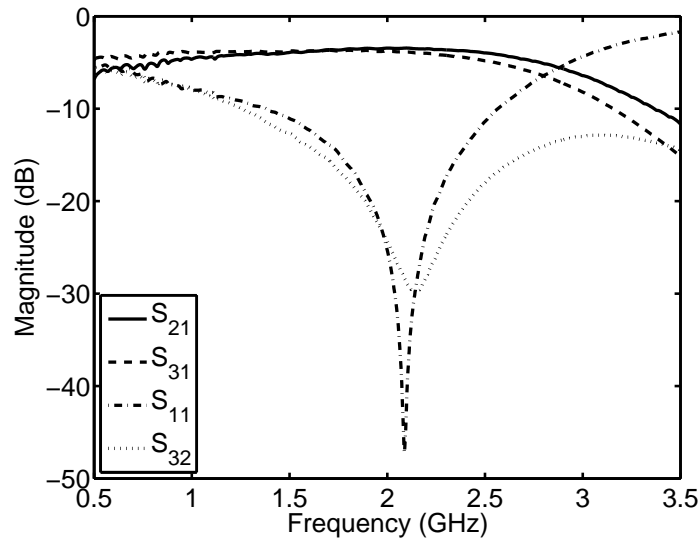


Figure 5.25.: Measured transmission and reflection S-parameters for tunable Wilkinson divider prototype at bias state  $V_{Bias}=17$  V.

Nonlinear effects caused by the ferroelectric varactors are quantified by a two-tone test procedure. The experimental results along with the simulated data are given in Fig. 5.28. The bias voltage was set appropriately to 7 V to shift the operating band around the frequency of 1.95 GHz. The advantage provided by the tuning



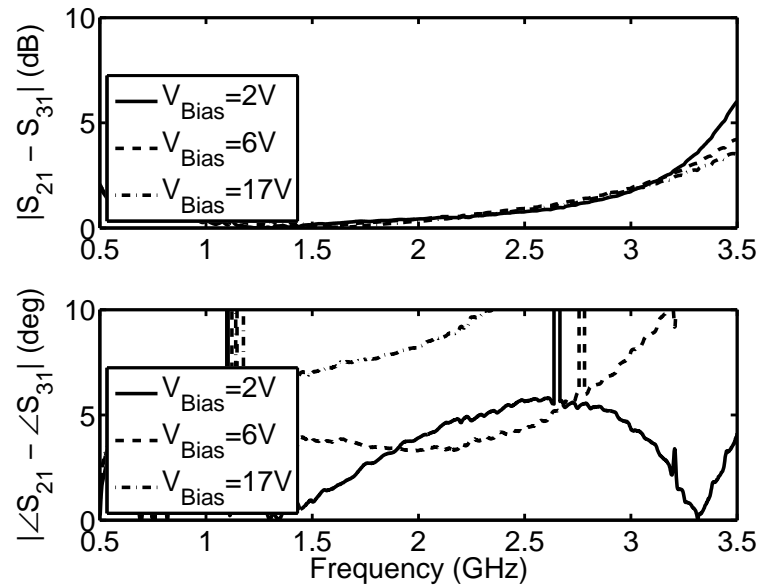


Figure 5.26.: Measured amplitude (top) and phase difference (bottom) for the transmission paths of the power divider.

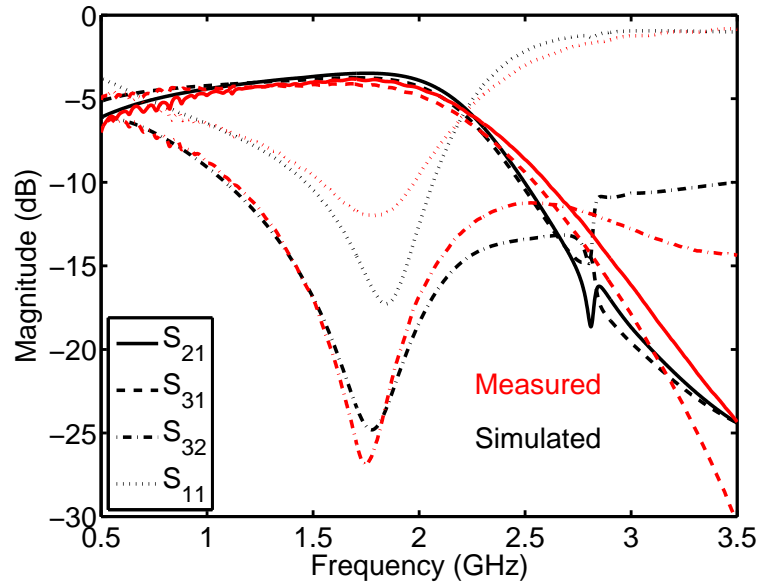


Figure 5.27.: Measured and simulated scattering parameters for fabricated tunable power divider at zero bias.

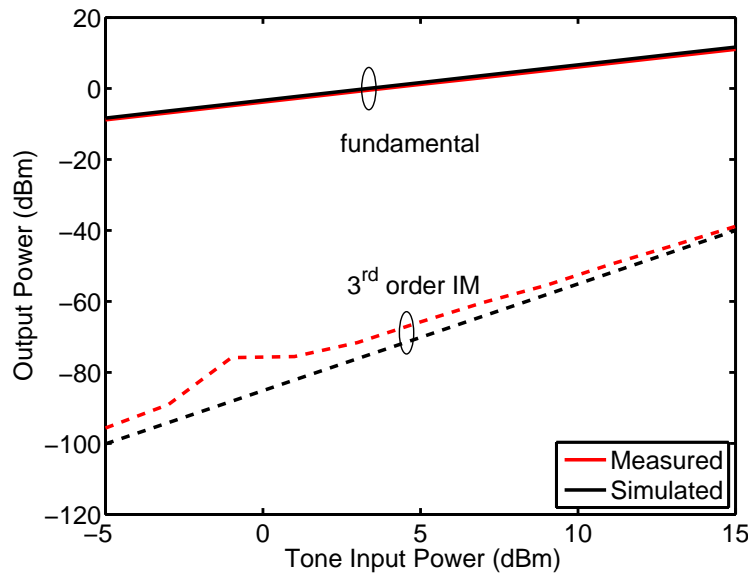


Figure 5.28.: Measured and simulated output power levels of fundamental tone and 3<sup>rd</sup> order intermodulation products at port 2 of the Wilkinson divider. A two-tone setup with  $f_1=1948$  MHz and  $f_2=1952$  MHz was used.

functionality concerns mainly the isolation between the output ports. The input return loss of the implemented prototype does not behave the same way due to possible varactor tolerances and some detuning of the characteristic impedance of the transmission lines. In this frequency region there are several communication bands allocated, thus frequency selectivity is desired. Compared to a reduced size power divider with fixed capacitors improved isolation is achieved at the other operating frequency bands. All figures reveal the inherent lowpass behavior, thus harmonic radiation would be suppressed significantly when considering an operation in a transceiver front-end system. At all operating bias states the second harmonic is attenuated by more than 20 dB. Reconfigurable power dividers based on a multiple section design have been also reported in [106]. Such solutions suffer from an increased form factor.

## 5.6. Reduced Size Tunable Branch-Line Coupler

The previously discussed frequency agile reduced size branch-line circuit with all its biasing components is depicted in Fig. 5.29. A prototype board of the proposed tunable coupler circuit was implemented on a Rogers RO3010 substrate with height  $h=1.27$  mm and dielectric constant  $\epsilon_r=10.2$ .

The circuit trace of the fabricated prototype is depicted in Fig. 5.30. Additional

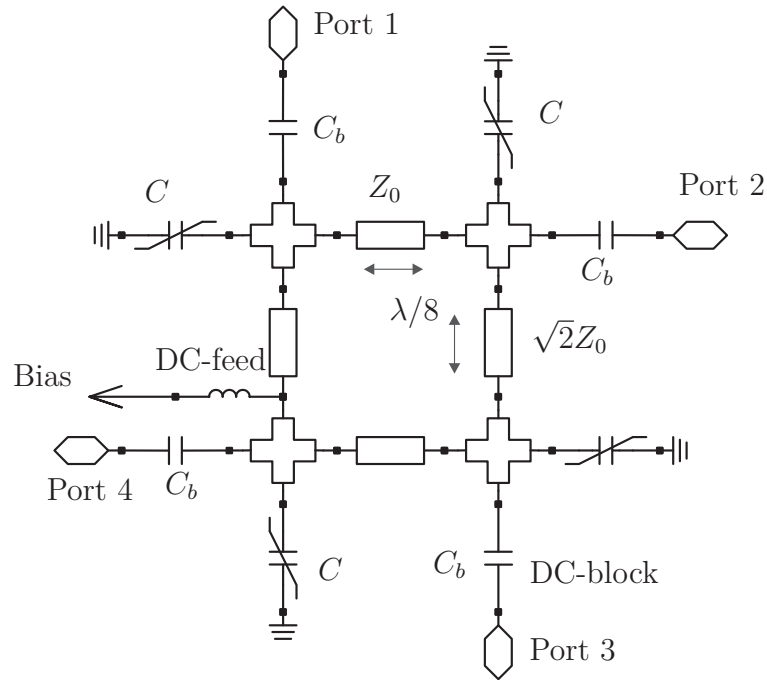


Figure 5.29.: Reduced size frequency agile branch-line coupler.

biasing components such as DC-block capacitors  $C_b$ , at all RF ports, and one RF-choke inductor  $L_c$  are used in order to establish the proper biasing conditions for the BST varactors. A carefully chosen layout ensured a total symmetric structure, which is of great significance for obtaining the desired amplitude and phase relations. The DC-block capacitors at these frequencies nearly behave as a through connection while the choke inductor presents a high impedance path to the RF signal. Therefore, the impact of the biasing elements can be almost neglected. It is worth mentioning that by using the proposed design it is possible to tune simultaneously all varactors. The bias circuitry is simplified since no sophisticated tuning algorithm is needed.

For the branch-line coupler varactors with nominal capacitance  $C=3$  pF serve as tuning elements, according to (4.13). The S-parameter response for three discrete bias states is presented in Figs. 5.31-5.33. All transmission and reflection parameters exhibit the well known branch-line coupler performance. A continuous tuning range from 1.8 GHz to 2.3 GHz is obtained.

Additional to the ideal 3 dB coupling, the insertion loss varies from 2 dB to 2.7 dB depending on the applied bias state. The amplitude and phase difference between the two transmission paths is shown in Fig. 5.34. The worst case deviation from the nominal phase difference of  $90^\circ$  is  $\pm 5^\circ$ . Similar low differences are observed for the amplitude, where the maximum difference for each bias state is 0.4 dB. Thus the coupler operation is fulfilled at different operating frequencies. Tunable branch-

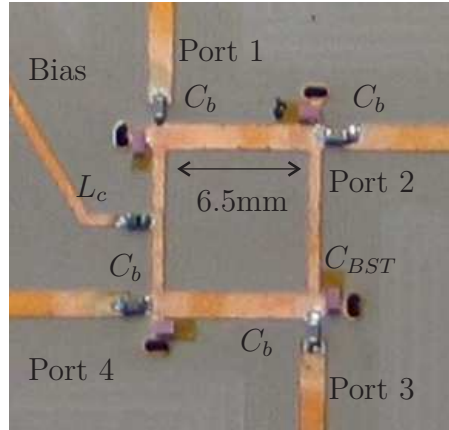


Figure 5.30.: Circuit trace of fabricated tunable branch-line coupler.

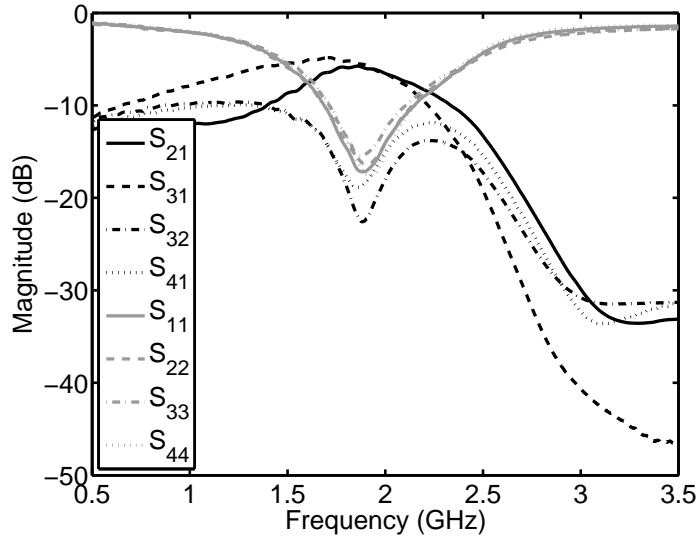


Figure 5.31.: Measured transmission and reflection S-parameters for tunable branch-line coupler prototype at bias state  $V_{Bias}=5$  V.

line couplers based on a transmission line approach have been reported previously in [107], [108], [109]. The advantage of the implemented circuit is the size reduction in combination with the frequency agility.

Similar to the Wilkinson divider prototype, excellent agreement between simulation and measurements is obtained, as indicated in Fig. 5.35. Minor deviations are caused by varactor value tolerances and mismatches. Similar to the implemented power divider the circuit indicates its lowpass characteristic since higher order harmonics are suppressed in the transmission paths. Operating these couplers along with multi-band power amplifiers, e.g. in a Doherty topology [110], would result

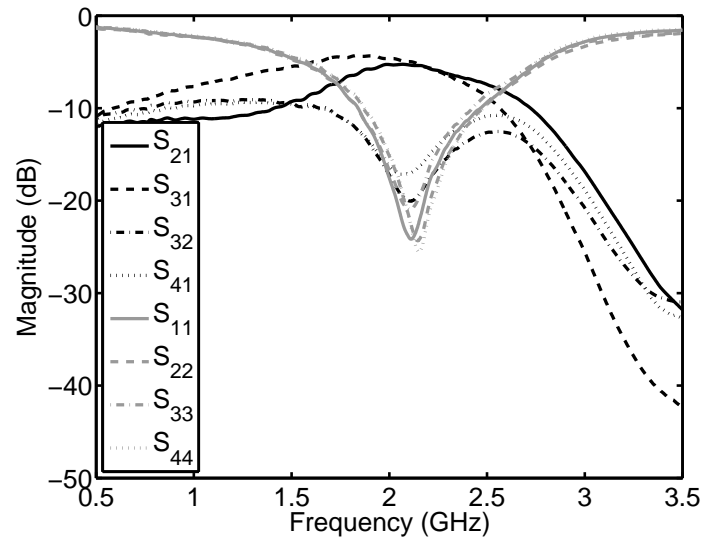


Figure 5.32.: Measured transmission and reflection S-parameters for tunable branch-line coupler prototype at bias state  $V_{Bias}=9$  V.

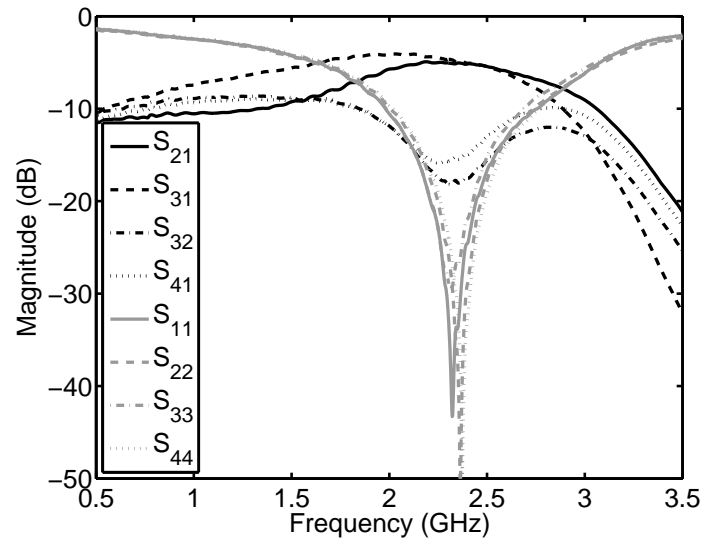


Figure 5.33.: Measured transmission and reflection S-parameters for tunable branch-line coupler prototype at bias state  $V_{Bias}=15$  V.

in frequency agile transmitter stages with suppressed harmonic radiation and thus improved spectrum purity. The achieved attenuation for the second harmonic exceeds 30 dB at all operating conditions. This attenuation level is comparable to the achieved stopband attenuation of the implemented 5<sup>th</sup> order lowpass filter which

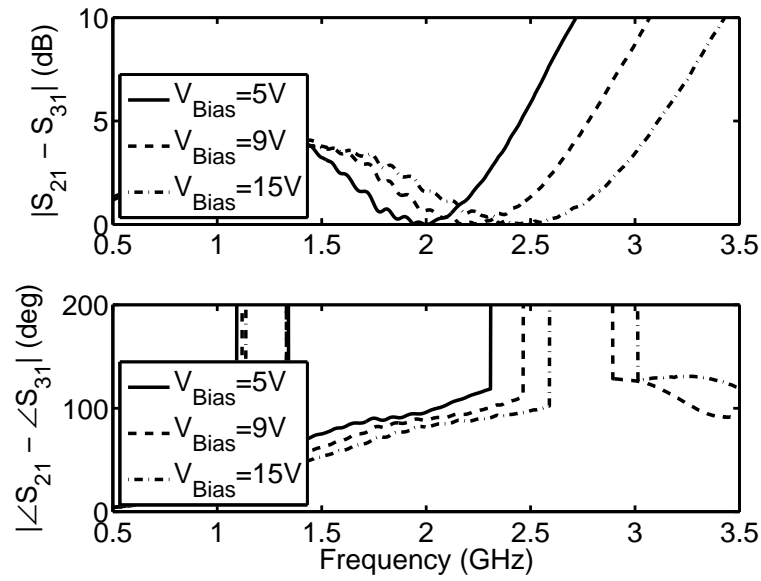


Figure 5.34.: Measured amplitude (top) and phase difference (bottom) for the transmission paths of the branch-line coupler.

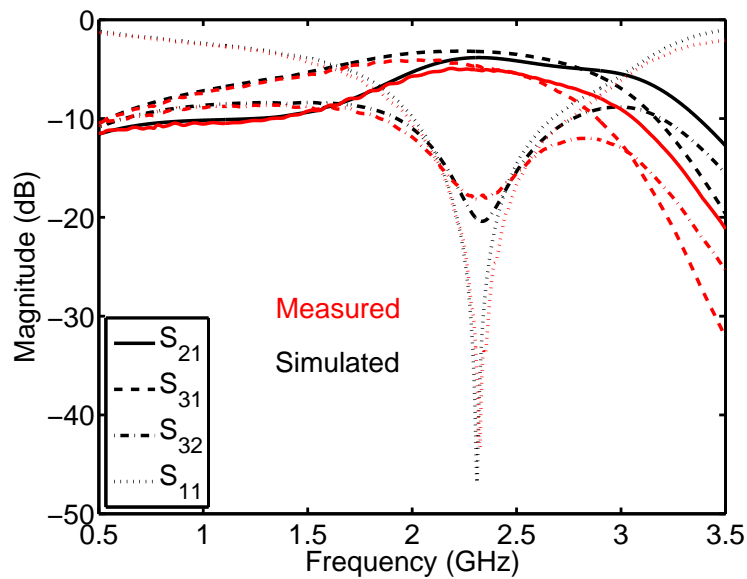


Figure 5.35.: Measured S-parameters at  $V_{Bias} = 15$  V and simulated data for the tunable branch-line coupler prototype.

was discussed previously. For determining the nonlinear effects caused by the ferroelectric varactors a two-tone test was performed. The experimental results and

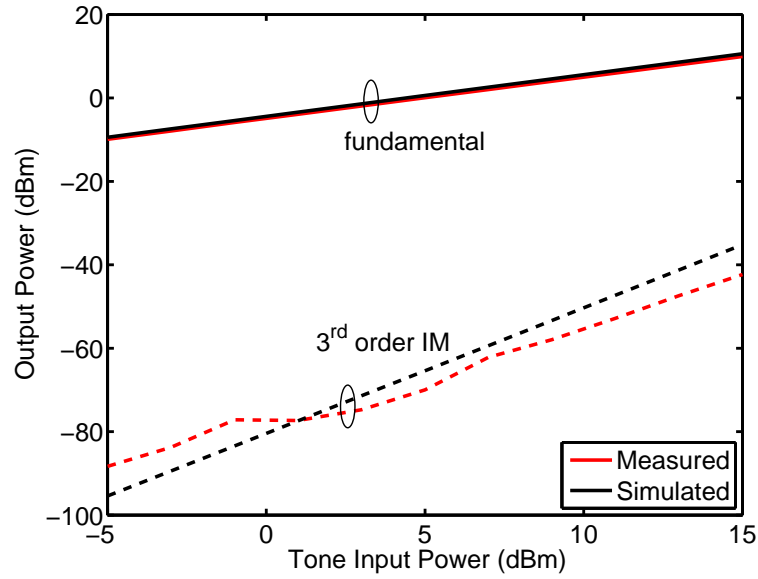


Figure 5.36.: Measured and simulated output power levels of fundamental tone and 3<sup>rd</sup> order intermodulation products at port 2 of the branch-line coupler. A two-tone setup with  $f_1=1948$  MHz and  $f_2=1952$  MHz was used.

simulated data are given in Fig. 5.36. The bias voltage was set appropriately to 7 V to shift the operating band around the frequency of 1.95 GHz.

From the previously presented data it can be seen, that the proposed novel frequency agile circuits are suitable for operation in multi-band systems since they provide a reconfigurable and predictable performance. Combining such reconfigurable circuits with conventional active front-end blocks, such as power amplifiers, mixers, etc. would be a step forward to the identified goal of reducing the radio front-end complexity. Using frequency agile microwave circuits would enable a multi-band operation for RF front-end systems while reducing the number of functional blocks.

# 6. Reconfigurable Front-End Systems

So far in this work, tunable microwave circuits have been treated as stand-alone subsystems and characterized for their small and large signal performance. Main objective of this chapter is to relate them to possible applications in transceiver architectures for both mobile and stationary communication devices. Realistic operating scenarios with complex modulated signals, e.g. UMTS 3GPP WCDMA, will be discussed and demonstrated for one of the implemented prototype subsystems.

## 6.1. Modulation Analysis

Investigating radio transmission systems typically involves modulated signals, which are used for modulating the sinusoidal RF carrier. In digital modulation schemes data sequences consisting of discrete symbols, namely binary characters, are used to modify the physical parameters of the carrier. Principally, a radio signal  $s(t)$  is characterized by its amplitude  $A$ , frequency  $f$ , and phase  $\phi$ . Digital modulation on either of those parameters results in what is known as amplitude shift keying (ASK), frequency shift keying (FSK), and phase shift keying (PSK), respectively. An arbitrary time variant radio signal would have the general form

$$s(t) = A \cos(2\pi ft + \phi). \quad (6.1)$$

The same equation can be transformed into the equivalent expression

$$s(t) = A \cos(\phi) \cos(2\pi ft) - A \sin(\phi) \sin(2\pi ft) \quad (6.2)$$

$$= I \cos(2\pi ft) + Q \sin(2\pi ft). \quad (6.3)$$

From (6.3) it is seen that the signal consists of two orthogonal parts of the same frequency  $f$ . Usually they are referred as the in-phase  $I$  and the quadrature component  $Q$ . Knowing the carrier frequency allows for a complete characterization of  $s(t)$  by its  $I$  and  $Q$  components. This calculation is typically performed in the baseband processing of communication devices. An equivalent representation of the signal  $s(t)$  is given in Fig. 6.1.



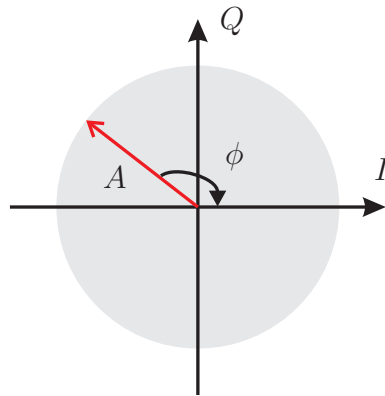


Figure 6.1.: Vector representation of signal  $s(t)$ .

In the baseband representation the signal vector is described by its amplitude  $A$  and phase  $\phi$ . At any given time  $t$ , the signal is characterized completely by its  $I$  and  $Q$  components since the vector represents the instantaneously sampled continuous signal. Based on this representation different modulation techniques can be analyzed in a straightforward manner.

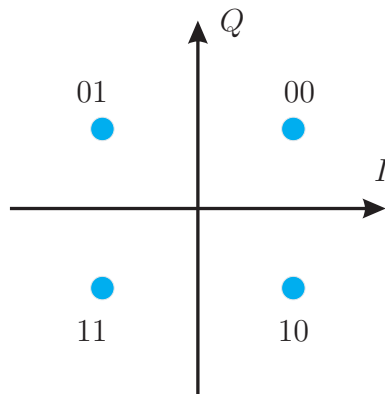


Figure 6.2.: Constellation diagram of QPSK signal.

In UMTS based communication systems QPSK (Quadrature Phase Shift Keying) is the used modulation technique. The phase  $\phi$  of the RF carrier signal is modulated by four different digital symbols, as indicated in Fig. 6.2. Each symbol reflects a pair of bits and is assigned to a defined phase of the signal vector. In the demodulation process the incoming signal is analyzed for its  $I$  and  $Q$  components and the transmitted data is detected by the signal vector phase. Imperfections in WCDMA transmitters, e.g. nonlinear effects or I-Q imbalances, can cause deviations in the amplitude or phase of the received vector signal. Such errors can be quantified by a unit called EVM (Error Vector Magnitude), which is illustrated in

Fig. 6.3.

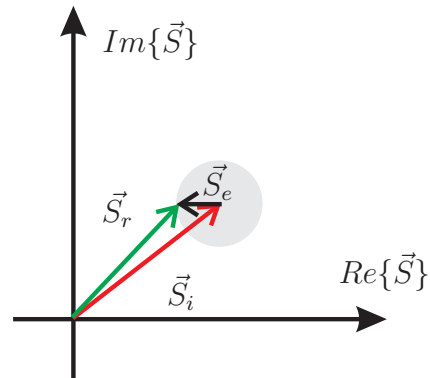


Figure 6.3.: Error vector magnitude definition.

The error magnitude  $\vec{S}_e$  represents the difference between the ideal signal vector  $\vec{S}_i$  and the actually received one  $\vec{S}_r$ , thus the EVM unit is formed by the following expression

$$EVM = \frac{\vec{S}_e}{\vec{S}_i} = \frac{\vec{S}_r - \vec{S}_i}{\vec{S}_i}. \quad (6.4)$$

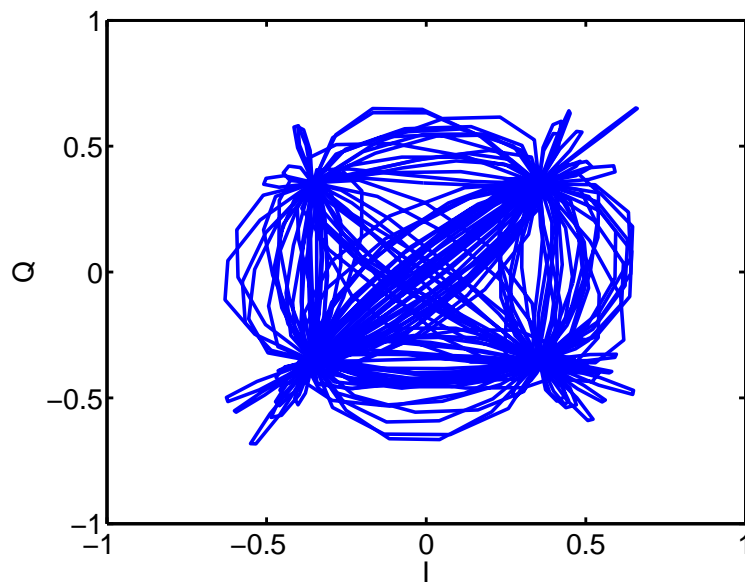


Figure 6.4.: Measured trajectory of QPSK modulated signal.

According to the current 3GPP specification a worst case EVM of 17.5% is allowed for WCDMA transmitters. A typical trajectory of a QPSK modulated

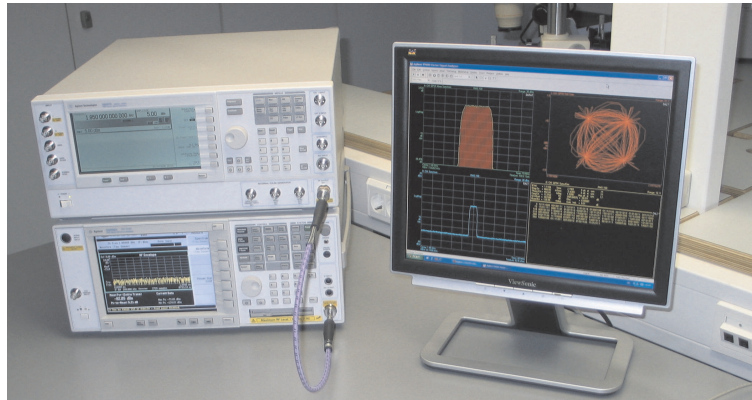


Figure 6.5.: Measurement setup for modulation analysis.

signal is given in Fig. 6.4. The used vector signal generator is an Agilent PSG and the resulting rms EVM value of the generator did not exceed 1%. Thus it is suitable for performing the compliance test. The modulated signal with a center frequency of 1.95 GHz is captured and analyzed by an Agilent PSA spectrum analyzer through the VSA demodulation software, as depicted in Fig. 6.5.

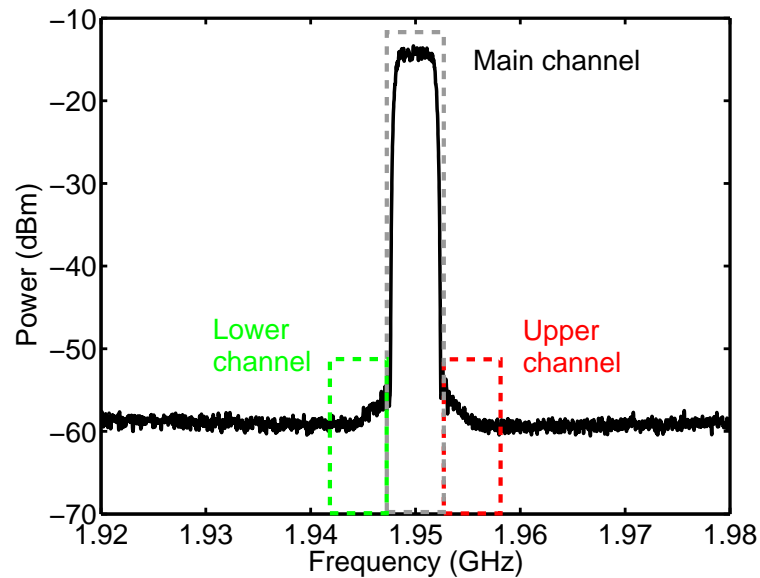


Figure 6.6.: Measured spectrum of WCDMA modulated signal.

The corresponding spectrum of the modulated signal with a channel bandwidth of 5 MHz is depicted in Fig. 6.6. The signal bandwidth is mainly determined by the chip rate of 3.84 Mchip/s and the QPSK modulation, thus the resulting bandwidth is approximately 3.84 MHz. Pulse shaping in the baseband generator is performed in

order to shape the transmission spectrum. A root raised cosine filter with a roll-off factor of 0.22 is used resulting in an increase of the signal bandwidth by 22%. The resulting total signal bandwidth is thus approximately 4.6 MHz. Nonlinearities in the power amplifiers result eventually in a distorted output spectrum. Additionally interactions of several signals can give rise to spectral power components in the vicinity of the considered communication channel. One criterion to quantify the aforementioned effect is known as adjacent channel leakage power (ACLP) which alternatively can be expressed in terms of a ratio (ACLR) between the power levels of adjacent channels. In this case only the directly adjacent channel with an offset of 5 MHz is considered. For base station transmitters, the ACLR in the adjacent frequency channel has to be 45 dB or more. For mobile stations the corresponding value is depending on the power class and channel spacing, according to table 6.1.

Table 6.1.: ACLR specifications for mobile stations.

Power Class	Output Power (dBm)	Channel Spacing (MHz)	ACLR limit (dB)
3	24	5	33
3	24	10	43
4	21	5	33
4	21	10	43

## 6.2. **Balanced Amplifier**

Transmitter stages are one of the key blocks within communication front-end architectures. In modern front-end implementations the transmitter includes mainly a power amplifier module and an output filter stage, at least when considering the analog high frequency part of it. Since several frequency bands have to be covered, the mainstream approach incorporates multi-band power amplifiers, which can be used for several communication bands, which are allocated over a relative small frequency range. The filtering which is applied to the power amplifier output signal is performed either by a lowpass filter or a duplexer. In conventional implementations there is no possibility of introducing reconfigurability in terms of selective filtering. Novel design approaches, using the successfully implemented circuits, can be used to modify already existing systems. A suitable example is the balanced type power amplifier [111] as illustrated in Fig. 6.7.

Two identical amplifiers are fed by a quadrature coupler which produces two signals with a phase difference of  $90^\circ$ . Their amplified output signals are combined again with a branch-line coupler which is connected in reverse order. One of the advantages of this topology is that reflected waves due to mismatch at the power amplifier ports pass through the couplers and are canceled out at the input and

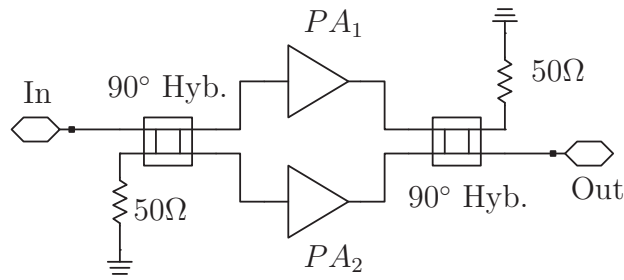


Figure 6.7.: Balanced power amplifier topology with branch-line couplers.

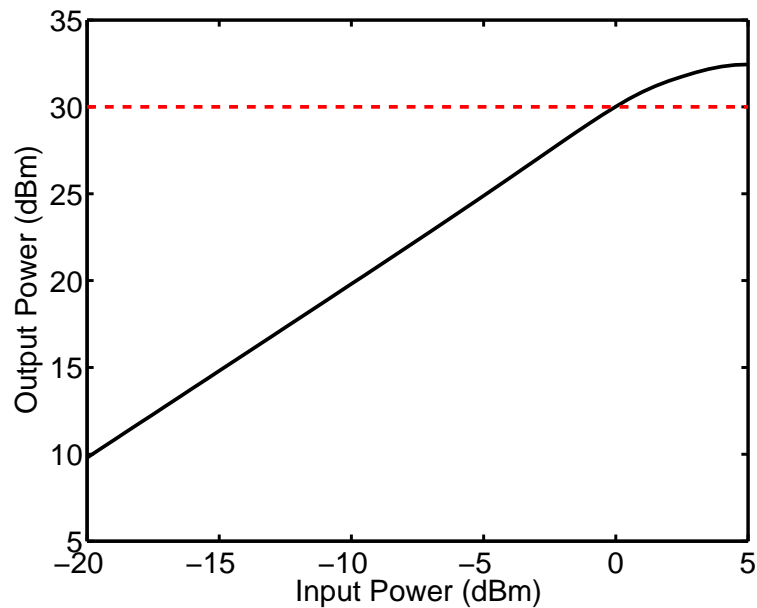


Figure 6.8.: Output power characteristic of the balanced amplifier of Fig. 6.7.

output ports respectively. This cancellation is caused by destructive superposition of the opposite phased signals. This type of amplifiers have been used widely in microwave applications since they allow for implementations of broadband transmitters with enhanced isolation and stability characteristics. Using identical fairly linear amplifier modules results in an overall output power which is twice the power of the single stages. In this work, the power amplifiers  $PA_1$ ,  $PA_2$  were described by behavioral models. Operating at 1.95 GHz they offer saturated power levels of 30 dBm with a moderate gain compression of 1 dB. Return loss and reverse isolation levels of 20 dB are considered. The linearity of the amplifiers is determined by their output referred third order intercept point which is set to 45 dBm. Assuming such performance for the individual amplifiers results in an output power characteristic of the transmitter as indicated in Fig. 6.8. Linear amplification with a gain of

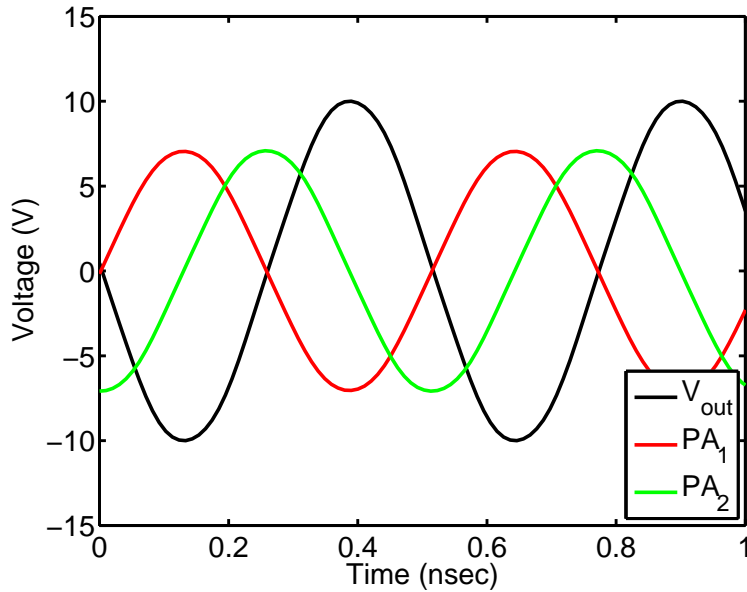


Figure 6.9.: Voltage waveforms at the output stages of the balanced amplifier module. Input power of  $P_{in}=0$  dBm is assumed at the frequency of 1.95 GHz.

30 dB is achieved up to approximately 1 W of RF power. At higher output power levels the amplifier module operates in saturation. The voltage waveforms of the amplifier module at the limit of linear operation are given in Fig. 6.9. As is readily seen, the output signals of the amplifiers  $PA_1$  and  $PA_2$  have a relative phase difference of  $90^\circ$ . This offset is finally corrected at the second branch-line coupler. The obtained waveforms have a nearly perfect sinusoidal shape indicating an operation with minor nonlinear effects. At this point it should be mentioned that such an approach is disadvantageous in terms of circuit dimensions and component count. Nevertheless, by using the previously implemented techniques circuit dimensions can be reduced significantly and a frequency agile behavior is obtained. The typically observed narrowband performance could be obtained for different operating communication bands by using tunable branch-line couplers.

Proper operation in communication devices implies investigation with modulated signals. Criteria concerning signal quality such as the error vector magnitude (EVM) and the spectral purity of the signal based on its adjacent channel leakage ratio (ACLR) have to be quantified. These specifications have been established by international standardization bodies, e.g. ETSI, as presented previously. The obtained output spectra at different operating power levels are given in Fig. 6.10 and Fig. 6.11. From the obtained simulation data it is seen that such a transmitter module would easily comply with the given specifications, since an ACLR of approximately 40 dB is resulting even for input power levels up to 0 dBm. At this

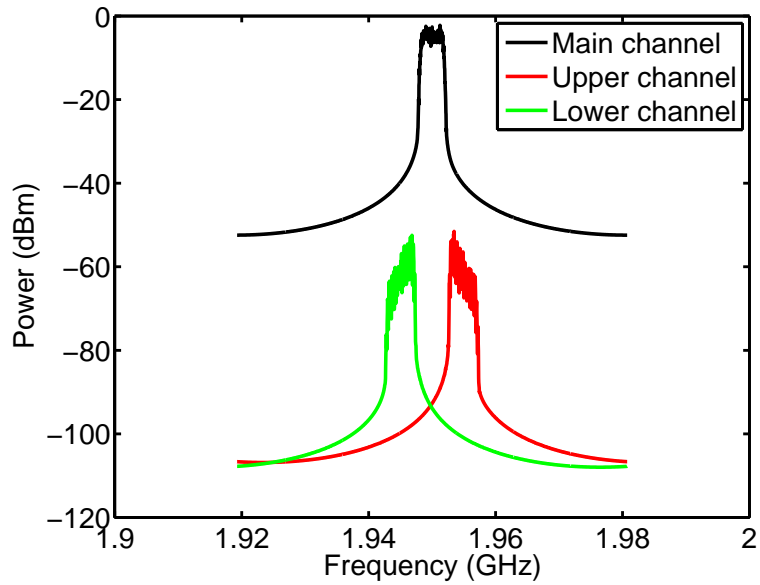


Figure 6.10.: Output spectrum for WCDMA signal with  $P_{in} = -10$  dBm and its adjacent channel spectral components.

operating RF output power of 1 W an EVM value of 7% is obtained, which is well below the specified limit.

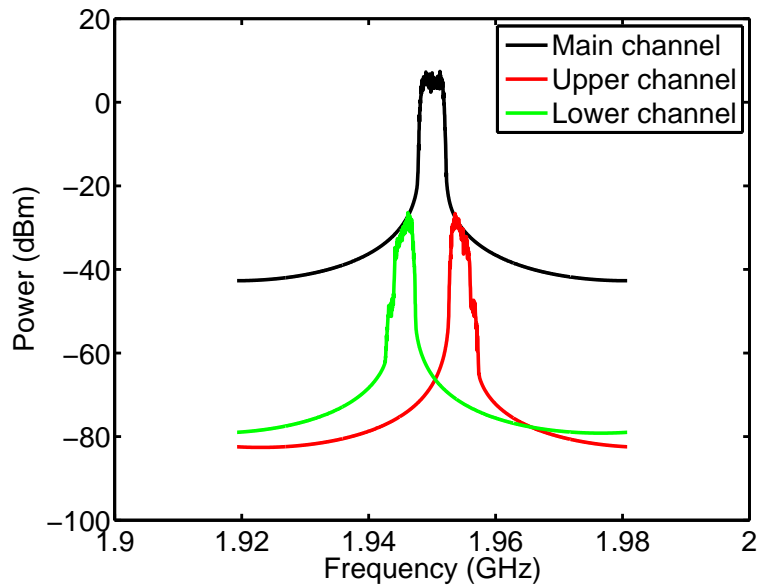


Figure 6.11.: Output spectrum for WCDMA signal with  $P_{in} = 0$  dBm and its adjacent channel spectral components.

### 6.3. Reconfigurable Amplifier

Based on the balanced amplifier topology, as discussed in the previous section, a modified version is obtained by substituting the branch-line couplers with the equivalent reduced size frequency agile branch-line couplers of Section 5.6. The only modification is the addition of one common bias voltage, as indicated in Fig. 6.12. This voltage was set to 5 V in order to establish the proper resonance frequency for the tunable couplers. Overall circuit dimensions are reduced by 50 % according to the shrinkage of the passive coupler structures. One noticeable effect is the lowpass filtering, which is performed by the hybrid couplers and is witnessed in Fig. 6.13 in terms of a roll-off effect in the transmission parameter. Both branch-line couplers attenuate the high frequency components of the incoming signal resulting in an overall attenuation of approximately 50 dB at the second harmonic. This behavior is especially important for suppression of higher order harmonics, which could appear by the used nonlinear circuits in this amplifier topology. For the first coupler circuit nonlinearities can be neglected since the expected maximum input power level is around 0 dBm. Amplification takes place at the output of the power amplifiers resulting in much higher input power levels for the second branch-line coupler. Harmonics which may occur at the power amplifier outputs will pass through the coupler stage which performs a lowpass filtering. At the target operating frequency of 1.95 GHz an attenuation of approximately 1.8 dB is resulting as a consequence of the additional losses introduced by the tunable couplers. This penalty in terms of insertion loss is a direct consequence of the moderate quality factors of the tunable passive elements.

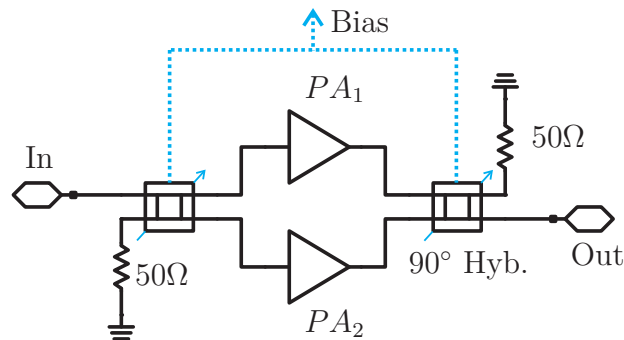


Figure 6.12.: Reconfigurable balanced power amplifier topology with tunable branch-line couplers.

The overall output characteristic of the reconfigurable amplifier module is given in Fig. 6.14. Linear operation is achieved up to input power levels of 0 dBm, while the increased insertion loss of the couplers results in reduced output power levels. One further issue that is worth mentioning concerns the observed voltage forms at the amplifier stages. As depicted in Fig. 6.15, significant deviations occur from the



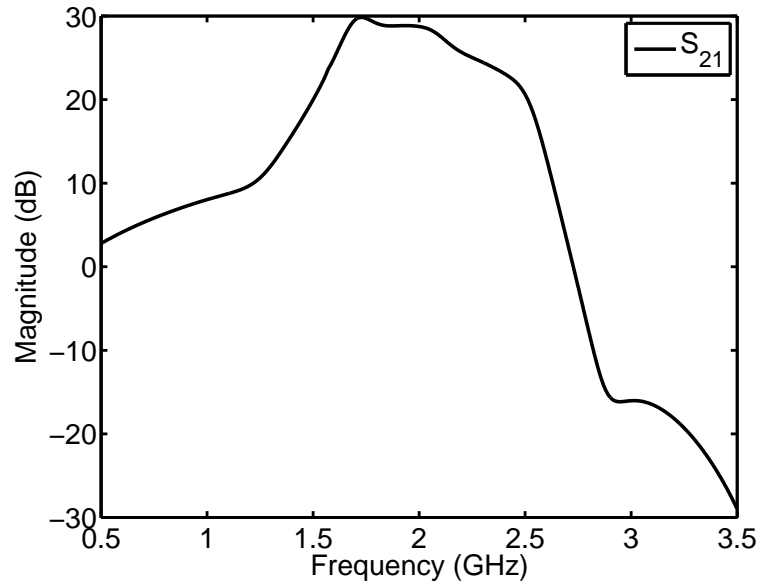


Figure 6.13.: Gain characteristic of tunable balanced amplifier module.

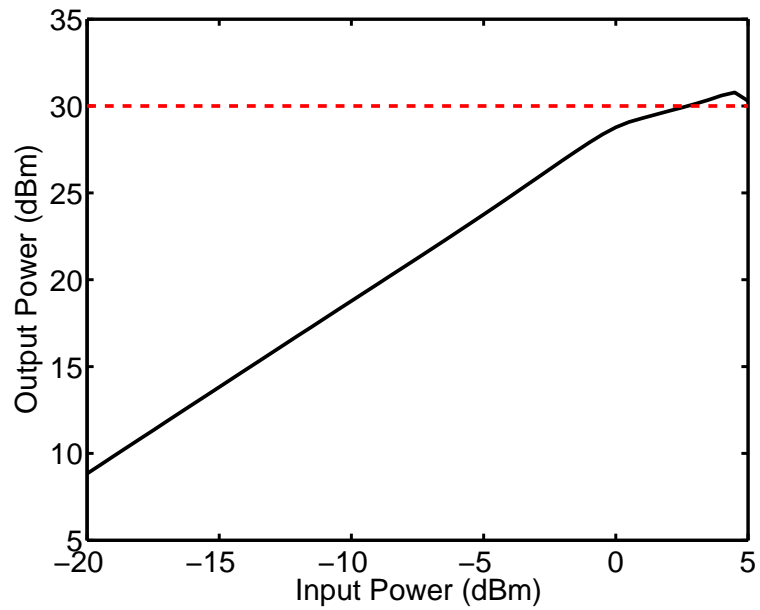


Figure 6.14.: Output power characteristic of the tunable balanced amplifier at an operating frequency of 1.95 GHz.

expected sinusoidal waveforms. Phase and gain imbalances in the tunable branch-line coupler structures result in voltage waveforms, which do not fulfill the desired shape. Thus care has to be taken in the design of the tunable coupler structures in

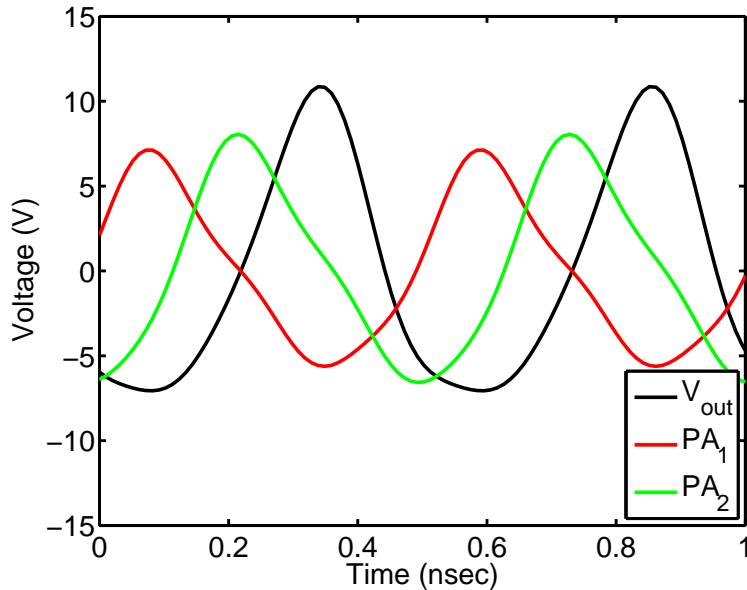


Figure 6.15.: Voltage waveforms at the output stages of the tunable balanced amplifier module. Input power of  $P_{in}=0$  dBm is assumed at the frequency of 1.95 GHz. The bias voltage is set to 5 V.

terms of symmetrical power coupling. Additionally to the mentioned imbalances, nonlinearities of the ferroelectric varactors itself are contributing also to a distorted voltage signal at the second coupler stage. These nonlinear effects become dominant for output power levels larger than 30 dBm, as indicated in Fig. 6.14.

A direct comparison between the previously discussed balanced amplifier and the proposed reconfigurable transmitter is ensured by using an identical simulation setup with modulated signals. A 3GPP WCDMA signal with a carrier frequency of 1.95 GHz is applied to the input terminal of the tunable balanced amplifier. The corresponding output spectra for the previously considered operating input power levels are given in Figs. 6.16 and 6.17. Comparing the mean power levels of the main channel and its adjacent channels reveals the achieved ACLR performance of the circuit. In both investigated cases the ACLR exceeds clearly the specified limit of 33 dB for a 5 MHz channel spacing. The simulated EVM was also well below the specified threshold of 17.5 %.

A first analysis of the resulting data leads to the conclusion, that the linearity requirements and the modulation quality is sufficient for such a circuit, at least considering operation with WCDMA signals. Nevertheless even for the discussed scenario it is evident, that in presence of the ferroelectric varactors some amount of distortion is taking place. The most obvious consequence of the nonlinearities contributed by the tuning elements are noticed by looking at the transient response of the voltage waveforms in Fig. 6.15. As discussed before, a series connection of

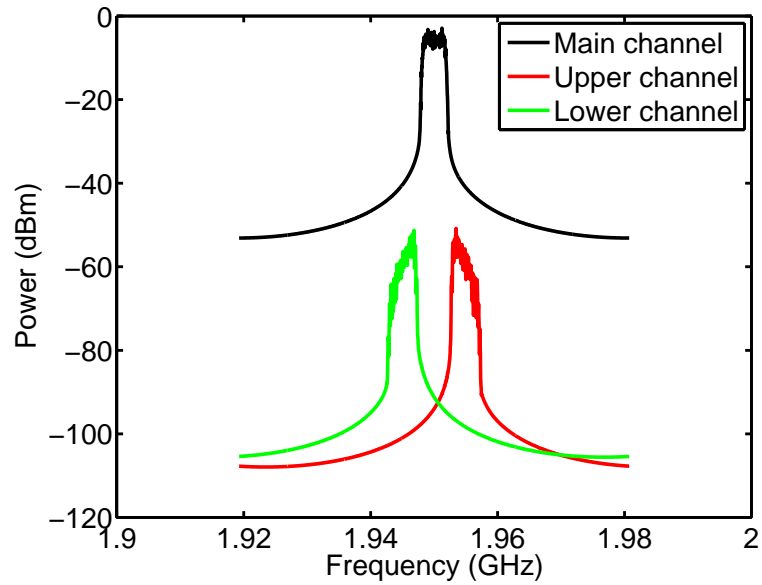


Figure 6.16.: Output spectrum for WCDMA signal with  $P_{in} = -10$  dBm and its adjacent channel spectral components for the proposed tunable transmitter topology.

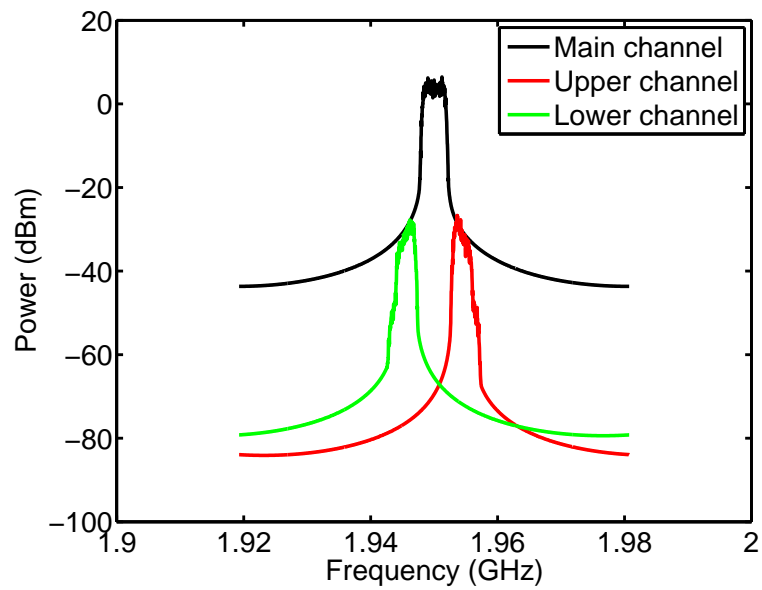


Figure 6.17.: Output spectrum for WCDMA signal with  $P_{in} = 0$  dBm and its adjacent channel spectral components for the proposed tunable transmitter topology.

individual varactors is a promising way to reduce the RF voltage swing across the tunable devices, thus improving the overall linearity of the circuit. As depicted in Fig. 6.18 and Fig. 6.19, cascading 3 varactors at each node of the second tunable branch-line coupler results in significant improvements in terms of linearity. The transient voltage waveforms have nearly perfect sinusoidal form indicating only some minor phase and amplitude errors in respect to each other. As a direct consequence the output power characteristic is improved as well. The obtained characteristic power curve indicates a regular operation of a power amplifier with moderate nonlinearities which cause a gain compression in the vicinity of its maximum output power. By a simple modification, namely cascading some varactors, the originally caused distortions are almost canceled out. The reduced nonlinear distortion is also noticed in the obtained output spectra of the amplifier module. The power leakage in their adjacent channels is clearly reduced, as depicted in Fig. 6.20 and Fig. 6.21.

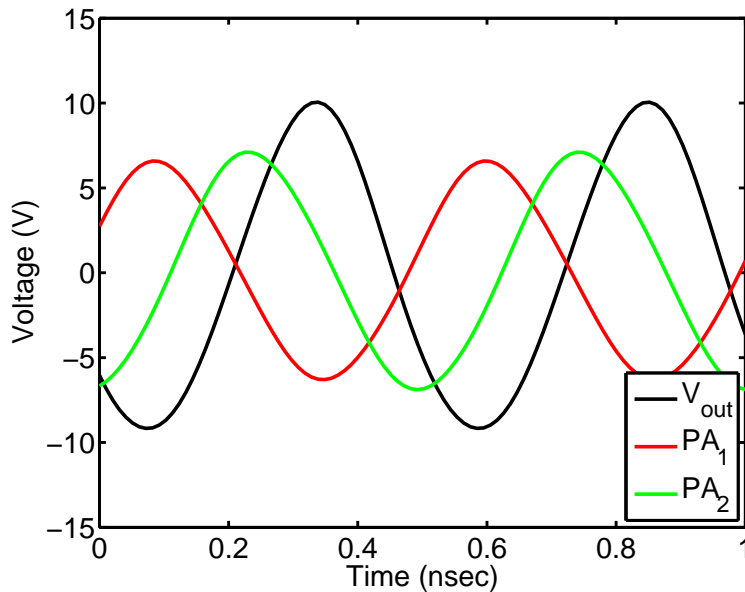


Figure 6.18.: Voltage waveforms for tunable balanced amplifier with a cascaded connection of 3 varactors for the second branch-line coupler. Input power of  $P_{in}=0$  dBm is assumed at the frequency of 1.95 GHz. The bias voltage is set to 5 V.

Recalling the picture of the ferroelectric varactor given in Fig. 2.2 supports the proposed solution. The active capacitor area of the 5 pF varactor is only a small portion of the overall chip. Processing several of those varactors in series would be feasible even without changing the chip size. The resulting high capacitance values which are needed in this case are implemented easily in a MIM structure. Customized solutions of reconfigurable microwave circuits including the voltage

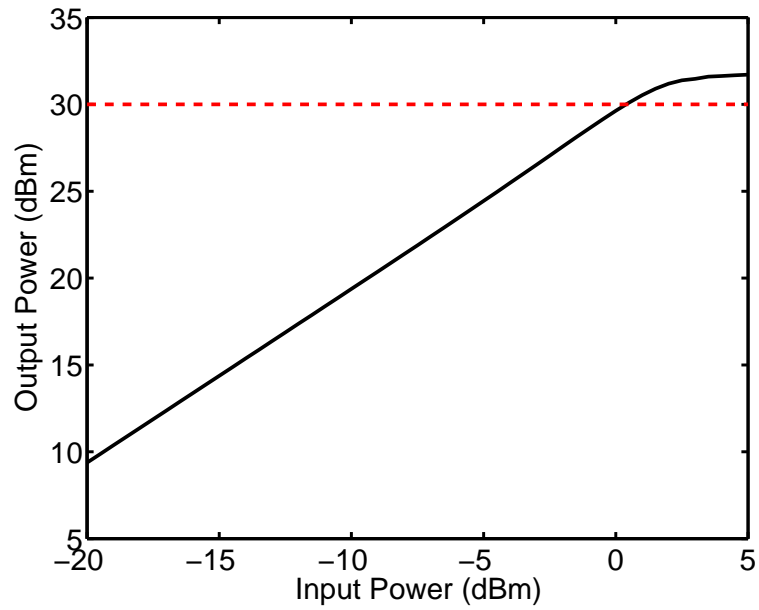


Figure 6.19.: Output power characteristic of the tunable balanced amplifier with 3 cascaded varactors at the second branch-line coupler.

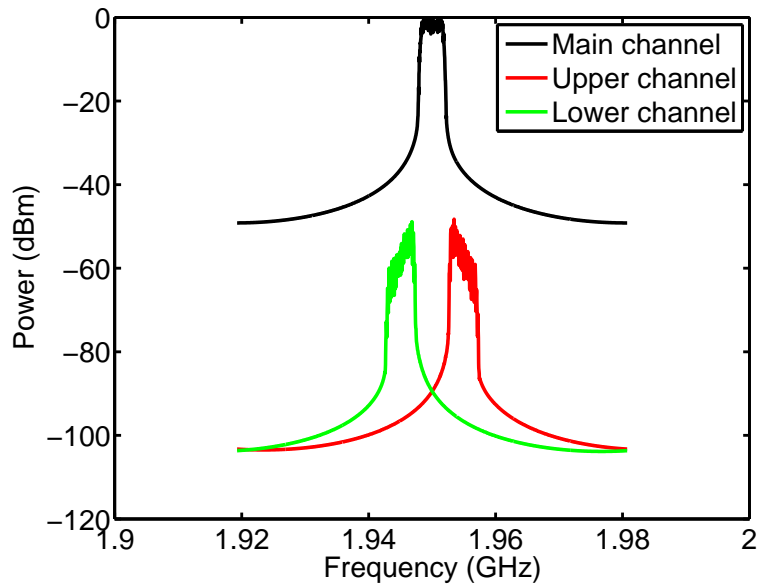


Figure 6.20.: Output spectrum for WCDMA signal with  $P_{in} = -10$  dBm and its adjacent channel spectral components for tunable balanced amplifier with 3 cascaded varactors at the second coupler stage.

handling circuits and tuning algorithms have been reported lately by industrial

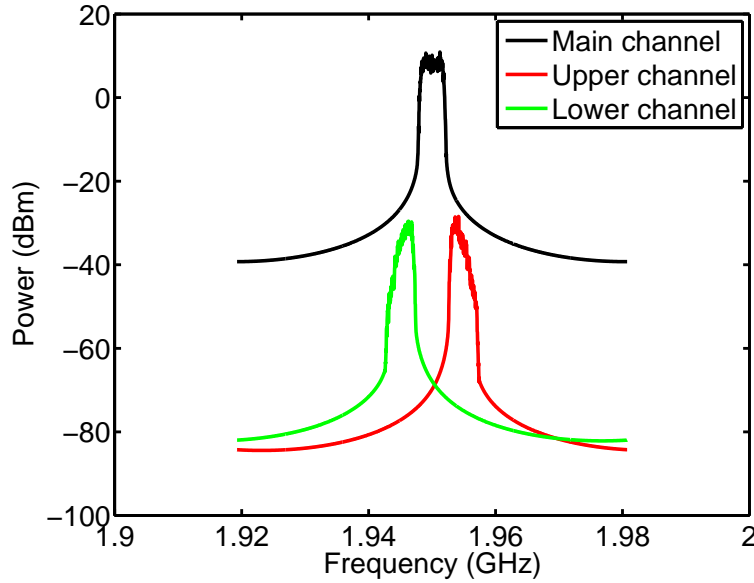


Figure 6.21.: Output spectrum for WCDMA signal with  $P_{in}=0$  dBm and its adjacent channel spectral components for tunable balanced amplifier with 3 cascaded varactors at the second coupler stage.

parties [112]. This technique appears to be very promising especially for thin-film varactors due to their high capacitance density, which allows for realizations of large capacitance values at considerably compact dimensions.

The frequency agile branch-line couplers play a key role in the proposed reconfigurable amplifier topology thus their individual behavior under operation with modulated signals should be investigated as well. By using the measurement setup of Fig. 6.5, a WCDMA modulated signal was applied to port 1 of the tunable branch-line coupler prototype and the corresponding power spectra at the output ports 2 and 3 were captured. The results for two different signal power levels of 5 dBm and 10 dBm are given in Fig. 6.22 and Fig. 6.23, respectively. As it is readily seen, the power coupling between both ports is absolutely symmetrical indicating only minor amplitude imbalances for the output paths. Additionally, it should be noted that there is no spectral regrowth witnessed for the adjacent channels. The resulting ACLR values are better than 35 dB. Nonlinear effects do not have a significant impact when operating at such power levels. A comparison between the simulated performance and the actual measured output spectrum for the branch-line prototype is given in Fig. 6.24. For the simulation setup a time period of 15 slots was used. During the measurement procedure an rms video bandwidth for the signal analyzer and an average factor of 100 was used. The dynamic range of the used measurement setup introduces limitations for power levels lower than -60 dBm. Furthermore, the limited simulation time causes an interpolation at the transition

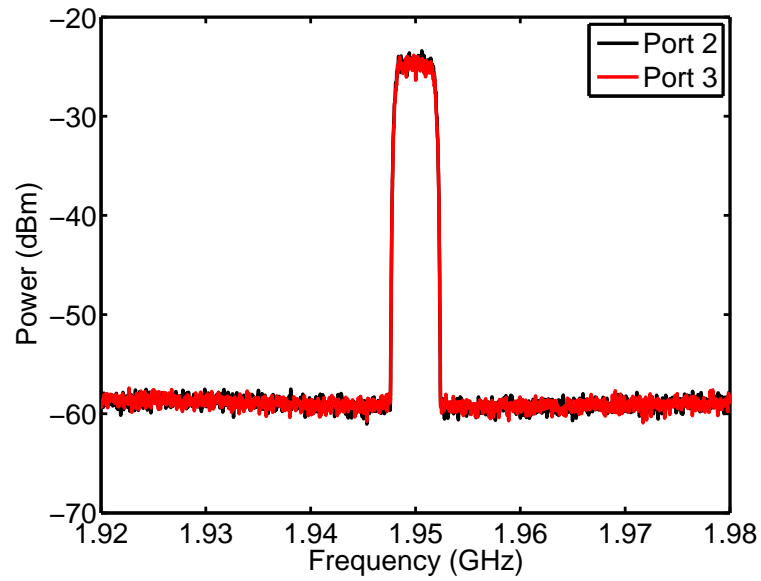


Figure 6.22.: Power spectra measured at the output ports of the tunable branch-line prototype board operating at a bias voltage of 7 V. The modulated input signal was set to a power of 5 dBm.

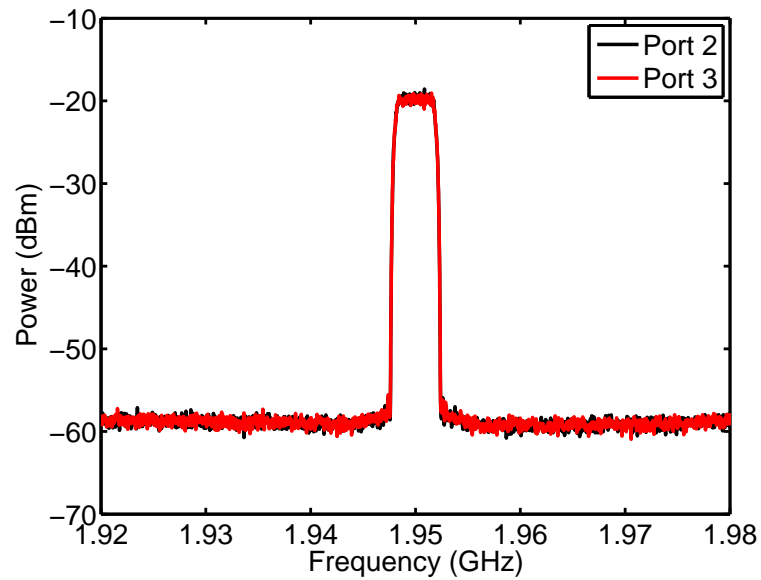


Figure 6.23.: Power spectra measured at the output ports of the tunable branch-line prototype board operating at a bias voltage of 7 V. The modulated input signal was set to a power of 10 dBm.

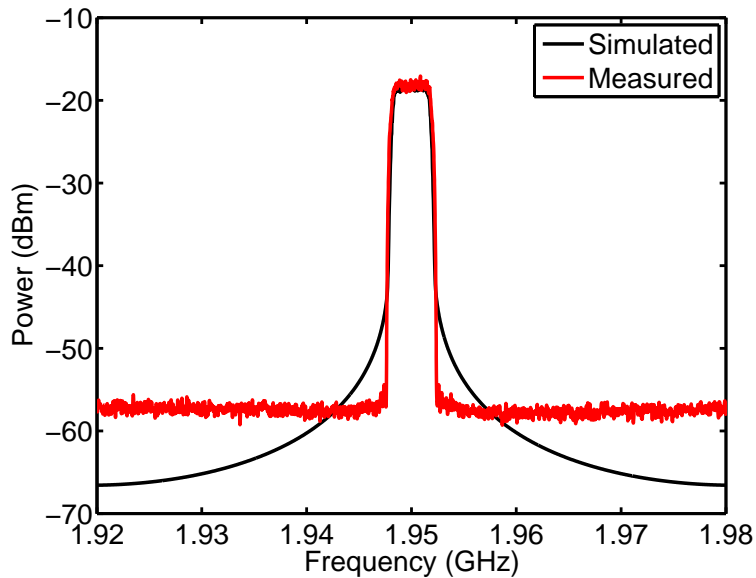


Figure 6.24.: Measured and simulated power spectra at port 2 of the tunable branch-line prototype board operating at a bias voltage of 7 V. The modulated input signal was set to a power of 10 dBm.

between the main channel and the adjacent ones. Nevertheless for the resulting channel power fairly good agreement is obtained thus proving the suitability of the simulation methodology. The implemented microwave circuits deliver reliable results for all kind of simulations, like harmonic balance, envelope, and transient analysis, thus all related system aspects for operation in a wireless communication environment can be investigated.

## 6.4. Bias Circuitry

So far voltage management concepts and the corresponding circuitry for producing the desired tuning voltages have not been taken into account. Since the target application is the operation in handheld devices for mobile communications the power consumption and the voltage handling are important issues. For the investigated ferroelectric varactors the tuning is achieved without power consumption since no DC current is involved. Only leakage currents for the varactors would result in DC power consumption, which would have a direct impact on the battery life time of the handheld device. A much more challenging task is the creation of the tuning voltages, since for handheld devices the only available energy source are batteries with low voltages, e.g. in the range of 3.5 V. Additional circuits such as charge pump topologies are needed to transform the low battery voltage to the desired maximum tuning voltage of approximately 20 V. One widely used charge pump



topology is the so called Dickson pump [113] and is depicted in Fig. 6.25.

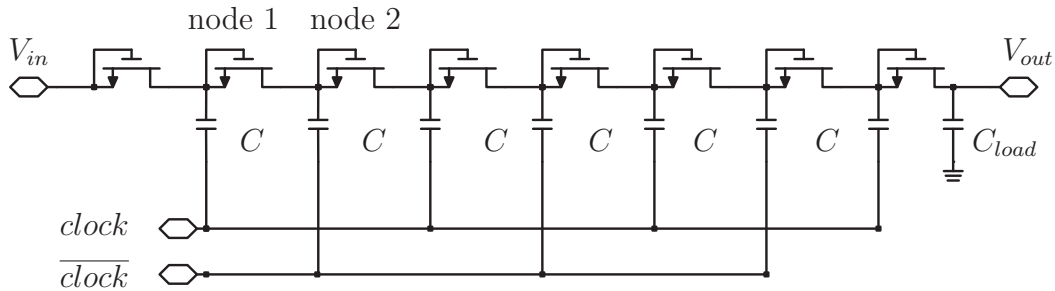


Figure 6.25.: Dickson charge pump with NMOS transistor stages.

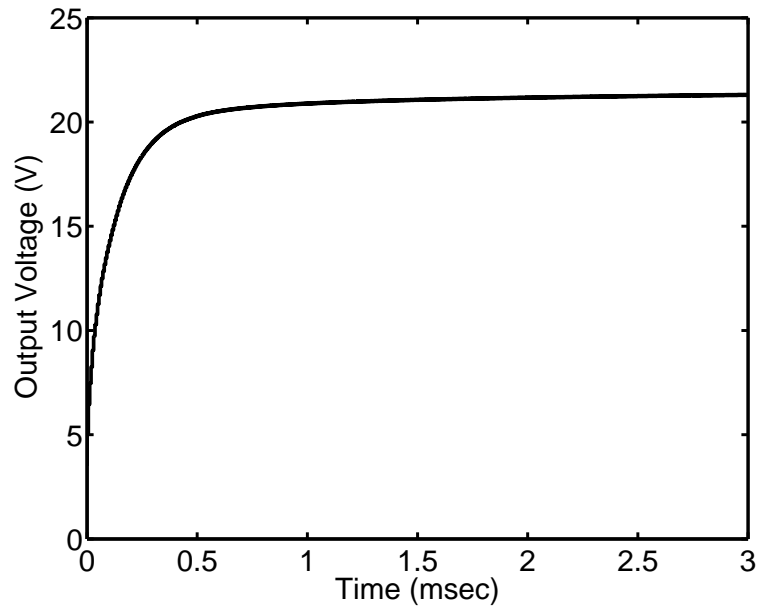


Figure 6.26.: Transient response of a charge pump with seven stages and a load capacitance of 10 pF.

The circuit operates like a voltage multiplier by pumping charge along the transistor stages which are configured to operate as diodes. One pulsed clock signal of amplitude  $V_{ref}$  and its complementary are used to control the propagation of the signal from the input to the output. When *clock* is switched to 'low' the first diode starts to conduct and presents a voltage of  $V_{in} - V_d$  to the first output stage, where  $V_d$  is the forward bias voltage of the diode. At the point where *clock* is set to 'high', the voltage at the output of node 1 becomes  $V_{in} + (V_{ref} - V_d)$  and the second diode starts to conduct providing a voltage of  $V_{in} + (V_{ref} - V_d) - U_d$ . When *clock* is low again the voltage at node 2 becomes  $V_{in} + 2(V_{ref} - V_d)$ . Repeating this logic for the following stages leads to an overall expression for the output voltage of

$$V_{out} = V_{in} + N(V_{ref} - V_d) - V_d. \quad (6.5)$$

Assuming an input voltage of 3.5 V, which is typical for batteries of handheld devices, and a clock pulse with amplitude of  $V_{ref}=3$  V would result in  $N=7$  charge pump cells in order to transform the input voltage to a value of approximately 20 V. The transient response for such a network is given in Fig. 6.26. The output signal reaches the desired value of 20 V in less than 1 msec, which should be sufficient for tuning operations. Considering an operation with such high voltages calls for semiconductor elements which are capable of dealing with them. High voltage CMOS processes have been developed for a variety of industrial and automotive applications and allow for integration of high voltage electronics along with the regular digital control blocks. Established semiconductor vendors such as Austria Microsystems offer a variety of adequate processes, e.g. 0.8  $\mu$ m CMOS process for voltages up to 50 V. Simple 'look-up' tables could be used for the implemented microwave circuits since only one bias signal is needed and thus there is no need for sophisticated tuning or control algorithms. Each setting of the bias voltage would result in a different operating frequency for the circuit. Previously defined operating states could be mapped to individual control signals, which in turn would be stored in simple memory devices.

## 7. Conclusion and Outlook

The objective of the present work is to demonstrate the potential of tunable passive components, such as ferroelectric or MEMS varactors, in designing frequency agile and reconfigurable microwave circuits. Complete design methodologies are presented for frequency agile filters based on lumped components. The implemented lowpass and notch filter exhibit tuning ranges of more than 30%. Additionally a modified distributed combline filter with an attenuation pole in the lower stopband has been implemented. The insertion- and return loss in the passband are better than 2.8 dB and 20 dB for all operating bias conditions. The filter passband can be tuned continuously from 1.8 GHz to 2 GHz enabling multi-band operation. Furthermore, a novel approach for designing reduced size frequency agile power dividers and couplers is presented. Besides a significant size reduction of 50%, a tuning range of more than 20% is achieved for this type of circuits. Excellent amplitude and phase relations are retained at all operating conditions. As a consequence the divider and coupler operation is fulfilled at discrete frequencies which can be tuned continuously. All proposed frequency agile microwave circuits were implemented successfully as prototype boards and characterized for their small and large signal operation. Finally an example of a reconfigurable transmitter topology is discussed on the basis of the implemented tunable branch-line couplers. The operation with real-world WCDMA modulated signals is investigated and verified by simulation and measurement, respectively.

So far the performance of the tunable passive components itself has been investigated and their operation in reconfigurable microwave circuits has been demonstrated successfully. The operation with modulated signals is demonstrated as well. A complete investigation at system level can be performed since equivalent varactor models can be integrated in commercially available simulator tools. As has been briefly demonstrated in Chapter 6 frequency agile circuits can be included in complete system solutions with other front-end modules, e.g. power amplifiers, and operate as reconfigurable front-end blocks. Future work should focus on complete system solutions and therefore needs to integrate tunable microwave circuits, like filters, couplers, etc. with active components, such as power amplifiers and mixers, in a complete front-end architecture. Modern packaging technologies such as the use of multilayer LTCC modules are promising candidates for implementing such prototype systems.

# A. Transmission Matrix and Transformations

The transmission matrix, also called  $ABCD$  matrix, is an elegant representation of two-port networks. It describes the dependence of voltages and currents associated with a two-port network, as they are depicted in Fig. A.1.

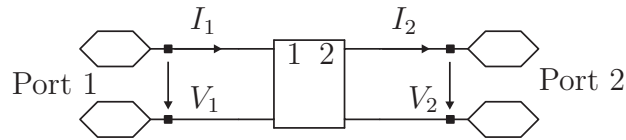


Figure A.1.: Schematic of two-port network.

$$V_1 = AV_2 + BI_2 \quad (\text{A.1})$$

$$I_1 = CV_2 + DI_2 \quad (\text{A.2})$$

In a matrix representation these formulas can be expressed as

$$\begin{bmatrix} V_1 \\ I_1 \end{bmatrix} = \begin{bmatrix} A & B \\ C & D \end{bmatrix} \cdot \begin{bmatrix} V_2 \\ I_2 \end{bmatrix}. \quad (\text{A.3})$$

The advantage of  $ABCD$  matrices is that a cascaded topology of several two-port networks can be described just by multiplying their individual transmission matrices. This representation is powerful since most of the microwave circuits rely on the combination of two-port elements.

Once the  $ABCD$  matrix of a structure has been calculated it can be easily transformed into the corresponding scattering parameter matrix which has the following form

$$S = \begin{bmatrix} S_{11} & S_{12} \\ S_{21} & S_{22} \end{bmatrix}. \quad (\text{A.4})$$

The individual elements of this matrix can be calculated as

$$S_{11} = \frac{A + B/Z_0 - CZ_0 - D}{A + B/Z_0 + CZ_0 + D} \quad (\text{A.5})$$

$$S_{12} = \frac{2(AD - BC)}{A + B/Z_0 + CZ_0 + D} \quad (\text{A.6})$$

$$S_{21} = \frac{2}{A + B/Z_0 + CZ_0 + D} \quad (\text{A.7})$$

$$S_{22} = \frac{-A + B/Z_0 - CZ_0 + D}{A + B/Z_0 + CZ_0 + D}, \quad (\text{A.8})$$

where  $Z_0$  is the reference impedance of the system. Some of the most common two-port networks used in microwave circuit design and their transmission matrices are summarized in the following figure.

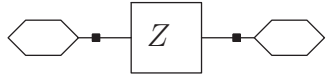
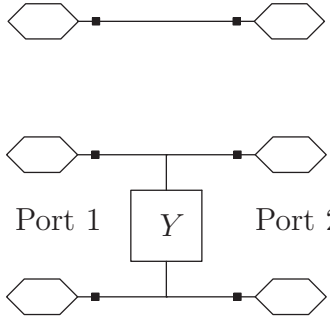
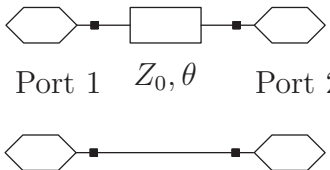
Two-port circuit	$ABCD$ matrix
 <p>Port 1                      Port 2</p>	$\begin{bmatrix} 1 & Z \\ 0 & 1 \end{bmatrix}$
 <p>Port 1                      Port 2</p>	$\begin{bmatrix} 1 & 0 \\ Y & 1 \end{bmatrix}$
 <p>Port 1      <math>Z_0, \theta</math>      Port 2</p>	$\begin{bmatrix} \cos(\theta) & jZ_0 \sin(\theta) \\ (j/Z_0) \sin(\theta) & \cos(\theta) \end{bmatrix}$

Figure A.2.:  $ABCD$  matrices of some useful two-port circuits.

In Fig. A.2,  $Z$ ,  $Y$  are the series impedance and shunt admittance respectively, while  $Z_0$ ,  $\theta$  are the characteristic impedance and electrical length of an arbitrary transmission line segment.

## B. Two-Tone Measurement Setup

One widely used procedure to quantify the nonlinear effects, which are associated with a nonlinear circuit, is the two-tone test. The underlying principle is presented in Fig. B.1. Applying two individual sinusoidal tones at the input of a nonlinear circuit causes intermodulation products at its output. Among them the 3<sup>rd</sup> order intermodulation products are the most critical ones since they are allocated in the vicinity of the fundamental tones thus they can hardly be removed with a filtering process.

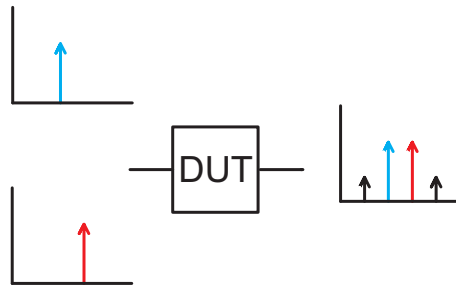


Figure B.1.: Nonlinear circuit response under two-tone excitation.

A typical two-tone measurement setup, as depicted in Fig. B.2, can be used to determine the linearity performance of such a circuit.

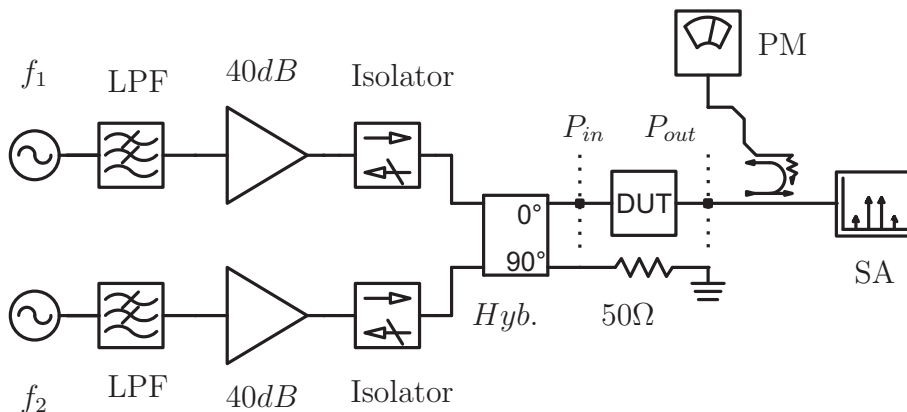


Figure B.2.: Schematic of two-tone measurement setup.

Two RF signal sources are used to produce the sinusoidal tones with individual frequencies  $f_1$  and  $f_2$ . Their output is lowpass filtered in order to cut off the spurious harmonic parts and then amplified by highly linear power amplifiers (PA). By connecting two isolators right after the PA modules reverse intermodulation is avoided. The hybrid coupler is used to combine the two narrow spaced tones and feed them to the DUT's input port. The attenuation between the power amplifier modules and the DUT is corrected thus the absolute power level  $P_{in}$  is presented at the input port of the DUT. The output port is connected through a coupler to a power meter (PM) and a spectrum analyzer (SA) to capture the corrected output power and the intermodulation product levels, respectively.

For the experimental results in this work the setup of Fig. B.3 was used. Two R&S SMIQ signal generators, one FSEB spectrum analyzer, and one NRP power meter form the core measurement units. Additional passive elements such as isolators, combiners and power couplers are used according to the previous description.

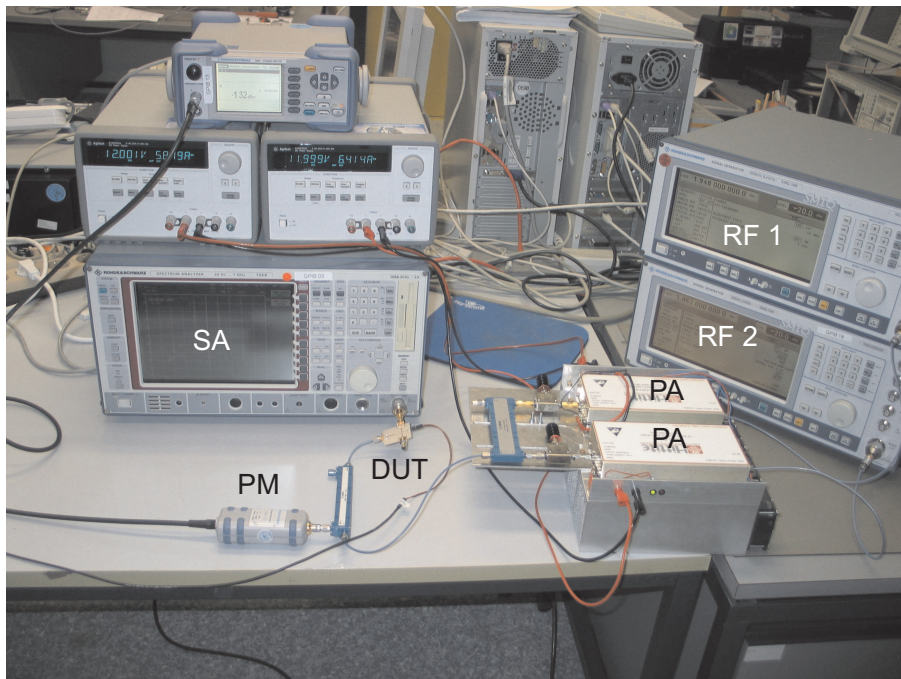


Figure B.3.: Measurement setup used for two-tone test.

The entire setup is interconnected via GPIB (General Purpose Interface Bus) and controlled through a PC and Agilent's VEE software. Using such a setup allows for accurate and repeatable measurements.

## C. List of Abbreviations

ACLR	Adjacent Channel Leakage Ratio
ADS	Advanced Design System
ASK	Amplitude Shift Keying
BST	Barium-Strontium-Titanate
CMOS	Complementary Metal Oxide Semiconductor
DC	Direct Current
DUT	Device Under Test
EDGE	Enhanced Data Rates for GSM Evolution
ESD	Electrostatic Discharge
ETSI	European Telecommunications Standards Institute
EVM	Error Vector Magnitude
FBAR	Film Bulk Acoustic Resonator
FSK	Frequency Shift Keying
GPIO	General Purpose Interface Bus
GSM	Global System for Mobile Communications
LTCC	Low Temperature Co-fired Ceramic
LTE	Long Term Evolution
MEMS	Microelectromechanical System
MIM	Metal Insulator Metal
PA	Power Amplifier
PC	Personal Computer
PM	Power Meter
PSK	Phase Shift Keying
PZT	Lead Zirconate Titanate
QPSK	Quadrature Phase Shift Keying
RF	Radio Frequency
SA	Spectrum/Signal Analyzer
SAW	Surface Acoustic Wave
SDD	Symbolically Defined Device
SMA	Sub-Miniature A
SMD	Surface Mount Device
UMTS	Universal Mobile Telecommunication System
VNA	Vector Network Analyzer
WCDMA	Wideband Code Division Multiple Access



# Bibliography

- [1] R. Weigel, D. Morgan, J. Owens, A. Ballato, K. Lakin, K. Hashimoto, and C. Ruppel, "Microwave acoustic materials, devices, and applications," *IEEE Trans. Microwave Theory and Tech.*, vol. 50, no. 3, pp. 738–749, 2002.
- [2] Y. Lin, C. Liu, K. Li, and C. Chen, "Design of an LTCC tri-band transceiver module for GPRS mobile applications," *IEEE Trans. Microwave Theory and Tech.*, vol. 52, no. 12, pp. 2718–2724, 2004.
- [3] P. Hagn, A. Przadka, V. Gebhardt, and U. Bauernschmitt, "Ceramics: the platform for duplexers and frontend-modules," in *2002 IEEE Ultrasonics Symposium*, vol. 1, 2002, pp. 1–10.
- [4] C. Lai, Y. Hsu, and C. Chen, "Triple-mode Five-band Power Amplifier LTCC Module for WLAN/GPRS/WCDMA Applications," in *Proc. 36th European Microwave Conf.*, 2006, pp. 1486–1489.
- [5] A. Chernyakov, K. Markov, A. Kryshtopin, D. Orlenko, S. Royak, R. Kravchenko, A. Gordiyenko, T. Kerssenbrock, G. Sevskiy, and P. Heide, "Novel small-size LTCC-based WLAN frontend-modules with integrated power amplifiers," in *2004 IEEE MTT-S Int. Microwave Symp. Dig.*, vol. 2, 6–11 Jun. 2004, pp. 559–562.
- [6] S. Marksteiner, M. Handtmann, H. Timme, R. Aigner, R. Welzer, J. Portmann, U. Bauernschmitt, I. AG, and G. Munich, "A miniature BAW duplexer using flip-chip on LTCC," in *2003 IEEE Ultrasonics Symposium*, vol. 2, 5–8 Oct. 2003, pp. 1794–1797.
- [7] W. Heinrich, "The flip-chip approach for millimeter wave packaging," *IEEE Microwave Magazine*, vol. 6, no. 3, pp. 36–45, 2005.
- [8] G. Feiertag, H. Krüger, and C. Bauer, "Hard shells," EPCOS AG, Tech. Rep., January 2008.
- [9] U. Bauernschmitt, C. Block, P. Hagn, G. Kovacs, E. Leitschak, A. Przadka, and C. Ruppel, "Front-end solutions for world phones," EPCOS AG, Tech. Rep., October 2007.

- 
- [10] A. Abbaspour-Tamijani, L. Dussopt, and G. Rebeiz, "Miniature and tunable filters using MEMS capacitors," *IEEE Trans. Microwave Theory and Tech.*, vol. 51, no. 7, pp. 1878–1885, 2003.
- [11] M. Rahman, K. Shamsaifar, P. Inc, and M. Columbia, "Electronically tunable LTCC based multi-layer filter for mobile handset application," in *2003 IEEE MTT-S Int. Microwave Symp. Dig.*, vol. 3, 8–13 Jun. 2003, pp. 1767–1770.
- [12] J. Nath, D. Ghosh, J. Maria, A. Kingon, W. Fathelbab, P. Franzon, and M. Steer, "An electronically tunable microstrip bandpass filter using thin-film Barium-Strontium-Titanate (BST) varactors," *IEEE Trans. Microwave Theory and Tech.*, vol. 53, no. 9, pp. 2707–2712, 2005.
- [13] Y. Lu, L. Katehi, and D. Peroulis, "High-power MEMS varactors and impedance tuners for millimeter-wave applications," *IEEE Trans. Microwave Theory and Tech.*, vol. 53, no. 11, pp. 3672–3678, 2005.
- [14] P. Scheele, F. Goelden, A. Giere, S. Mueller, and R. Jakoby, "Continuously tunable impedance matching network using ferroelectric varactors," in *2005 IEEE MTT-S Int. Microwave Symp. Dig.*, 12–17 Jun. 2005, pp. 603–606.
- [15] M. Schmidt, E. Lourandakis, A. Leidl, S. Seitz, and R. Weigel, "A Comparison of Tunable Ferroelectric  $\Pi$  and T-Matching Networks," in *Proc. 37th European Microwave Conf.*, 9–12 Oct. 2007, pp. 98–101.
- [16] Q. Shen and N. Barker, "Distributed MEMS Tunable Matching Network Using Minimal-Contact RF-MEMS Varactors," *IEEE Trans. Microwave Theory and Tech.*, vol. 54, no. 6, pp. 2646–2658, June 2006.
- [17] J. Serraiocco, P. Hansen, T. Taylor, J. Speck, and R. York, "Compact Distributed Phase Shifters at X-Band Using BST," *Integrated Ferroelectrics*, vol. 56, no. 1, pp. 1087–1095, 2003.
- [18] D. Kim, S.-S. Je, J. Kenney, and P. Marry, "Design of ferroelectric phase shifters for minimum performance variation over temperature," in *2004 IEEE MTT-S Int. Microwave Symp. Dig.*, vol. 1, 6–11 Jun. 2004, pp. 257–260.
- [19] W. Fathelbab and M. Steer, "New classes of miniaturized planar Marchand baluns," *IEEE Trans. Microwave Theory and Tech.*, vol. 53, no. 4, pp. 1211–1220, 2005.
- [20] Y. Zheng, A. Giere, and R. Jakoby, "A Compact Antenna with Two Independently Tunable Frequency Bands," in *2008 IEEE AP-S International Symposium Dig.*, 5–12 Jul. 2008.

- [21] R. Jackson and R. Ramadoss, "A MEMS-based electrostatically tunable circular microstrip patch antenna," *JOURNAL OF MICROMECHANICS AND MICROENGINEERING*, vol. 17, no. 1, p. 1, 2007.
- [22] M. Al-Ahmad, C. Loyez, N. Rolland, and P. Rolland, "Wide BST-based tuning of voltage controlled oscillator," in *2006 Asia-Pacific Microwave Conference*, 12–15 Dec. 2006, pp. 468–471.
- [23] A. Victor, J. Nath, D. Ghosh, B. Boyette, J.-P. Maria, M. Steer, A. Kingon, and G. Stauf, "A voltage controlled oscillator using barium strontium titanate (BST) thin film varactor," in *2004 IEEE Radio and Wireless Conference*, 19–22 Sept. 2004, pp. 91–94.
- [24] H. Katta, H. Kurioka, and Y. Yashima, "Tunable Power Amplifier Using Thin-Film BST Capacitors," in *2006 IEEE MTT-S Int. Microwave Symp. Dig.*, 11–16 Jun. 2006, pp. 564–567.
- [25] W. Neo, Y. Lin, X. Liu, L. De Vreede, L. Larson, M. Spirito, M. Pelk, K. Buisman, A. Akhnoukh, A. De Graauw *et al.*, "Adaptive Multi-Band Multi-Mode Power Amplifier Using Integrated Varactor-Based Tunable Matching Networks," *IEEE Journal of Solid-State Circuits*, vol. 41, no. 9, pp. 2166–2176, 2006.
- [26] A. Tombak, "A Ferroelectric-Capacitor-Based Tunable Matching Network for Quad-Band Cellular Power Amplifiers," *IEEE Trans. Microwave Theory and Tech.*, vol. 55, no. 2, pp. 370–375, 2007.
- [27] G. Fischer, "Next-Generation Base Station Radio Frequency Architecture," *Bell Labs Technical Journal*, vol. 12, no. 2, pp. 3–18, 2007.
- [28] J. Valasek, "Piezo-Electric and Allied Phenomena in Rochelle Salt," *Physical Review*, vol. 17, no. 4, pp. 475–481, 1921.
- [29] H. Kohlstedt, Y. Mustafa, A. Gerber, A. Petraru, M. Fitsilis, R. Meyer, U. Böttger, and R. Waser, "Current status and challenges of ferroelectric memory devices," *Microelectronic Engineering*, vol. 80, pp. 296–304, 2005.
- [30] H. Itoh, K. Kashihara, T. Okudaira, Y. Tsunemine, Y. Ohno, T. Nishimura, T. Horikawa, and T. Shibano, "Integration of BST thin film for DRAM fabrication," *Integrated Ferroelectrics*, vol. 11, no. 1, pp. 101–109, 1995.
- [31] D. Kotecki, J. Baniecki, H. Shen, R. Laibowitz, K. Saenger, J. Lian, T. Shaw, S. Athavale, C. Cabral, P. Duncombe, M. Gutsche, G. Kunkel, Y.-J. Park, Y.-Y. Wang, and R. Wise, "(ba,sr)tio<sub>3</sub> dielectrics for future stacked capacitor dram," *IBM Journal of Research and Development*, vol. 43, no. 3, pp. 367–382, 1999.

- 
- [32] D. Thompson, O. Tantot, H. Jallageas, G. Ponchak, M. Tentzeris, and J. Pappolymerou, "Characterization of liquid crystal polymer (LCP) material and transmission lines on LCP substrates from 30 to 110 GHz," *IEEE Trans. Microwave Theory and Tech.*, vol. 52, no. 4, pp. 1343–1352, 2004.
- [33] S. Mueller, A. Penirschke, C. Damm, P. Scheele, M. Wittek, C. Weil, and R. Jakoby, "Broad-band microwave characterization of liquid crystals using a temperature-controlled coaxial transmission line," *IEEE Trans. Microwave Theory and Tech.*, vol. 53, no. 6 Part 2, pp. 1937–1945, 2005.
- [34] S. Mueller, C. Felber, P. Scheele, M. Wittek, C. Hock, and R. Jakoby, "Passive Tunable Liquid Crystal Finline Phase Shifter for Millimeterwaves," *Proc. 35th European Microwave Conf.*, vol. 1, 2005.
- [35] R. Marin, A. Moessinger, F. Goelden, S. Mueller, and R. Jakoby, "77 GHz Reconfigurable Reflectarray with Nematic Liquid Crystal," *Proc. 2nd European Conference on Antennas and Propagation*, pp. 1–5, 2007.
- [36] O. Vendik, L. Ter-Martirosyan, and S. Zubko, "Microwave losses in incipient ferroelectrics as functions of the temperature and the biasing field," *Journal of Applied Physics*, vol. 84, p. 993, 1998.
- [37] A. Vorobiev, P. Rundqvist, K. Khamchane, and S. Gevorgian, "Microwave Loss Mechanisms in  $\text{Ba}_{0.25}\text{Sr}_{0.75}\text{TiO}_3$  Thin Film Varactors," *Journal of Applied Physics*, vol. 96, no. 8, pp. 4642–4649, 2004.
- [38] M. Lines and G. A.M., *Principles and Applications of Ferroelectrics and Related Materials*, ser. Oxford Classic Texts. Oxford University Press Inc., New York, 1977.
- [39] D. Kil, J. Park, J. Lee, J. Yoon, Y. Yu, J. Roh, C. Kim, and J. Hwang, "Electrical properties of MOCVD BST thin films annealed by rapid thermal annealing process," *Integrated Ferroelectrics*, vol. 33, no. 1, pp. 291–301, 2001.
- [40] J. Lu, S. Schmidt, D. Boesch, N. Pervez, R. York, and S. Stemmer, "Low-loss tunable capacitors fabricated directly on gold bottom electrodes," *Applied Physics Letters*, vol. 88, p. 112905, 2006.
- [41] P. Rundqvist, T. Liljenfors, A. Vorobiev, E. Olsson, and S. Gevorgian, "The effect of SiO, Pt, and Pt/ Au templates on the microstructure and permittivity of BaSrTiO films," *Journal of Applied Physics*, vol. 100, pp. 114–116, 2006.
- [42] H. Schlosser and M. Drougard, "Surface Layers on Barium Titanate Single Crystals above the Curie Point," *Journal of Applied Physics*, vol. 32, p. 1227, 2004.

- 
- [43] S. Schmitz and H. Schroeder, "Leakage Current Measurements of STO and BST Thin Films Interpreted by the "Dead" Layer Model," *Integrated Ferroelectrics*, vol. 46, no. 1, pp. 233–242, 2002.
- [44] O. Vendik and L. Ter-Martirosyan, "Influence of charged defects on the dielectric response of incipient ferroelectrics," *Journal of Applied Physics*, vol. 87, p. 1435, 2000.
- [45] X. Li, B. Chen, H. Jing, H. Lu, B. Zhao, Z. Mai, and Q. Jia, "Experimental evidence of the 'dead layer' at Pt/ BaTiO interface," *Applied Physics Letters*, vol. 87, p. 222905, 2005.
- [46] D. Chase, L. Chen, and R. York, "Modeling the Capacitive Nonlinearity in Thin-Film BST Varactors," *IEEE Trans. Microwave Theory and Tech.*, vol. 53, no. 10, pp. 3215–3220, 2005.
- [47] M. Schmidt, "Abstimmbare Anpassnetzwerke auf Basis ferroelektrischer Varaktoren für Mobilfunkanwendungen," Ph.D. Dissertation, Technische Fakultät der Universität Erlangen-Nürnberg, 2007.
- [48] *Advanced impedance measurement capability of the RF I-V method compared to the network analysis method*, Agilent Technologies, July, 26 2001, Application Note 1369–2.
- [49] S. Wartenberg, *RF Measurements of Die and Packages*. Artech House, 2002.
- [50] B. Strukov and A. Levanyuk, *Ferroelectric Phenomena in Crystals*. Berlin, Springer, 1998.
- [51] S. Tappe, U. Bottger, and R. Waser, "Electrostrictive resonances in (Ba<sub>0.7</sub>Sr<sub>0.3</sub>) TiO<sub>3</sub> thin films at microwave frequencies," *Applied Physics Letters*, vol. 85, pp. 624–626, 2004.
- [52] S. Gevorgian, A. Vorobiev, and T. Lewin, "DC Field and Temperature Dependent Acoustic Resonances in Parallel-Plate Capacitors Based on SrTiO<sub>3</sub> and Ba<sub>0.25</sub>Sr<sub>0.75</sub>TiO<sub>3</sub> Films: Experiment and Modeling," *Journal of Applied Physics*, vol. 99, p. 124112, 2006.
- [53] K. Lakin, "Fundamental Properties of Thin Film Resonators," in *Proceedings of the 45th Annual Symposium on Frequency Control*, May 1991, pp. 201–206.
- [54] —, "Modeling of Thin Film Resonators and Filters," in *1992 IEEE MTT-S Int. Microwave Symp. Dig.*, vol. 1, June 1992, pp. 149–152.

- 
- [55] X. Chen, A. Kingon, H. Al-Shareef, K. Bellur, K. Gifford, and O. Auciello, "Leakage and interface engineering in titanate thin films for non-volatile ferroelectric memory and ulsi drums," *Integrated Ferroelectrics*, vol. 7, no. 1, pp. 291–306, 1995.
- [56] B. Chae, C. Park, Y. Yang, and M. Jang, "Asymmetry in fatigue and recovery in ferroelectric Pb (Zr, Ti) O thin-film capacitors," *Applied Physics Letters*, vol. 75, p. 2135, 1999.
- [57] A. Kozyrev, O. Soldatenkov, T. Samoilova, A. Ivanov, C. Mueller, T. Rivkin, and G. Koepf, "Response time and power handling capability of tunable microwave devices using ferroelectric films," *Integrated Ferroelectrics*, vol. 22, no. 1, pp. 329–340, 1998.
- [58] R. York, "Circuit configuration for DC-biased capacitors," Jan. 5 2004, US Patent App. 10/752,370.
- [59] M. Schmidt, E. Lourandakis, R. Weigel, A. Leidl, and S. Seitz, "A Thin-Film BST Varactor Model for Linear and Nonlinear Circuit Simulations for Mobile Communication Systems," in *2006 IEEE Int. Symposium on the Applications of Ferroelectrics*, 30 Jul.–3 Aug. 2006, pp. 372–375.
- [60] K. Van Dyke, "A determination of some of the properties of the piezo-electric quartz resonator," *Proceedings of the Institute of Radio Engineers*, vol. 23, no. 4, pp. 386–392, 1925.
- [61] S. Butterworth and F. Smith, "The equivalent circuit of the magnetostriction oscillator," *Proceedings of the Physical Society*, vol. 43, no. 2, pp. 166–185, 1931.
- [62] J. Nath, D. Ghosh, J. Maria, M. Steer, A. Kingon, and G. Stauf, "Microwave properties of bst thin film interdigital capacitors on low cost alumina substrates," in *Proc. 34th European Microwave Conf.*, 11–15 Oct. 2004, pp. 1497–1500.
- [63] P. Scheele, "Steuerbare passive Mikrowellenkomponenten auf Basis hochpermittiver ferroelektrischer Schichten," Ph.D. Dissertation, Technische Universität Darmstadt, 2007.
- [64] A. Giere, Y. Zheng, H. Gieser, K. Marquardt, H. Wolf, P. Scheele, and R. Jakoby, "Coating of planar Barium-Strontium-Titanate thick-film varactors to increase tunability," in *Proc. 37th European Microwave Conf.*, 9–12 Oct. 2007, pp. 114–117.

- [65] P. Scheele, A. Giere, Y. Zheng, F. Goelden, and R. Jakoby, "Modeling and Applications of Ferroelectric-Thick Film Devices With Resistive Electrodes for Linearity Improvement and Tuning-Voltage Reduction," *IEEE Trans. Microwave Theory and Tech.*, vol. 55, no. 2 Part 2, pp. 383–390, 2007.
- [66] R. Jaeger, "Introduction to microelectronic fabrication," *Addison-Wesley Modular Series On Solid State Devices*, p. 232, 1987.
- [67] S. Lee, S. Park, and D. Cho, "The surface/bulk micromachining (SBM) process: a new method for fabricating released MEMS in single crystal silicon," *Journal of Microelectromechanical Systems*, vol. 8, no. 4, pp. 409–416, 1999.
- [68] C. Malek and V. Saile, "Applications of LIGA technology to precision manufacturing of high-aspect-ratio micro-components and-systems: a review," *Microelectronics Journal*, vol. 35, no. 2, pp. 131–143, 2004.
- [69] J. Gaspar, V. Chu, and J. Conde, "Electrostatic actuation of thin-film microelectromechanical structures," *Journal of Applied Physics*, vol. 93, p. 10018, 2003.
- [70] H. Lee, J. Park, J. Park, H. Nam, and J. Bu, "Design, fabrication and RF performances of two different types of piezoelectrically actuated Ohmic MEMS switches," *JOURNAL OF MICROMECHANICS AND MICROENGINEERING*, vol. 15, no. 11, p. 2098, 2005.
- [71] J. Park, Y. Yee, H. Nam, and J. Bu, "Micromachined RF MEMS tunable capacitors using piezoelectric actuators," in *2001 IEEE MTT-S Int. Microwave Symp. Dig.*, vol. 3, 2001, pp. 2111–2114.
- [72] V. Ziegler, "Low-complexity RF-MEMS switch technology for tunable microwave components," WMH-07 Workshop proceedings, 2008 MTT-S International Microwave Symposium, June 2008.
- [73] D. Sadler, S. Gupta, and C. Ahn, "Micromachined spiral inductors using UV-LIGA techniques," *IEEE Transactions on Magnetics*, vol. 37, no. 4 Part 1, pp. 2897–2899, 2001.
- [74] S. Chang and S. Sivoththaman, "A Tunable RF MEMS Inductor on Silicon Incorporating an Amorphous Silicon Bimorph in a Low-Temperature Process," *IEEE Electron Device Letters*, vol. 27, no. 11, pp. 905–907, 2006.
- [75] D. Goins, R. Nelson, and J. McKillop, "Design of a 20 GHz Low Loss Ohmic Contact RF MEMS Switch," in *2007 IEEE MTT-S Int. Microwave Symp. Dig.*, 2007, pp. 371–374.

- [76] R. Ramadoss, S. Lee, Y. Lee, V. Bright, and K. Gupta, "RF-MEMS Capacitive Switches Fabricated Using Printed Circuit Processing Techniques," *Journal of Microelectromechanical Systems*, vol. 15, no. 6, pp. 1595–1604, 2006.
- [77] D. Bell, T. Lu, N. Fleck, and S. Spearing, "MEMS actuators and sensors: observations on their performance and selection for purpose," *Journal of Micromechanics and Microengineering*, vol. 15, no. 7, pp. S153–S164, 2005.
- [78] J. Muldavin, C. Bozler, S. Rabe, and C. Keast, "Large tuning range analog and multi-bit MEMS varactors," in *2004 IEEE MTT-S Int. Microwave Symp. Dig.*, vol. 3, 6–11 Jun. 2004, pp. 1919–1922.
- [79] D. Peroulis, Y. Lu, and L. Katehi, "Highly reliable analog MEMS varactors," in *2004 IEEE MTT-S Int. Microwave Symp. Dig.*, vol. 2, 6–11 Jun. 2004, pp. 869–872.
- [80] M. Al Ahmad, R. Maenner, R. Matz, and P. Russer, "Integrated piezoelectric LTCC varactor," *Proceedings of the European Microwave Association*, vol. 1, no. 2, pp. 104–108, Jun. 2005.
- [81] M. Wren and T. Brazil, "Experimental class-F power amplifier design using computationally efficient and accurate large-signal pHEMT model," *IEEE Trans. Microwave Theory and Tech.*, vol. 53, no. 5, pp. 1723–1731, 2005.
- [82] J. Wood, D. Root, N. Tufflaro, W. Process, T. Centers, A. Inc, and S. Rosa, "A behavioral modeling approach to nonlinear model-order reduction for RF/microwave ICs and systems," *IEEE Trans. Microwave Theory and Tech.*, vol. 52, no. 9 Part 2, pp. 2274–2284, 2004.
- [83] H. De Los Santos, *Introduction to Microelectromechanical Microwave Systems*. Artech House, 2004.
- [84] *User-Defined Models, ADS Manual*, Agilent Technologies, Sept. 2006.
- [85] D. Girbau, N. Otegi, L. Pradell, and A. Lazaro, "Study of intermodulation in RF MEMS variable capacitors," *IEEE Trans. Microwave Theory and Tech.*, vol. 54, no. 3, pp. 1120–1130, 2006.
- [86] J. Fu, X. Zhu, J. Phillips, and A. Mortazawi, "Improving Linearity of Ferroelectric-Based Microwave Tunable Circuits," *IEEE Trans. Microwave Theory and Tech.*, vol. 55, no. 2 Part 2, pp. 354–360, 2007.



- [87] Y. Yoon, D. Kim, M. Allen, J. Kenney, and A. Hunt, "A reduced intermodulation distortion tunable ferroelectric capacitor-architecture and demonstration," *IEEE Trans. Microwave Theory and Tech.*, vol. 51, no. 12, pp. 2568–2576, 2003.
- [88] G. Matthaei, L. Young, and E. Jones, *Microwave Filters, Impedance - Matching Networks, and Coupling Structures*. McGraw-Hill, 1964.
- [89] P. Richards, "Resistor-termination-line circuits," *Proc. of the IRE*, vol. 36, pp. 217–220, February 1948.
- [90] I. Hunter and J. Rhodes, "Electronically Tunable Microwave Bandpass Filters," *IEEE Trans. Microwave Theory and Tech.*, vol. 82, no. 9, pp. 1354–1360, 1982.
- [91] E. Cristal, "Tapped-Line Coupled Transmission Lines with Applications to Interdigital and Compline Filters," *IEEE Trans. Microwave Theory and Tech.*, vol. 23, no. 12, pp. 1007–1012, 1975.
- [92] S. Caspi and J. Adelman, "Design of combline and interdigital filters with tapped-line input," *IEEE Trans. Microwave Theory and Tech.*, vol. 36, no. 4, pp. 759–763, 1988.
- [93] G. Torregrosa-Penalva, G. Lopez-Risueno, and J. Alonso, "A simple method to design wide-band electronically tunable comblinefilters," *IEEE Trans. Microwave Theory and Tech.*, vol. 50, no. 1, pp. 172–177, 2002.
- [94] J. Lim and D. Park, "A modified Chebyshev bandpass filter with attenuation poles in the stopband," *IEEE Trans. Microwave Theory and Tech.*, vol. 45, no. 6, pp. 898–904, 1997.
- [95] C. Tang, Y. Lin, and C. Chang, "Realization of transmission zeros in combline filters using an auxiliary inductively coupled ground plane," *IEEE Trans. Microwave Theory and Tech.*, vol. 51, no. 10, pp. 2112–2118, 2003.
- [96] E. Wilkinson, "An N-Way Hybrid Power Divider," *IEEE Trans. Microwave Theory and Tech.*, vol. 8, pp. 116–118, 1960.
- [97] D. Pozar, *Microwave Engineering*. John Wiley & Sons, Inc, 1998.
- [98] J. Reed, "The Multiple Branch Waveguide Coupler," *IEEE Trans. Microwave Theory and Tech.*, vol. 6, no. 4, pp. 398–403, 1958.
- [99] C. Ho, L. Fan, and K. Chang, "Broad-band uniplanar hybrid-ring and branch-line couplers," *IEEE Trans. Microwave Theory and Tech.*, vol. 41, no. 12, pp. 2116–2125, 1993.

- 
- [100] T. Hirota, A. Minakawa, and M. Muraguchi, "Reduced-Size Branch-Line and Rat-Race Hybrids for Uniplanar MMIC's," *IEEE Trans. Microwave Theory and Tech.*, vol. 38, pp. 270–275, 1990.
- [101] S. Parisi, "180 lumped element hybrid," in *1989 IEEE MTT-S Int. Microwave Symp. Dig.*, 1989, pp. 1243–1246.
- [102] E. A. Fardin, A. S. Holland, and K. Ghorbani, "Frequency Agile 90 deg Hybrid Coupler Using Barium Strontium Titanate Varactors," in *2007 IEEE MTT-S Int. Microwave Symp. Dig.*, 3–8 Jun. 2007, pp. 675–678.
- [103] W. Fathelbab, "The Synthesis of a Class of Branch-Line Directional Couplers," *IEEE Trans. Microwave Theory and Tech.*, vol. 56, no. 8, pp. 1985–1994, 2008.
- [104] F. Grover, *Inductance Calculations: Working Formulas and Tables*. Courier Dover Publications, 2004.
- [105] D. Staiculescu, A. Sutono, and J. Laskar, "Wideband Scalable Electrical Model for Microwave/Milimeter Wave Flip Chip Interconnects," *IEEE Transaction on Advanced Packaging*, vol. 24, pp. 255–259, 2001.
- [106] A. Ocera, P. Farinelli, F. Cherubini, P. Mezzanotte, R. Sorrentino, B. Margesin, and F. Giacomozzi, "A MEMS-Reconfigurable Power Divider on High Resistivity Silicon Substrate," in *2007 IEEE MTT-S Int. Microwave Symp. Dig.*, 2007, pp. 501–504.
- [107] E. Fardin, K. Ghorbani, and A. Holland, "A Varactor Tuned Branch-Line Hybrid Coupler," in *2005 Asia-Pacific Microwave Conference*, vol. 3, Dec. 2005, pp. 1408–1411.
- [108] F. Ferrero, C. Luxey, R. Staraj, G. Jacquemod, and V. Fusco, "Compact quasi-lumped hybrid coupler tunable over large frequency band," *Electronics Letters*, vol. 43, no. 19, pp. 1030–1031, 2007.
- [109] E. Djoumessi, E. Marsan, C. Caloz, M. Chaker, and K. Wu, "Varactor-Tuned Dual-Band Quadrature Hybrid Coupler," *IEEE Microwave and Wireless Components Letters*, vol. 16, no. 11, pp. 603–605, 2006.
- [110] W. Doherty, "A New High Efficiency Power Amplifier for Modulated Waves," *Proceedings of the IRE*, vol. 24, no. 9, pp. 1163–1182, 1936.
- [111] K. Eisele, R. Engelbrecht, and K. Kurokawa, "Balanced transistor amplifiers for precise wideband microwave applications," in *IEEE International Solid-State Circuits Conference*, vol. 8, 1965, pp. 18–19.

- [112] M. Nguyen, W. Yan, and E. Horne, "Broadband Tunable Filters Using High Q Passive Tunable ICs," in *2008 IEEE MTT-S Int. Microwave Symp. Dig.*, 15–20 Jun. 2008, pp. 951–954.
- [113] J. Dickson, "On-chip high-voltage generation in NMOS integrated circuits using an improved voltage multiplier technique," *IEEE Journal of Solid-State Circuits*, vol. 11, no. 3, pp. 374–378, 1976.

# Curriculum Vitae

## Personal Data

Name: Errikos Lourandakis  
Address: Holzgartenstrasse 29, 90461 Nuremberg, Germany  
Date of Birth: 29.09.1981  
Place of Birth: Nuremberg, Germany  
Family Status: not married  
Citizenship: Greece

## Education

09/87 – 07/93 Greek Elementary School, Nuremberg  
09/93 – 07/96 Greek Junior High School, Nuremberg  
09/96 – 07/99 Greek High School, Nuremberg

## Academic

09/99 – 02/05 Electrical and Computer Engineering, University of Patras,  
Patras, Greece (Degree: Dipl. Eng.)

## Professional

09/05 – 02/09 Research Assistant at the Institute for Electronics Engineer-  
ing, University of Erlangen-Nuremberg, Erlangen

Nuremberg, February 2009

Errikos Lourandakis

## D. Publications

- R. Weigel, and E. Lourandakis, 'Frequency Agile Ferroelectric Filters, Power Dividers, and Couplers,' to be published in Workshop Proceedings, 2009 IEEE MTT-S International Microwave Symposium (IMS), June 2009.
- E. Lourandakis, G. Fischer, and R. Weigel, 'Characterization and Modeling of Continuously Tunable MEMS Varactor,' to be published in 2009 German Microwave Conference, March 2009.
- E. Lourandakis, M. Schmidt, G. Fischer, and R. Weigel, 'A Ferroelectric Tunable Compline Filter With Improved Stopband Transitions,' in 2009 IEEE Radio and Wireless Symposium, January 2009, pp. 340–343.
- E. Lourandakis, M. Schmidt, S. Seitz, and R. Weigel, 'Reduced Size Frequency Agile Microwave Circuits Using Ferroelectric Thin-Film Varactors,' in IEEE Transactions on Microwave Theory and Techniques, Vol. 56, Issue 12, Part 2, December 2008, pp. 3093–3099.
- E. Lourandakis, M. Schmidt, S. Seitz, and R. Weigel, 'Tunable Lumped Element Filters With BST Thin-Film Varactors,' in 2008 European Wireless Technology Conference (EuWiT), October 2008, pp. 270–273.
- E. Lourandakis, M. Schmidt, and R. Weigel, 'Tunable BST-Varactor-Based Matching Networks for Mobile Radio Applications,' in Workshop Proceedings (WMH), 2008 IEEE MTT-S International Microwave Symposium (IMS), June 2008.
- E. Lourandakis, M. Schmidt, A. Leidl, S. Seitz, and R. Weigel, 'A Tunable and Reduced Size Power Divider Using Ferroelectric Thin-Film Varactors,' in 2008 IEEE MTT-S International Microwave Symposium (IMS), June 2008, pp. 967–970.
- E. Lourandakis, M. Schmidt, A. Leidl, S. Seitz, and R. Weigel, 'Reduced Size and Tunable Microwave Circuits Using BST Thin-Film Varactors,' in 2008 German Microwave Conference, March 2008, pp. 213–216, invited paper.

- 
- M. Schmidt, E. Lourandakis, A. Leidl, S. Seitz, and R. Weigel, 'A comparison of tunable ferroelectric  $\Pi$ - and T-matching networks,' in 2007 European Microwave Conference (EuMC), October 2007, pp. 98–101.
  - M. Schmidt, E. Lourandakis, R. Weigel, A. Leidl, and S. Seitz, 'A Thin-Film BST Varactor Model for Linear and Nonlinear Circuit Simulations for Mobile Communication Systems,' in 2006 IEEE International Symposium on the Applications of Ferroelectrics, July 2006, pp. 372–375.